Tampere University

SHAHROZ AHMED

HARDFACED WEAR RESISTANT COATINGS FOR MINING TOOLS

Materials Science and Engineering
Examiners: Prof. Petri Vuoristo, Dr. Jari Tuominen, MSc. (Eng.) Tuomo Saarinen
June 2019

ABSTRACT

Shahroz Ahmed: Hardfaced wear resistant coatings for mining tools
Master's Thesis, 108 pages
Tampere University
Master's Degree Program in Materials Science and Engineering
June 2019

Hardfacing is one of the methods to protect base material from severe wear and corrosion environment and provide life extension to the component. In this work, erosion resistance and impact resistance of four hardfacing alloys were tested in their as clad and post weld heat-treated conditions; two iron based alloys and two nickel based alloys were selected. The hardfacing was deposited by cold metal transfer (CMT) welding because the method provides the advantages of automated precise welding, low dilution, spatter free deposits and high degree of flexibility. Two cladding strategies were adopted while hardfacing; cladding on quench and tempered steel and cladding on soft annealed steel, which was later followed by heat treatment. The deposits were examined for their heat input, dilution, cooling time ($T_{8/5}$) and deposition rate. The erosion resistance of the alloys was tested with pulse jet equipment and impact resistance was analysed with hammer mill test; both tests were conducted at Tampere University. After hardfacing, the samples were grinded and cut according to the dimensions that would fit in both test equipment. Before the test the samples were analysed for their microstructure, phase and hardness to differentiate the results of as clad and heat-treated conditions. After the erosion and impact tests, the wear depth of the samples was analysed with Alicona optical surface profilometer. It was revealed that post weld heat-treated samples are not suitable for high wear resistance and there are high chances that heat treatment produces crack in the heat affected zone. The results of the erosion tests and impact tests yielded that iron based alloys, in their as clad state, offer high wear and impact resistance as compare to the nickel based alloys.

Keywords: Hardfacing, Cold Metal Transfer, Erosion, Hammer Mill, Pulse Jet

PREFACE

This thesis work was conducted at Tampere University Hervanta campus, in Materials Sciences and Environmental Engineering. The work started in October 2018 and finally was completed in June 2019.

I would like to thank my supervisor Senior Research Fellow Dr. Jari Tuominen for providing his support throughout this thesis work. He was a big help in preparing the cladding specimens and for his ideas in how to make this thesis better. He provided me with ideas and advices on how to improve this thesis. I would also like to thank my other supervisor Prof. Petri Vuoristo for his support during this work, he provided me with valuable knowledge about hardfacing and wear, and shared his ideas to perform the thesis with a better approach. I would also like to thank my third supervisor Tuomo Saarinen, who has been a big support in this work, sharing his knowledge about wear and heat treatment, also provided materials for experiments at the earliest.

I would like to thank Project Manager Jussi Laurila for carrying out SEM and EDS results for my specimens. I am also grateful to Project Researcher Leo Hyvärinen for conducting XRD analysis for my samples. A huge credit also goes to the staff of Laboratory of Materials Science, who were willing to help when I needed to work on new equipment.

Tampere, 26th June 2019
Shahroz Ahmed

CONTENTS

LIST OF SYMBOLS AND ABBREVIATIONS

Ar	Argon
CE	Carbon Equivalent
CMT	Cold Metal Transfer
CZHAZ	Coarse Grain Heat Affected Zone
E	welding energy
EDS	Energy Dispersive X-ray Spectroscopy
F_3	three-dimension welding coefficient
FZHAZ	Fine Grain Heat Affected Zone
GTAW	Gas Tungsten Arc Welding
HAZ	Heat Affected Zone
HDPL	High power diode lasers
He	Helium
HV	Hardness Vicker
I	mean current
ICHAZ	Intercritical Heat Affected Zone
IIE	International Institute of Welding
K	welding efficiency constant
MAG	Metal active gas
MIG	Metal inert gas
MMAW	Manual Metal Arc Welding
PAW	Plasma Arc Welding
PMZ	Partially Melted Zone
PTA	Plasma Transfer Arc
PWHT	Post Weld Heat-treated
Q	heat input
SEM	Scanning Electron Microscopy
SMAW	Shield Metal Arc Welding
$T_{(8/5)}$	cooling time from 800˚C to 500˚C
U	mean voltage
V	travel speed
WC	tungsten carbide
WFR	Wire feed rate
XRD	X-ray Diffraction

1. INTRODUCTION

Wear is often encountered in moving and sliding contacts or where lubrication is ineffective. Wear prevention is one of the biggest challenges in many applications and consequently damages from wear leads to substantial economic losses. So, counter measures are a necessity to avoid wear losses. As wear is not a material property but rather a system property. Any changes in the system can alter the wear rate. It is one of the reasons that wear characterization is complex, as wear rate varies in different environments. Recent researches have proved that surface coatings are efficient and cost-effective method to improve wear resistance. However, hardfacing by welding techniques offers a better resistance in severe wear environment as compared to thermal spraying and thermal hardening [1, 2].

Hardfacing offers properties such as, high resistance to abrasion, adhesion, impact, corrosion or a combination of these factors. Hardfacing provides a permanent metallurgical bond with the base material and proved to be cost effective in many applications as compared to thermal spraying and hardening. But, the major drawback of hardfacing is the high heat input to the substrate during welding [1, 2]. Variety of methods have been developed to produce a hardfaced coating that offers high deposition rates and low heat input. But, due to the high cooling rate it is necessary to characterize the weldment area and changes that have occurred in the base material after welding. As these changes can have a significant impact on the property of the whole component and can lead to undesirable results [2].

This thesis work focuses on examining the erosion resistance of four different hardfacing material deposited by Cold Metal Transfer (CMT). The deposits were characterized under impact loads to observe the mass loss of single weld overlay. The erosion resistance was planned to be characterized under wide particle size distribution and high velocity. So, pulse jet equipment was utilized for observing erosion resistance of hardfacing deposits. The erosion resistance of the deposits was observed under two different impingement angles and at high velocities. The hardfaced deposits were also compared for erosion resistance in as clad and post heat-treated conditions. It was one of the tasks in this thesis to compare erosion resistance of hardfacing alloys before and after heat treatment. The changes in the base material before and after heat treatment were characterized by optical microscopy, hardness measurements, X-ray Diffraction (XRD), Scanning Electron Microscopy (SEM) and Electron Dispersive X-ray Spectroscopy (EDS) analysis. All the samples were compared with their performance under impact loads and erosion resistance.

2. HARDFACING

Hardfacing is defined as the deposition of special alloys by various welding processes on exposed areas to prevent base materials from damage. Main applications of hardfacing lie in the areas where there is need to encounter severe wear, corrosion or to hinder sliding wear from unlubricated or insufficient lubricated metal-to-metal contacts [2]. Applications of hardfacing include mining tools, crushers, ball mills and earth moving equipment. Hardfacing is utilized in many areas and utilized in wide application, see Figure 2.1. Hardfacing is also utilized to recover parts that have deteriorated. Flawed components can be hardfaced to original dimensions, which results in increase in the life time of the component [3].

The information about the base material and the alloy to be hardfaced is essential but some other parameters need to be considered. The parameters include geometry of component, prevention of surface cracking, minimize stresses and distortion, deposition quality and cost [4]. Adequate selection of these process related parameters can lead to effective surface protection. Hardfacing is a versatile process and various alloys can be deposited to identical or non-identical base materials; selection of alloys depends on the nature of application [5].

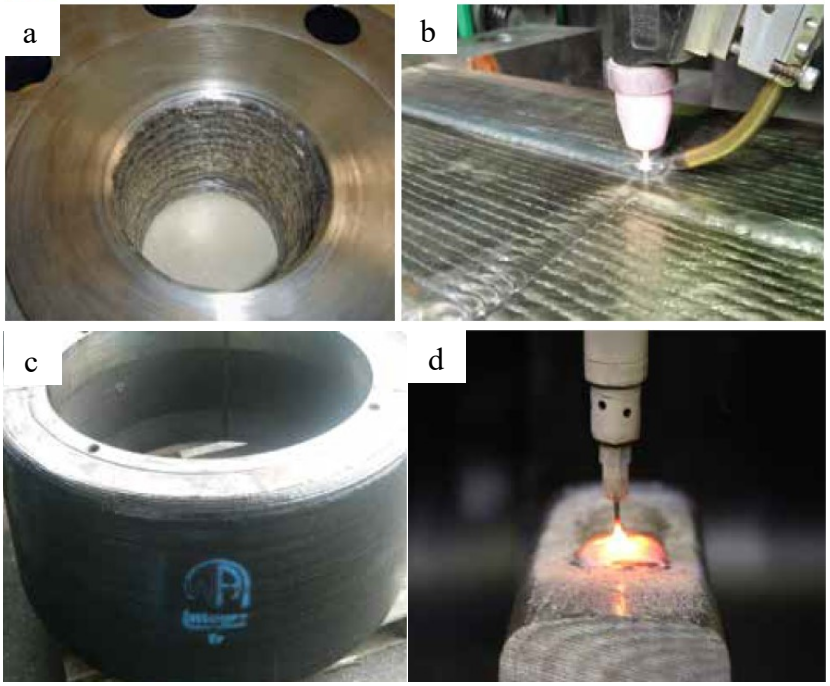

Figure 2.1: *Applications of hardfacing, (a) flange bore hold, (b) turbine housing, (c) Crusher roller, (d) Rail head* [6]

2.1 Hardfacing methods

There is a variety of methods that are used to produce a hardfaced coating. They vary in their form of filler material, heat source and operation mode, see Figure 2.2. Venkatesh et al. [7] list parameters that differentiate between the methods to be selected. The parameters include base metal composition, size and shape of the component, accessibility of the area to be welded, coating thickness, dilution, state of the filler material to be hardfaced whether in the form of wires, rods or powders and number of passes [7]. The common methods that are utilized for hardfacing are discussed in the following sections.

Method	Form of filler	Approx. min deposit thickness, mm	Dilution of deposit, %	Usual mode of application	Deposition rate*, kg/h
Oxy-acetylene, with welding rods	Bare wire, rod or tube	0.5	1 to 5	Manual	½ to 3
Oxy-acetylene with powders	Powder	0.08	1 to 5	Manual	½ to 7
Tungsten-inert gas (TIG)	Bare rod, wire or tube	1	5 to 10	Manual	½ to 2
Plasma transferred arc	Powder	0.25	5 to 30	Fully automatic	½ to 7
Shielded metal arc	Flux coated wire, rod or tube (manual), flux cored wire (semi-automatic)	2	10 to 30	Manual Semi-automatic	1 to 3 2 to 10
Open arc	Tubular wire, which may be flux-cored	2	15 to 25	Semi-automatic	2 to 10
Metal inert gas (MIG)	Bare wire or tube	2	10 to 25	Semi-automatic	2 to 10
Submerged arc	Bare wire, tube or strip	2	15 to 35	Fully automatic	2 to 70
Electroslag	Bare rod or tube	20		Fully automatic	50 to 350

Figure 2.2: *Methods for hardfacing* [8]

2.1.1 Oxyacetylene gas welding

The technique uses acetylene-oxygen flame to heat the substrate and melting the filler rod to produce a coating. Temperatures as high as 3000˚C are achieved when acetylene is combusted by oxygen. When the flame is sprayed on the surface, a small percentage of carbon is absorbed on the surface that creates a watery and glazed appearance that is called ‘sweating’. This layer has low melting point which produces very strong metallurgical bond with the surface and also contributes to reduce dilution. The hardfacing rod is melted drop by drop on the sweated area and spreads quickly [8, 9].

This technique has the advantage of operating at low cost and good quality of coatings require operator skills. The equipment is portable, easily available and requires no consumption of electricity. Dilution levels encountered with this method range from 5-6% and thermal shock of the weldment is also low because of slow cooling [9]. The method is suited for a vast number of materials but generally recommended for high carbon and chromium containing filler rods. This technique is not suited for hardfacing of larger components. Powders can also be used as a filler material instead of rods [10].

Albert et al. [10] have deposited wear resistant hardfacing of tungsten carbide (WC) in a matrix of nickel, copper and silicon alloy by oxyacetylene welding. The hardfacing consisted of uniform WC particles dispersed in the matrix with a volume fraction of 40%, uniform coat, low dilution with small percentages of porosity. Due to a lack temperature control in oxyacetylene welding, the fine powders of tungsten carbide melted in the matrix, which led to an increase in the wear resistance of the matrix but at the expense of reduced toughness. The deposited coating by oxyacetylene welding resulted in improved wear resistance and increased the lifetime of the component by eight times. However, it is advised that uniform size distribution of tungsten carbide particles would lead to better quality coating [10].

2.1.2 Shielded metal arc welding

Shielded metal arc welding (SMAW) uses arc between an anode and a cathode as the heating source to melt the base metal and deposit the alloy; it is also known as manual metal arc welding (MMAW). Electrodes are used as a filler material which is coated by various types of binders. Binders disintegrate during arcing and serve different purposes which includes arc stabilization, prevention from oxidation and contamination during welding and solidification, surface cleanliness by slag blanket and improves compatibility of weld metal by alloying elements, see Figure 2.3 [11]. Amado et al. [12] have proved in their article that efficient coating of tubular electrodes in SMAW increases the alloy transfer efficiency and results in low dilution for hardfacing applications.

The process works by connecting the electrode to the electrode holder, that is connected to the power source; the other end of the supply is connected to the work terminal. Arc ignites when the electrode is brought close to the workpiece, and then the electrode is pulled back to deposit the weld drop [11]. The main process parameters are the control of current and voltage, which depend on the selected filler material and the base metal. The orientation of the electrode is also an important parameter that needs to be taken into account [12].

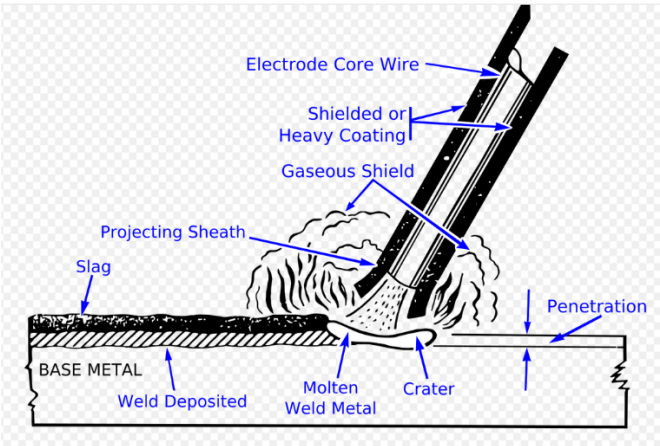

Figure 2.3: *Schematic diagram of shielded metal arc welding* [11]

There have been various studies in SMAW welding regarding different process parameters, but one of the key properties is to study the transfer of molten metal on the substrate. The mode of metal transfer determines the stability of the process, geometry of weld bead and spatter control [12]. The weld drop detachment occurs by short-circuiting, which is a very short period (around 4-5ms) of time, it arises when the weld drop touches the weld pool and created zero resistance and increased current. Due to increased current, heating of the contact between the weld drop and the molten pool results in decreased surface tension, lower viscosity of the weld drop, increment in electromagnetic forces, which results in weld drop transfer. Short circuit time depends on the surface tension of the weld drop detached from the electrode. Longer short-circuiting times is not recommended because it leads to process instability [13].

Amado et al. [12] have studied wear resistant hardfacing by SMAW to examine the effects of different electrodes with varying current values. The article revealed that tubular electrodes were most suited for hardfacing application because they offer a higher deposition rate as compared to solid electrodes under the same current values. Higher current values can lead to a higher deposition rate with solid electrode, but it affects the coated binders, which can disintegrate at high currents before performing their intended functions. Solid electrodes also resulted in higher short-circuiting times and lower short-circuiting frequencies, which leads to larger drop diameter. The study by Amado et al. [12] also proves that even at high current vales the weld drop transfer occurs by short-circuiting and for hardfacing applications the ideal limit for short circuit is less than 3ms, which is proven by the study conducted by Cruz et al. [13].

2.1.3 Metal inert gas welding

Metal inert gas welding (MIG) also uses electric arc as the source of heat. The main difference between MIG and SMAW is the supply of shielding gas and use of wire electrode. SMAW uses coated flux and electrode as rods whereas MIG uses filler metal in the form of wires and shielding gas, which is supplied externally, to protect weld pool from oxidation or other atmospheric attack. MIG is a subtype of gas metal arc welding (GMAW) with other subtype being metal active gas welding (MAG). The difference between MIG and MAG lies in the use of shielding gas; the former uses inert gases while the latter uses active gaseous mixture. The advantage of MIG welding is that the process is automated or semi-automated, which increases the deposition rate. Three types of wires are utilized in MIG, flux cored, solid and tubular, the diameter of wires ranges from 0.8-2mm [14].

The setup of MIG welding consist of power source, welding torch, wire feeder, shielding gas supply and in some cases an external cooling for the welding torch, see Figure 2.4. The welding torch also contains the nozzle for shielding gases; the inert gaseous mixture can be changed according to requirements. DC current is recommended with positive electrode potential; DC reverse polarity sometimes results in an unstable erratic arc,

which can disturb the shielding gas environment and cause contamination in the weld pool. Alternating current is not preferred as it periodically causes arc extinction [14].

As the process is automated or semi-automated, the wire feeder supplies the wire continuously. The wire feeder uncoils the wire at a rate selected by the operator, the rate depends on the filler wire burn rate under constant arc length. Although it is necessary to maintain a constant arc length, it can be changed by altering the voltage; even small changes in voltage can cause the arc length to alter. MIG welding, like other arc welding processes, uses high current low voltage for igniting the arc. The range of current and voltage depends on the weld metal, shielding gas and mode of metal transfer [14, 15].

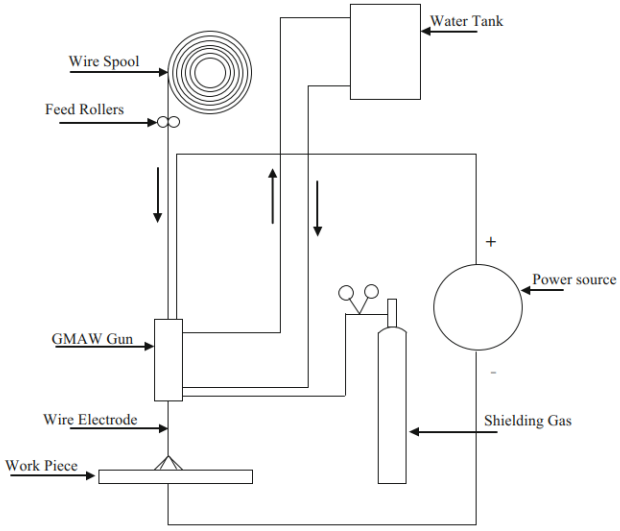

***Figure 2.4**: Schematic diagram of the components of MIG welding* [14]

Cruz et al. [13] described that the metal transfer in SMAW only takes place by short-circuiting, while as per Ersoy et al. [16] metal transfer in MIG occurs by three different modes, globular, spray transfer and short circuit. Fouilland et al. [15] have defined a fourth mode of metal transfer which is named as 'pulse transfer'. Each method differs in arc voltage and current, shielding gas, extension of electrode, composition and diameter of the filler wire.

Short circuit mode, described in sec. 2.1.2, is recommended for the repairing of joints, welding of thin sheets, heat sensitive materials and where there is need for single pass welding. This mode results in lack of penetration of filler metal, large spatter and high cooling rate of the weld pool [14].

In globular mode, the weld drop transfer under the influence of gravitational forces. The size of the deposited weld drop is significantly larger than the diameter of the wire. It occurs at a low current level and high percentage of carbon dioxide is used as a shielding gas, along with some percentage of argon. Only horizontal and flat direction welding can

be carried out with this method because increased size of weld drop makes deposition difficult in vertical direction. Excessive spatter is encountered with this method however, it can be reduced by using only CO_2 as a shielding gas. Generally, 100% CO_2 is not recommended as it can significantly reduce the corrosion resistance, especially in case of stainless steels [14, 16].

A steady surge in arc current gradually increases the rate of electrode melting and escalates the frequency of the weld drop transfer. At a high current value, the gravitational forces acting on the weld drop becomes insignificant as compared to the electromagnetic forces and a stream of molten metal is detached from the electrode. The stream of small size molten droplets only forms at a certain level of high current known as 'transition current'. This mode of transfer is termed as spray transfer and is characterized by small molten droplets, high arc voltage and current. It is suitable for welding of thick sections in flat and horizontal positions and created less spatter as compared with other modes. The drawback of this mode is the use of high current, which results in elevated heat input [14, 16].

Pulse transfer is a recent development mode of metal transfer in MIG. This mode offers a low heat input and an advantage to weld in multiple directions with minimum spatter. The process works by creating a pulse between high and low levels of current. The mean value of current generally falls in the range of currents encountered with globular and spray transfer, the high value associates with spray transfer while low current is a characteristic of globular transfer. It is suited for a variety of materials and deposition quality of the weld is relatively high [14]. Pulsed MIG reduces the level of heat input, several millimeters thick hardfacing can be deposited and required machining is less. Fouilland et al. [15] reported these results while depositing stellite coating on top of hot working steel.

2.1.4 PTA Hardfacing

Plasma Transfer Arc (PTA) is a welding process that utilizes transferred plasma arc as a heat source for welding, Figure 2.5 shows a schematic diagram of PTA welding. A tungsten non-consumable electrode is used to generate plasma arc between the torch and base material by ionizing the gas supplied by nozzle, which is surrounded by orifice; the ionization gas mostly consists of Ar or a mixture of Ar and He. Filler metal in form of powders are used in PTA; filler metal in the form of wires can also be used, the process is called Plasma Arc Welding (PAW). A carrier gas is used to transfer the molten material to the workpiece and a shielding gas is used to protect the weld; inert gas such as Ar is used to fulfil these purposes [8, 17, 18]. PTA is also utilized in hardfacing applications for the advantages of low dilution and high deposition rates; dilution rates of 4-7% and deposition rate of 5kg/hr are achieved from hardfacing by PTA welding, according to reference [8].

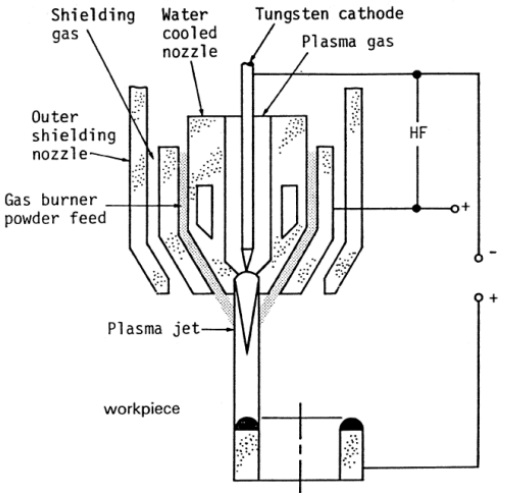

Figure 2.5: *Schematic diagram of Plasma Transfer Arc welding* [8]

Ulutan et al. [19] deposited hardfacing of FeCrC composite at different currents to analyze for wear losses, they reported that the hardfacing was free of cracks, porosity and bonding defects. The results also included that minimum wear losses were encountered with the hardfacing that was deposited at a current of 100A.

2.1.5 Cold metal transfer

Cold metal transfer (CMT) welding is a modified form of Metal Inert Gas welding process, which was developed by Fronius GmbH in 2004. Invention of CMT was accompanied by multiple advantages which includes low heat input, possibility to weld dissimilar metals with high accuracy and complete automation. The process differs from conventional MIG/MAG process by the mode of material transfer, which has not been previously encountered [20]. CMT deposits materials by dip metal transfer mode that is based upon mechanically assisted droplet deposition. The weld droplet detachment by CMT is the deciding factor that supersedes this technology as compared to ordinary MIG welding [21]. Experiments have proved that CMT has a higher melting potential for the same electrode as compared to MIG/MAG welding, so power utilization is much improved [22].

The basic components of the welding equipment are similar as in MIG, which consist of power source, filler metal wire, shielding gases and a welding torch. The difference lies in the innovation of welding torch and the introduction of a wire buffer. There are two separate wire drives integrated, the front drive moves the wire in forward and backward positions while the rear drive creates tension in the wire and pushes it forward. The front drive is connected with an alternating current servomotor, which oscillates the wire at frequencies up to 70 Hz and assist in the weld drop detachment. A ‘wire buffer’ is incorporated between the two drives, it assists in creating additional space for wires and also separates the two wire drives [23].

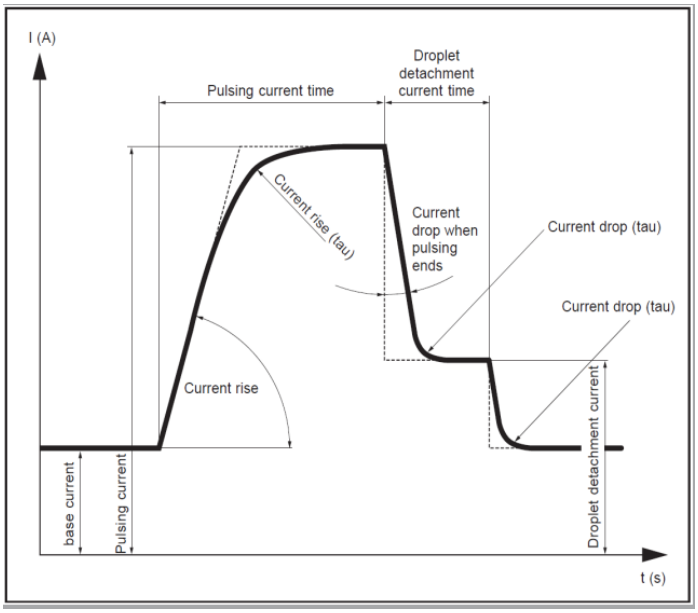

Figure 2.6: *Pulsating current phenomenon while drop detachment* [23]

Fronius GmbH represents the behavior of the pulsating current and weld drop detachment, shown in Figure 2.6. To understand the procedure of the weld drop detachment in CMT thoroughly, Selvi et al. [20] and Kah et al. [21] have broken down the weld cycle into steps. The success of these steps lies in the absolute control of arc current and voltage, see Figure 2.7, which is why they are controlled by an algorithm installed in the CMT program, the three steps are:

- **Peak current phase**: The peak current phase signifies the initiation of arc with a high pulse of current and a constant voltage. The arc ignites and heats the work piece and the electrode.
- **Background current phase**: The current is dropped in this phase, reduction of current ensures that weld drop does not retract from the electrode but remains attached in the form of a globule. The current drop in this stage is responsible for the low heat input and also prevents damage to the work piece from excessive heating.
- **Short circuit phase**: once the current is lowered, the electrode is pushed to the weld pool which initiates a short circuit. As soon as the short circuit is sensed the voltage is brought down to zero and current is brought to minimum, which diminishes the arc. By the help of alternating current servomotor, the wire oscillates producing a back draw force in the wire that results in liquid fracture and weld drop transfer to the pool. Then the gun moves forward and the cycle starts again.

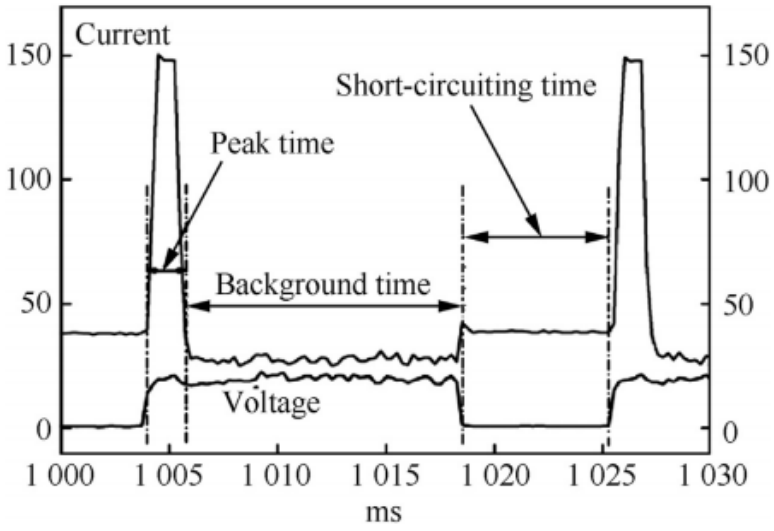

Figure 2.7: *Waveforms for current and voltage in a CMT cycle* [20]

Amin [24], conducted heat source models for CMT and presented a graphical model of the weld drop detachment in sequence, see Figure 2.8. Pickin at al. [25] carried out comparisons between the utilization of current as a function of the wire feed rate in CMT and MIG welding, their trials have concluded that welding performed by CMT has certain advantages over MIG/MAG welding, that are:

- **Reduced Heat Input**: By comparing the utilization of current between pulsed MIG and CMT, experiments revealed that, for the same amount of current the material deposition is higher in CMT. The relationship between **WFR** (wire feed rate) and **Im** (mean current) is linear in CMT which was analyzed by weld bead penetration. The reduced current increases the efficiency of the process and prevents burnout of the workpiece.
- **Control of Material Penetration**: Dilution of the wire can be controlled by altering the duration of the short circuit phase, which is irrespective of the wire feed rate and current relationship. Adjusting this short circuit period not only influences the shut off time of the arc but also effects the frequency of the arcing phase and also inhibits further heat transfer to the workpiece.

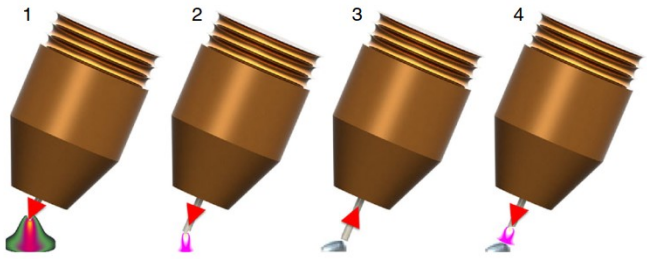

Figure 2.8: *Stages of weld drop detachment, (1) arc melts the base metal and wire (2) creation of weld drop resulting in short circuit (3) arc extinguishes and wire retracts back after detecting short circuit (4) wire moves forward and arc reignites* [24]

Ola et al. [26] deposited Inconel 718 superalloy filler clads on 718 substrate by CMT, the article revealed that clads of Inconel 718 superalloy were effectively deposited by CMT and results in low dilution. They further recommended cladding of Inconel 718 by CMT for repairing damaged or worn-out parts. The research also added that microstructure of the clads were free from cracks and porosity with a strong metallurgical bond. Cao et al. [27] have revealed that it is a challenge welding aluminum to galvanized mild steel, but this welding was successfully done through CMT. The article added that CMT is one of the versatile methods when welding dissimilar metals provided that parameters are chosen according to the selected materials.

2.1.6 Laser cladding

Laser is the abbreviation of 'Light Amplification by Stimulated Emission of Radiation'. Laser is an intense form of light, which is released by an atom in the excited state. Energy can be provided in the form of electricity to excite the atom and release a photon; this photon is the source of generating laser. Usually it is believed that power is the deciding factor between a white light and a laser, however it is not the case as some lasers have lower intensities than the light from a torch. There are three distinguishing factors between a flashlight and a laser. First, the flashlight is much broad than a laser, secondly, white light consists of many colors while laser consist of a single wavelength photons. Third, photons in a laser are aligned in a single direction, while light waves are aligned randomly in a flashlight [28].

The unique characteristic of laser is the capability to produce a very narrow and uniformly aligned beam. Because of this property, lasers find a wide variety of applications ranging from bar codes to laser printing. In materials processing, lasers have been efficiently utilized for cutting, drilling, welding and in heat treatment applications. Precise cuts and holes are made in an efficient and cost-effective manner. The cuts made by lasers are much precise than mechanical cutters [28].

Different kinds of surface treatments are carried out by laser technology that includes surface hardening, surface melting and cladding. Surface hardening involves producing wear resistant layers on surface of components; melting of surface does not take place. The source provides an excellent heat sink for cooling and automatic quenching takes place producing a hardened surface layer. Lasers for surface melting are intended for making controlled alloy additions to make it wear or corrosion resistant. Lasers produce fine microstructures as compared to ordinary means of alloying; however, this application has yet to find wide industrial application [29].

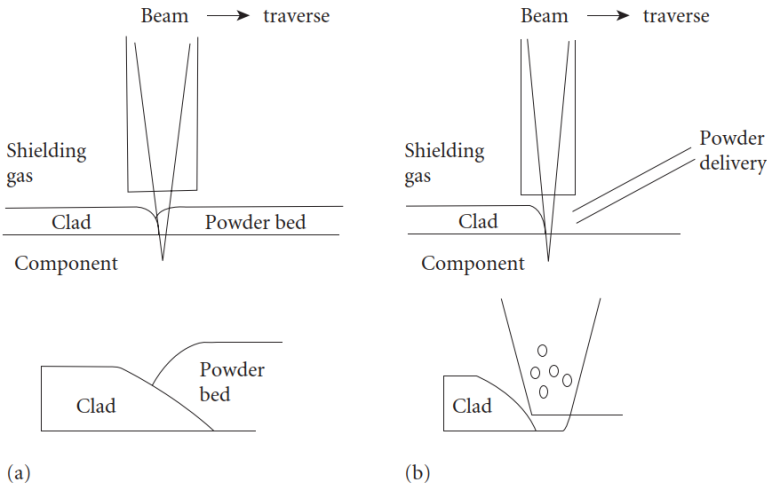

Figure 2.9: *Methods of cladding, (a) predeposition (b) codeposition* [29].

Laser cladding is a fusion process in which melting of an alloy and the substrate takes place to produce a clad. High power diode lasers (HPDL) are best suited for producing clads because of their high efficiency and they are maintenance free. The alloy can be predeposited or codeposited in the form of foils, powders or wires but powders are recommended, see Figure 2.9. If the alloy is predeposited, the lasers directly interact with the alloy and melts it, the melt front moves until it reaches the substrate resulting in melting of substrate and dilution of the alloy. If the alloy is codeposited, some fraction of laser melts the alloy and other fraction melts the substrate. The substrate acts a heat sink and fast cooling takes place. The dilution encountered with laser cladding is generally low, typically around 5% [29, 30].

Dilution is one of the deciding parameters that differentiates between clad qualities. Dilution needs to be kept at a low level because it affects the hardness of the clad [31]. Ming et al. [30] carried out laser cladding of nickel base alloys with the addition of WC powders to study the dilution effects. It is concluded that, a higher powder feed rate resulted in a decrease of dilution and tensile strength; the optimum parameters however produced a dilution level of 4-8%. Hemmati et al. [31] carried out a similar study to investigate the dilution levels by laser cladding nickel base alloy. It was revealed that iron content in the alloy greatly influences the dilution levels and the precipitation phases. Additionally, it was stated that an effective control over the parameters can result in very low dilution levels by laser cladding. Amado et al. [32] recommends in their article, that powder fillers are most appropriate for wear resistant hardfaced coatings. Moderate intensity and large scanning speeds of lasers are best suited for hardfacing applications as these parameters lead to homogenous distribution of WC particles.

2.2 Hardfacing materials

There are variety of alloys that are used as consumables in hardfacing applications but generally, they are categorized in four sections, given in Table 2.1. The selection of appropriate hardfacing material is important as the economic success depends on it [33].

Table 2.1: *Classification of hardfacing alloys* [33]

Group	Hardfacing alloys	Total alloy content, %	Principal alloying elements
1a	Low alloy Iron based Alloys	6-12	Cr, Mo, Mn
1b	High alloy Iron based alloys	12-50	Cr, Mo, Mn, Ni, Co
2	Nickel based alloys	40-70	Cr, B, Si, C, Fe
3	Cobalt based alloys	40-70	Cr, C, W, Mo

2.2.1 Iron based alloys

Iron based alloys are the most cost-effective hardfacing alloys available. The cost increases as the percentage of alloying elements increases. They are also widely utilized in hardfacing application because of their wide availability and compatibility to weld with dissimilar metals. Wear resistance of iron based consumables depend on the alloy content. The main alloying elements are carbon, chromium, vanadium, molybdenum, niobium and tungsten. These elements form hard phases by precipitation hardening which increases the wear resistance of the alloys [6, 34].

Nature of the precipitated carbides depends on the solidification mode i.e. hypoeutectic, eutectic or hypereutectic. The primary precipitated carbides are of the stoichiometric composition M_7C_3 and $M_{23}C_6$, where M indicates the highest amount of carbide forming element. M_7C_3 carbides are generally favored in hardfacing application due to their higher resistance to wear than $M_{23}C_6$ carbides. Hypoeutectic and eutectic composition alloys favors the precipitation of $M_{23}C_6$ in an austenite matrix. Hypoeutectic $M_{23}C_6$ tend to be fine lamellar structure, while the morphology of eutectic $M_{23}C_6$ tend to be equiaxed dendrite. Hypereutectic alloys favors the precipitation of M_7C_3 carbides in an austenite matrix, the reason being the content of carbon and principal alloying element. Although both types of carbides can be found in hypo and hypereutectic alloys [35-37].

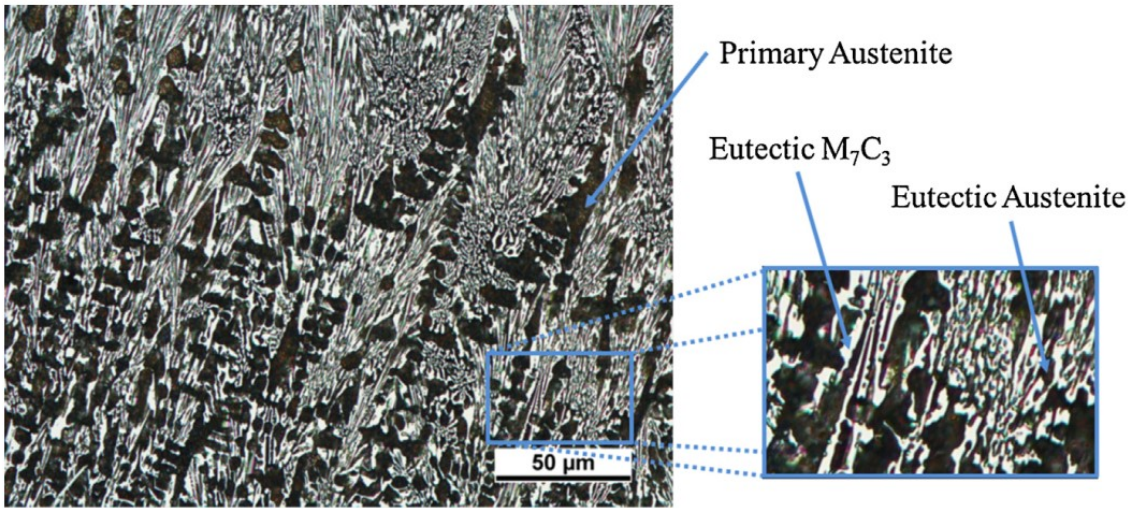

Figure 2.10: *Structure of a hypoeutectic Fe-Cr-C alloy* [36]

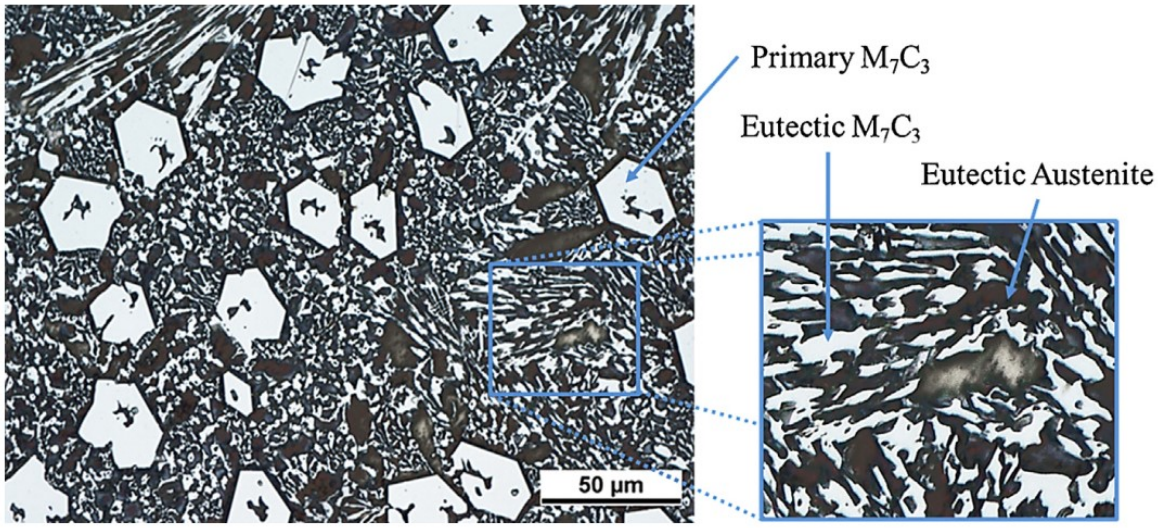

Figure 2.11: *Structure of a hypereutectic Fe-Cr-C alloy* [36]

Sabet et al. [38] compared the wear resistance of Fe-Cr-C hardfacing alloys with hypo and hyper eutectic compositions. It was revealed that hypereutectic alloys produced a higher resistance to wear; the reason being the content of carbon and chromium. According to Sabet et al. [38], in hypoeutectic alloys proeutectic austenite nucleates before M_7C_3 and the microstructure consist of eutectic M_7C_3 in a primary austenite matrix. While in hypereutectic composition alloys, the structure consists of primary carbides followed by the growth of eutectic austenite. Figure 2.10 and 2.11 presents the structure of hypo and hypereutectic Fe-Cr-C alloys, with M_7C_3 being as chromium carbides.

2.2.2 Nickel based alloys

Nickel based hardfacing are mostly utilized in the areas where there is need to prevent a combination of wear and corrosion or to encounter thermal degradation. Application of hardfacing of these alloys include valve seats, nuclear reactors, spiral conveyor screws. These alloys generally have a hardness above 55HRC, and they are known for maintaining their hardness at temperatures around 850°C. Properties of these alloys depend on the content of alloying elements; principal alloying elements of nickel-based consumables are given in table 2.1. These elements solidify and combine to form various phases that contribute to the properties of the alloy. Typical phases consist of γ-Ni, Ni_3B, Ni_3Si, Cr_5B_3, Cr_7C_3 and Fe_7C_3 [6, 36, 39].

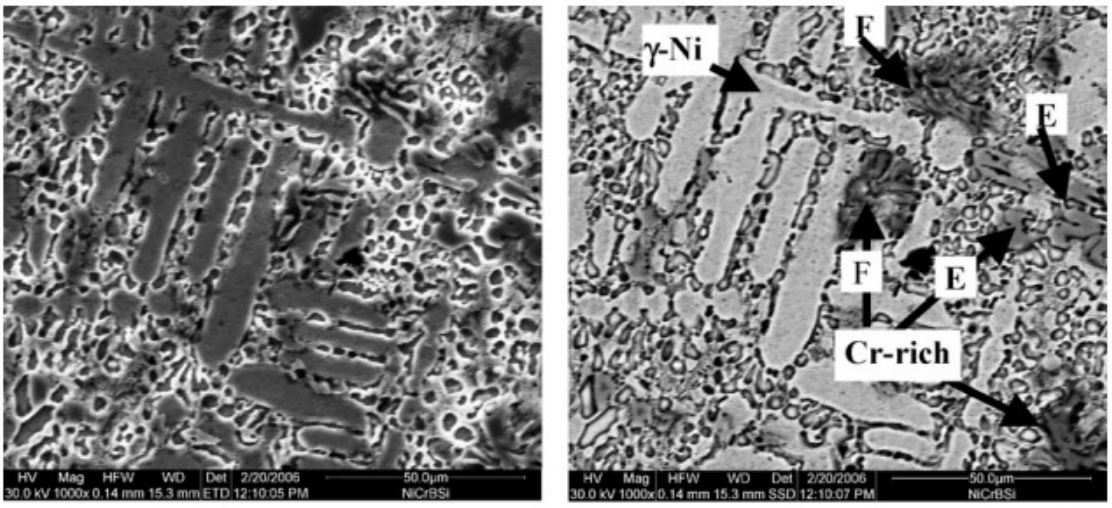

Figure 2.12: *Bright and dark field images of Ni based hardfacing, E represents eutectic phases* [40].

Solidification rate and alloy content controls the microstructure of nickel based hardfacing which mainly consist of primary dendritic γ-Ni with eutectics of carbides and interdendritic γ-Ni [41] , Figure 2.12. Hemmati et al.[42] carried out their research to inquire effect of alloy content on the properties of Ni-B-Cr-Si alloys. It was observed that high content of chromium tends to cause cracks, it was concluded that content of chromium could be suppressed and addition of small amount of niobium can prevent crack growth. However, control of welding parameters such as feed rate, cladding speed and heat input also have dominant effect on the microstructure. These parameters can be effectively controlled by choosing a suitable hardfacing technique; researches suggests that laser cladding of nickel-based alloys have produced a superior microstructure as compared to other methods [39, 41, 42]. Thick coatings of nickel-based alloys with strong metallurgical bond have been able successfully deposited by laser technology [42].

Nickel based alloys can provide good resistance to wear in low to mild abrasive environment, but it will degrade in severe wear environments. It is a common practice to add

tungsten carbide (WC) powders with nickel alloys to improve abrasion resistance. Addition of WC increases the overall hardness of the alloy and wear resistance depends on the volume fraction of these particles. Nickel based alloys provide a tough matrix and suitable interphase for WC powders that increase the performance of the hardfacing in severe wear environments. The overall structure consist of a matrix of γ-Ni, eutectic carbides and WC/W_2C particles, Figure 2.13 [6, 36].

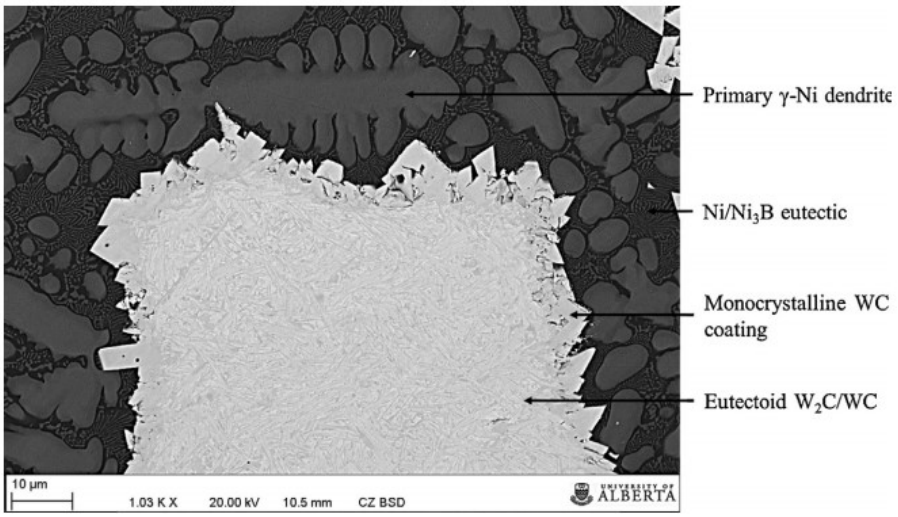

Figure 2.13: *Microstructure of Ni-B-Si with WC powders* [36]

WC is introduced into the melt in the form of powders, these powders should not undergo melting otherwise the wear resistance is suppressed to a high degree. To avoid melting of WC powders, a low heat input should be selected [36, 43]. Katsich et al.[43] studied wear properties of WC/Ni based alloy deposited with different values of current; 50, 80 and 110A were selected as current values. Their research Figured out that as the heat input levels were increased, the carbides began to degrade and reduced the wear resistance of the alloy. The alloy deposited with 50A incurred minimum mass loss in wear tests as compared to alloys deposited with higher values of current.

2.2.3 Cobalt based alloys

Cladding of cobalt based alloys find applications in the areas where there is need to counter severe wear environment at high temperature. These alloys have good resistance to abrasion, erosion, corrosion and oxidation. Cobalt based hardfacing have very low coefficient of friction, because of this property they are utilized in low lubricated areas, or where there is risk of metal to metal sliding wear. For hardfacing applications, cobalt - chromium alloys are used; commercial name for these alloys is stellite, and main alloying element is chromium with some amounts of carbon, molybdenum and tungsten. There are various grades of stellite for different applications, each grade differentiated from another by the alloy content. The wear resistance depends on the carbide content; content of carbon in the alloy dictates the fraction of carbides [44, 45].

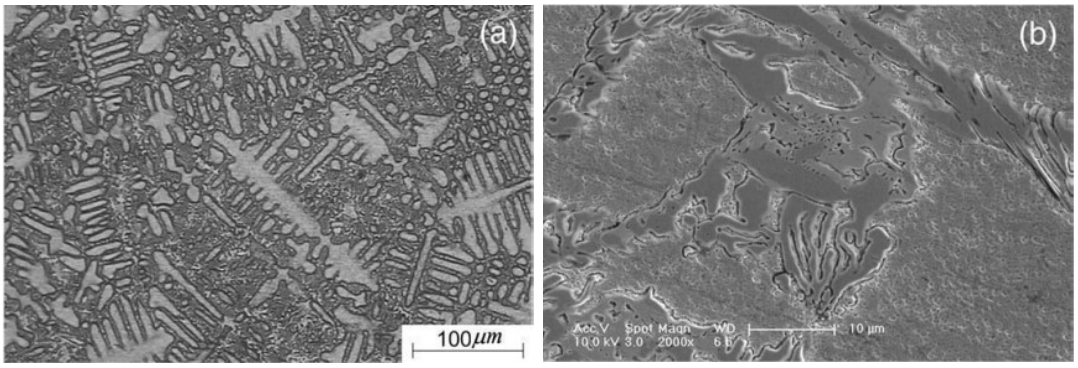

Figure 2.14: *Dendritic and interdendritic regions of the microstructures of Stellite, (a) low magnification, (b) high magnification* [46]

The microstructure consists of dendritic cobalt-chromium matrix with and interdendritic carbides of the order of M_7C_3 and $M_{23}C_6$, see Figure 2.14. Molybdenum and tungsten increase the strength and wear resistance by forming intermetallic phases of $Co_3(Mo,W)$ and carbides of the order of MC and M_6C [46]. Due to these high amount of carbides, stellite alloys are susceptible to cracking but these cracks can be avoided by selecting adequate process and parameters. Hardfacing of stellite can be deposited by SMAW, Gas Tungsten Arc Welding (GTAW), Plasma Transfer Arc (PTA) or laser cladding [44].

Cobalt based alloys have superior properties as compared to nickel-based alloys, one of the reasons is the crystal structure of cobalt matrix. Cobalt has a face centered cubic (FCC) crystal structure at temperature above 417°C, and when cooled slowly thee fcc transforms to hcp. As the cooling rates in welding are considerably high, cobalt retains the fcc structure which is unstable and has a very low stacking fault energy. This fcc structure can transform to hcp by mechanical stresses or by providing enough temperature. The fcc crystal due to its low stacking fault energy provides the alloy with high yield strength, low fatigue damage and high work hardening; the alloy is able to withstand higher stress due to transformation from fcc to hcp. These attributes give the alloy higher resistance to material damage in wear conditions with a combination of resistance to cavitation and corrosion [47].

3. WELDING OF QUENCH AND TEMPERED STEELS

Quenched and Tempered steels refer to class of steels that have been subjected to quenching and tempering treatment for improvement of mechanical properties. Typical microstructures of quench and tempered steels consist of tempered martensite, bainite, small amount of pearlite and very minute amount of retained austenite can also be present if the steels contain 2% silicon. Steels containing less than 0.25% carbon are not usually quench and tempered; 0.25-0.55% carbon steels are mostly subjected to quenching and tempering. Oil quenching is preferred to minimize stresses and tempering in the range of 350°-700°C can induce tensile strengths of 900-1600MPa; applications of these steels include shafts, tools and machined parts [48]. Major alloying elements in these steels include silicon, manganese, chromium and vanadium; the role of alloying elements include inhibition of coarsening of cementite, higher cooling rate to avoid nose region in CCT diagram and secondary hardening [18, 48].

Welding of quenched and tempered steels is one of the suitable methods to produce to strong joint that is metallurgically bonded. Welding involves fusion of filler metal and a base material that produces a coalescence of molten metal followed by high cooling rate. Fusion welding can be classified according to their heat source; heat sources for welding vary from oxyacetylene, lasers, electron beam and electric arc. Heat input in welding also affects the base metal, which can include localized melting, residual stresses and structural changes. Due to the high heat input, distinct zones are created in the base metal, [48, 49], which are discussed in the following sections.

3.1 Fusion zone

Fusion zone represents the area in which the materials have undergone melting, and the chemical composition of the fusion zone depends on the materials involved in melting, Figure 3.1. The fusion zone may not have the equal balance of base metal and filler metal and the composition can depend on many factors including welding process, melting point of the materials and cooling rate [50]. The amount base metal in the fusion zone is termed as dilution and as discussed in section 2.1, low dilution can result in higher hardness in the fusion zone.

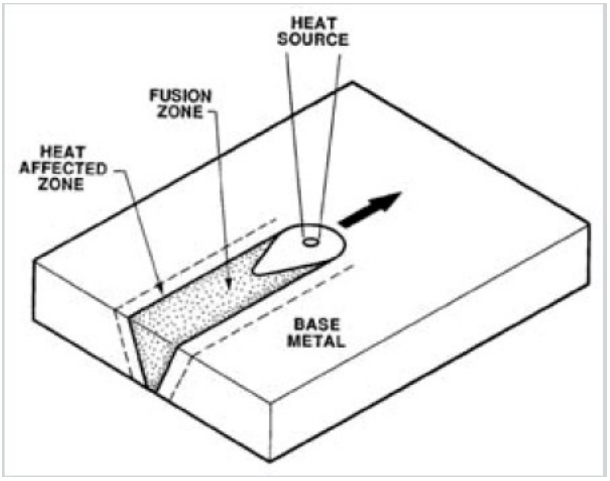

Figure 3.1: *Schematic diagram of the welding process showing; fusion zone, heat affected zone and the base metal* [51]

The strength of the fusion zone depends on the microstructure; and microstructure is dependent on the solidification mode. During the solidification of an alloy three modes of solidification can exist which includes planar, cellular and dendritic, see Figure 3.2. However, as the cooling rate is very high in welding dendritic mode of solidification is favorable in welding solidification according to the constitutional supercooling theory. The morphology of the grains during solidification and the size of the these grains depends on the temperature gradient (G) and the growth rate (R), higher cooling rate results in finer structures of the dendrites in the fusion zone [49], see Figure 3.3.

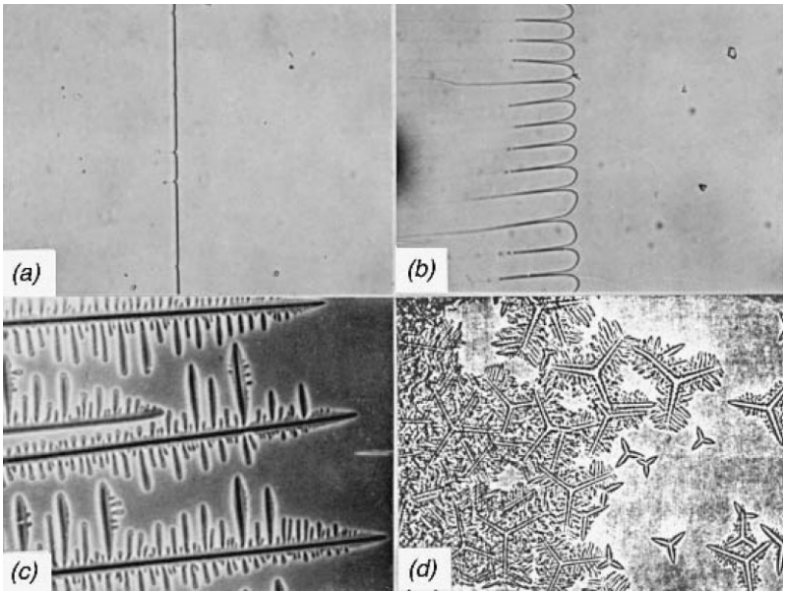

Figure 3.2: *Basic modes of solidification: (a) planar (b) cellular (c) columnar dendritic (d) equiaxed dendritic* [49]

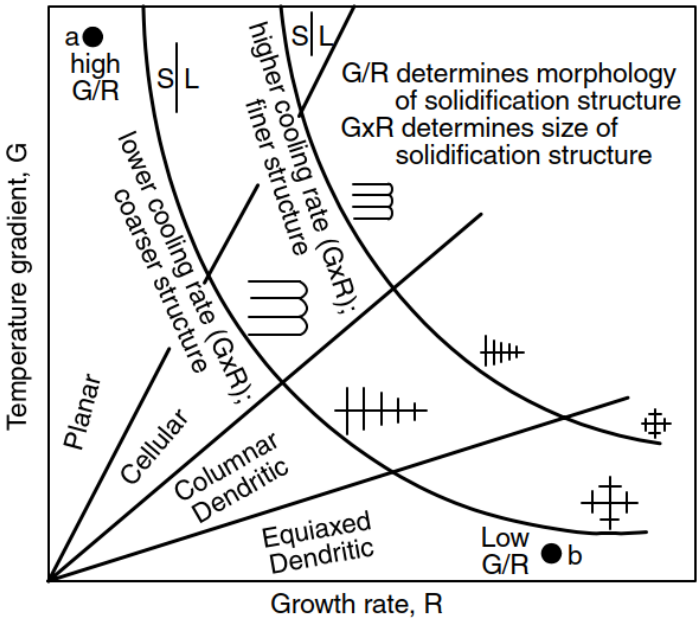

Figure 3.3: *Effect of temperature gradient and growth rate on the morphology and size of grains in weld solidification* [49]

The mechanical properties are greatly affected by the grain structure, size and the orientation of the grains. The grains in the fusion zone grow by epitaxial growth or non-epitaxial growth that depends on the welding method; while grains away from the fusion zone, grow by competitive growth, see Figure 3.4. In both the growth mechanisms, the grains orient in the direction where the heat dissipation is maximum. The direction of maximum heat dissipation or easy growth directions depend on the crystal structure of the materials; for bcc and fcc materials, 100 is the easy growth direction for dendrites. Due to this directional growth, the properties of the weld become anisotropic and mechanical properties perpendicular to the direction to the weld are significantly suppressed. To encounter these problems, some measures such as inoculation and external excitation are adopted. Both measures result in grain refining as increasing the amount of grains; as increasing the amount of grains results in the increase of tensile strength [49, 51].

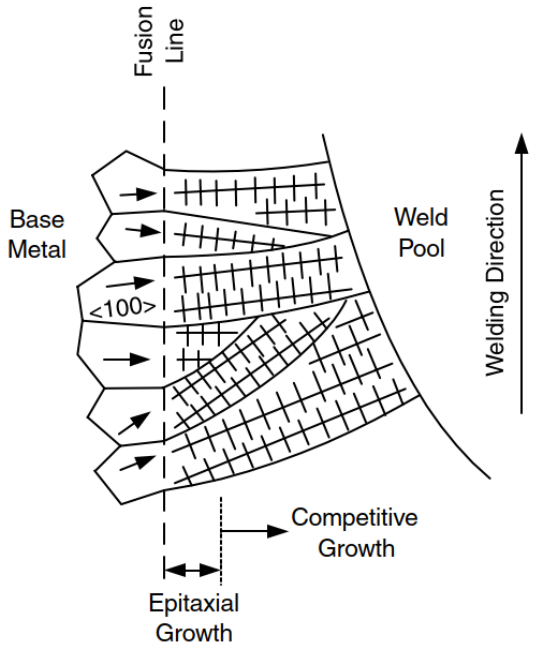

Figure 3.4: *Epitaxial and competitive growth in fusion zone* [49].

3.2 Partially melted zone

Partially melted zone (PMZ) is the area adjacent to the fusion zone, presence of liquation is the evidence of the existence of PMZ. The heat transferred in the PMZ is not enough to completely melt the base metal, but it is above the eutectic temperature and phases in PMZ consists of solid and liquid.

Kou [49] explains that how concentration gradient can occur in the PMZ, he explains five different mechanisms about the formation and changes in concentration in the PMZ upon reheating and then cooling. However, the mechanism of 'grain boundary segregation' is considered as a more favorable approach in the concentration gradient in PMZ. Elements that have the tendency to segregate at grain boundaries include phosphorous, silicon, and nitrogen [52]. Grain boundary segregation explains that upon reheating and cooling the matrix rejects the solute and solidifies as 'hypoeutectic' while solute rich phase solidifies as 'hypereutectic' and this contributes to change in concentration [49].

3.2.1 Hydrogen cracking in PMZ

Intergranular hydrogen cracking can occur in the PMZ, as hydrogen can easily diffuse in the liquid phase of the PMZ, see Figure 3.5. Liquidated grain boundaries serve as pipelines for hydrogen to diffuse in the PMZ, this is because liquid metal has higher capacity to allow hydrogen to diffuse through as compared to solid iron. When this solute segregated and hydrogen rich liquid solidify, it provides nucleation sites for hydrogen cracking to occur in the PMZ [49].

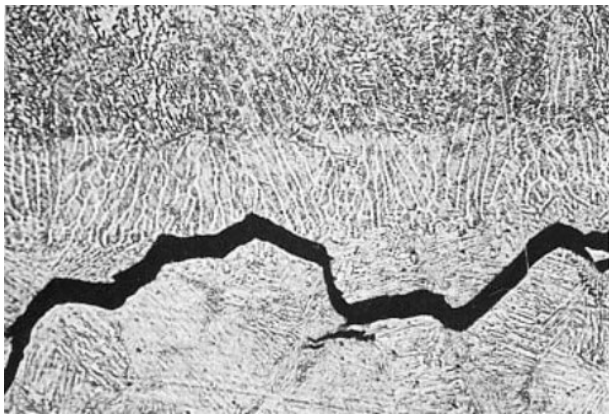

Figure 3.5: *Hydrogen cracking in the PMZ of HY-80 welded steel* [49]

3.3 Heat affected zone

Heat affected zone (HAZ) is the area that occurs after the PMZ during welding. The heat in HAZ is not enough to melt the base material but it is sufficient to cause significant structural changes. The hardness of work hardened, transformation hardened and precipitation hardened steels can decrease in the HAZ; because during reheating and cooling in HAZ grains undergo recrystallization and growth that suppresses the hardness values [49]. As a consequence of heating and rapid cooling, a variety of microstructures can occur in HAZ depending on the alloy. Strength and ductility of steels are considerably reduced and cracks can initiate in HAZ [53].

One tool for estimating microstructure of HAZ is by the use of continuous cooling transformation (CCT) diagrams. CCT diagrams were generated by continuously cooling austenite at different cooling rates; So, these diagrams help in better understanding of the welding conditions. These diagrams consist of phases which include, bainite, pearlite, ferrite and martensite; the diagram also uses martensite start (Ms) and martensite finish (Mf) temperatures [18].

As described above, the region of HAZ suffers a heating and cooling cycle; heating from the fusion zone and cooling from the base metal. The heating rate decrease as the distance from the fusion boundary increases, see Figure 3.6. This makes it important to determine the cooling rate because it is less sensitive to the distance from fusion boundary. The time taken to cool from 800°C-500°C ($T_{8/5}$) is particularly important. For many steels that are utilized in welding, this time represents the solid-state transformation of austenite. Two parameters can be utilized to determine the thermal cycle in HAZ; peak temperature (Tp) and $T_{8/5}$. Both these parameters depend on the heat input to estimate the thermal behavior of HAZ; the relation of heat input with Tp and $T_{8/5}$ is given in equations 3.1 and 3.2, where ‘q’ represents heat input, ‘r’ represents distance from the fusion boundary and ‘n’ represents constant for thickness in relation to the weld bead and value of ‘n’ can be 1 or 2, depending on the thickness of specimen to weld bead ratio [48].

$$Tp \propto q/r \quad (3.1)$$

$$T_{8/5} \propto q^n \quad (3.2)$$

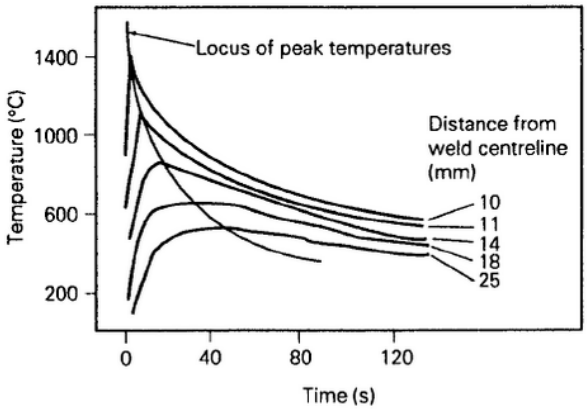

Figure 3.6: *Curves representing the thermal cycle of welds in HAZ* [48]

Quench and tempered steels are more prone to form martensite in HAZ, because of the presence of chromium, nickel and molybdenum. Because of these alloying elements, un-tempered martensite can form at an increasing rate in quench and tempered steels. This untempered martensite is very brittle with poor toughness and contains residual stresses; this untampered martensite can lead to cracking in HAZ [18].

Studying the hardenability is also a key parameter, since it describes the depth of formation of martensite in HAZ. CCT diagrams are used to predict the hardenability in HAZ and utilizes the time between Ms and Mf temperature to predict it. Hardenability can depend on some factors that include content of alloying element, carbon percentage, grain size of austenite and thickness of specimen [18]

Hardness of the martensite in HAZ is of particular importance; since, higher hardness of un-tempered martensite can often result in cracking. Higher percentage of carbon leads to higher content of martensite [18] , see Figure 3.7. That is why it is a challenge to weld large thick sections that contain carbon percentages higher than 0.45% [48]. Based on the carbon percentage in the base metal, hardenability of different steels can be compared. International Institute of Welding (IIW) have derived a formula to estimate carbon equivalent (CE) in carbon steels that utilizes carbon percentages and other alloying element percentages to compare the hardenability. The formula is given in equation 3.3; the formula is useful to judge that if preheating or post treatments are required after welding. For example, if the CE is less than 0.35 than no preheating is required; if the CE is between 0.35-0.55 than preheating is required but post treatment is not necessary. If the CE is higher than 0.55, in that case both preheating and post treatments are advisable [18, 48].

$$CE_{IIW} = \%C + \%Mn/6 + \% (Cr + Mo + V)/5 + \% (Si + Ni + Cu)/15 \quad (3.3)$$

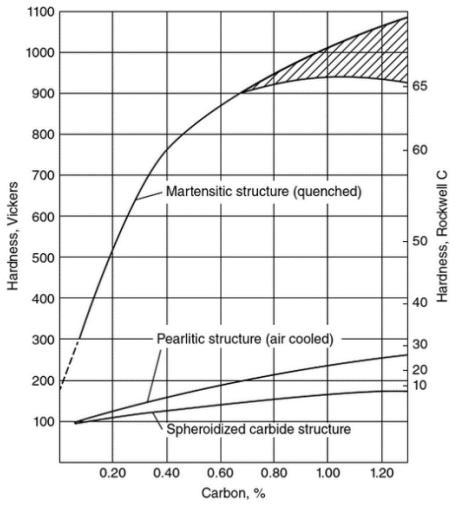

Figure 3.7: *Hardness of different phases in relation to carbon content* [18].

Various structural changes are observed at different levels of HAZ, these levels have different structure, hardness and toughness values from one another. Because of these changes, HAZ is further categorized into three subzones; coarse grain (CGHAZ), fine grain (FGHAZ) and inter-critical (ICHAZ) [54], see Figure 3.8 and 3.9. These zones are discussed in the following sections. Subcritical HAZ is considered as a part of ICHAZ, so it is not described separately.

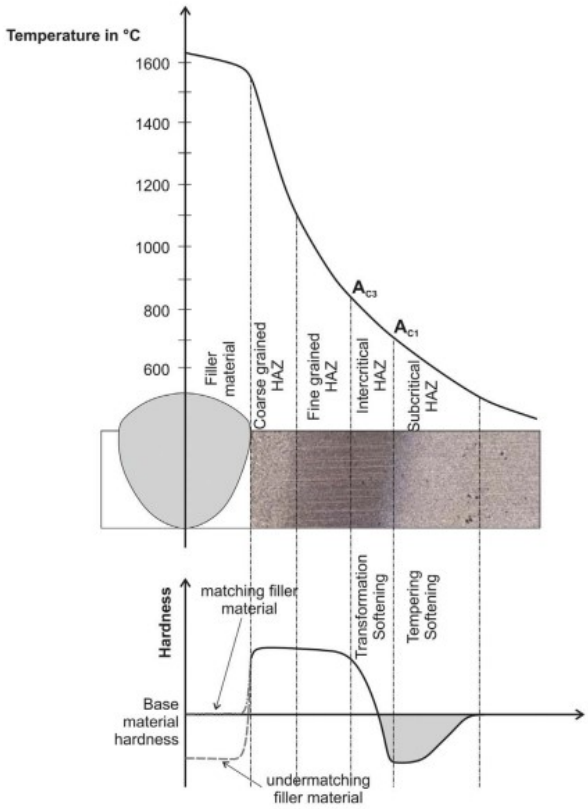

Figure 3.8: *Subzones of HAZ according to iron carbide diagram, with their subsequent hardness [54]*

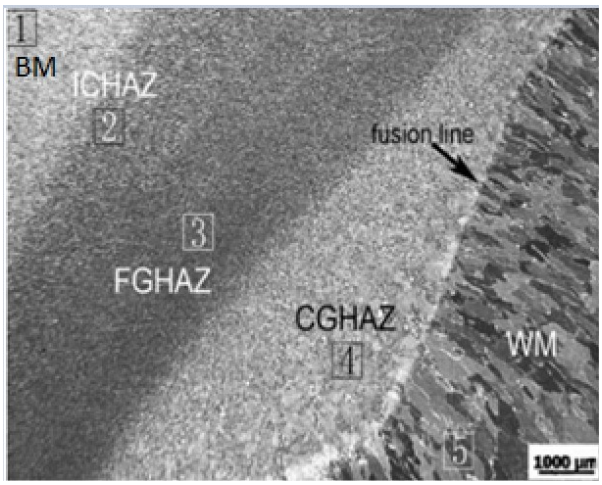

Figure 3.9: *Optical micrograph of zones in a weldment and subzones of HAZ* [55]

3.3.1 Coarse grain heat affected zone

This zone is present next to the PMZ, the temperatures in this zone can reach to around 1250°C (>Ac3). Structures for steels in this region mainly include bainite and martensite, but small amounts of δ ferrite can also be present [56]. Yanet et al. [56] explains the phenomenon of high hardness (as compared to other HAZ subzones) and coarse grains in this zone. They propose that coarse grains ae due to high temperature, and reheating due to very high temperatures dissolves the existing precipitates of steel in the coarse grains. Although in theory, the hardness of coarser grains should be less than fine grains, but precipitate dissolution in grains increases the hardness of this zone.

Lan et al. [55] and Qiu at al. [57] focused their attention on determining the impact toughness values in CGHAZ, as according to them crack propagation in subzones of HAZ depends on toughness. Qiu et al. [57] have shown that impact toughness in CGHAZ is lower as compared to FGHAZ, they explain that lower impact toughness is due to the large martensite-austenite constituents; upon reheating and rapid cooling partition of carbon and silicon occurs and carbon-rich austenite transforms to martensite and carbon deficit region transforms to bainite, the amount of austenite transformed to martensite is termed as 'martensite-austenite constituents'(M-A constituents). Lan et al. [55] observed that highest amount of M-A constituents are present on the coarse grain boundaries in the CGHAZ, they also concluded that cleavage fracture occurs in the CGHAZ and the initiation sites are the M-A constituents on the grain boundaries.

3.3.2 Fine grain heat affected zone

Temperatures in FGHAZ can reach around Ac3 (~912°C), precipitates are not usually dissolved in this zone, the hardness is a bit low than CGHAZ and the creep resistance of this region is low. The grain size in FGHAZ is small and the properties of this zone lies between CGHAZ and ICHAZ. As there is not a complete dissolution of precipitates, the

structures differ from CGHAZ [56]. The microstructure of FGHAZ consist of granular bainite, polygonal ferrite (massive ferrite) and acicular ferrite [55, 57].

Lan et al. [55] and Qiu at al. [57] made comparisons of the impact toughness between CZHAZ and FZHAZ. They revealed that impact toughness of FZHAZ is higher as compared to CZHAZ, they present two main reasons for this phenomenon. First reason being low constituent of M-A, less amount of M-A constituent than CZHAZ results suppressed amount of crack initiation sites and toughness is higher. Secondly, due to the presence of acicular ferrite; acicular ferrite hinders the crack propagation due to its high angle grain boundaries. They further explain that acicular ferrite grows on the boundaries of precipitates and increasing the amount of Ti, Al, Mn and Si can encourage the growth of acicular ferrite and inhibit crack propagation. Lan et al. [55] explains that fracture surface of FGHAZ contained features of quasi-cleavage and ductile fracture as compared to cleavage fracture in CGHAZ; they concluded that this mechanism of quasi-cleavage is due to the presence of high angle misoriented grain boundaries of acicular ferrite.

3.3.3 Intercritical heat affected zone

This zone is characterized by its partial transformation from ferrite to austenite, the temperatures in this region are between Ac1 and Ac3(~900-700°C). As new austenite grains are formed, prior martensite can undergo tempering and also precipitate redissolution can occur. This zone has the lowest hardness and impact toughness among the subzones of HAZ and this area is prone to creep failures [56]. The microstructure of ICHAZ consist of granular bainite, quasi-polygonal ferrite and M-A constituents [55].

Li et al. [58] have explained the reason for low impact toughness in ICHAZ. They have further divided the ICHAZ into three zones according to temperature; 912-830°C, 830-770°C and 770-700°C. According to them the impact energy is the lowest in the region of 830-770°C and primary reason being M-A constituents. It was found that M-A constituents emerge in the microstructure above Ac1 and they attain a critical size in the temperature range of 770-830°C, while above 830 M-A constituents form a slender shape and starts to settle on grain boundaries. Li et al. [58] concluded that the critical size of M-A constituent is 3µm and it is primarily responsible for low impact toughness. Although they did not explain completely the relation of M-A constituents and impact toughness but one hypothesis could be that occurrence of twinned martensite in M-A constituent may be the reason of low impact toughness.

3.4 Effect of preheating

Cold cracks in welding are important to take in consideration and also crucial to adopt counter measures to avoid weld cracking. Cold cracking in welding can be a result of entrapped hydrogen, formation of martensite in HAZ and thermal stresses [59-61]. Marcus [59] has described in his article that preheating can be effective in hydrogen escape

from the weldment and prevent cracks due to hydrogen embrittlement. Baek et al. [60] deposited metal powder on tool steel to produce a hardfacing by laser cladding with varying preheating temperatures. They concluded that higher preheating temperatures can suppress thermal stresses, as the cooling rate of the substrate is low. They observed that dendritic morphology at the interface did not exist at a preheating temperature greater than 300°C and instead was replaced by cellular grains. Lai et al. [61] explained that suitable preheating temperature at a higher depth would inhibit the growth of martensite in HAZ and prevent cold cracks.

Preheating temperatures can be different for each material and can depend on several factors. Marcus [59] lists factors that can influence the preheating temperature, they include:

- The carbon equivalent of the base metal and the weld metal.
- Type of weld joint and thickness of the weldment area.
- Heat input by the welding process selected.
- Transformation and shrinkage stresses
- Diffusion rate of hydrogen in the weld metal and base metal.

4. EROSION WEAR

Erosion wear is degradation of material by the impact of flowing particles under the influence of fluid travelling at significant velocity. Erosion is encountered in various machineries, examples include; erosion of turbine blades by dust in an aircraft, erosion of hydro-turbines by sand particles and degradation of pump impellers in mineral processing. In many cases, the material removal by erosive wear is small but collective damage is significant. If erosive are solid particles then mechanism similar to abrasion will occur, if liquid is involved then wear takes place by repetitive impacts. In order to prevent erosion; the study of erosion mechanism is necessary, mechanisms of wear by erosion is shown in Figure 4.1. Different mechanisms are involved in erosion and depends on various parameters [62], these are discussed in detail in the following sections.

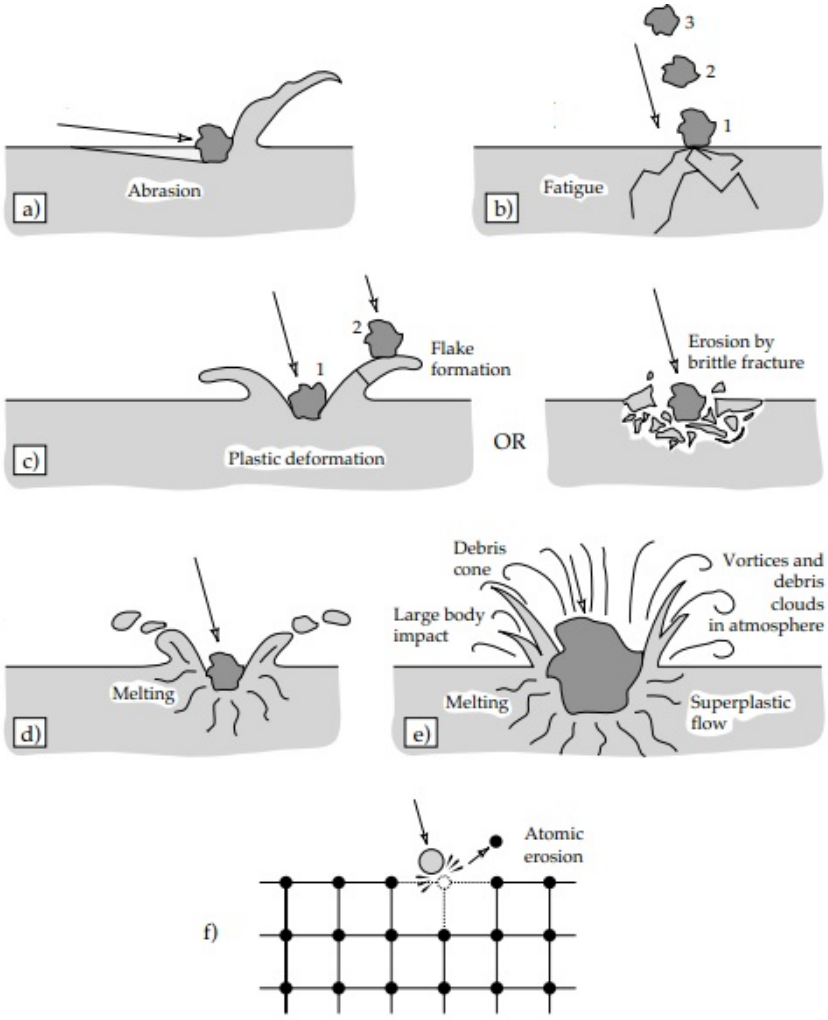

Figure 4.1: *Erosion mechanisms:(a) abrasion, (b) surface fatigue (c) brittle fracture or plastic deformation (d) melting (e) macroscopic erosion with secondary effects (f) crystal lattice degradation from impact by atoms* [62]

4.1 Effect of particle angle

Particle impingement angle can vary between 0 to 90°. It is found that at low impingement angles (<30), ductile materials undergo severe loss by erosion, where as brittle materials suffer high wear rates at high impingement angles [62], see Figure 4.2. This study was also confirmed by Kleis et al. [63], when they experimented 0.2%C steel with different abrasives at an angle of 0-90°, Figure 4.3. They proposed that at certain threshold velocity cutting component is dominant in ductile and soft materials by sharp edge particles while, high wear rate is encountered in brittle materials by impact component.

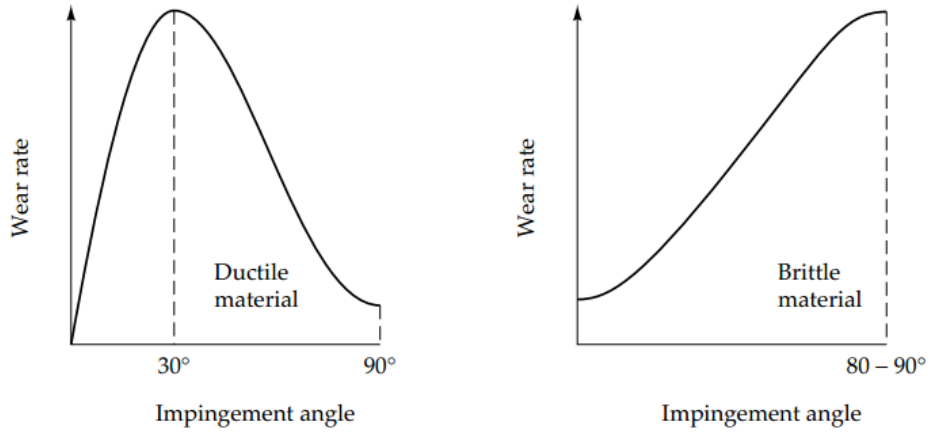

Figure 4.2: *Effect of impingement angle on ductile and brittle materials* [62]

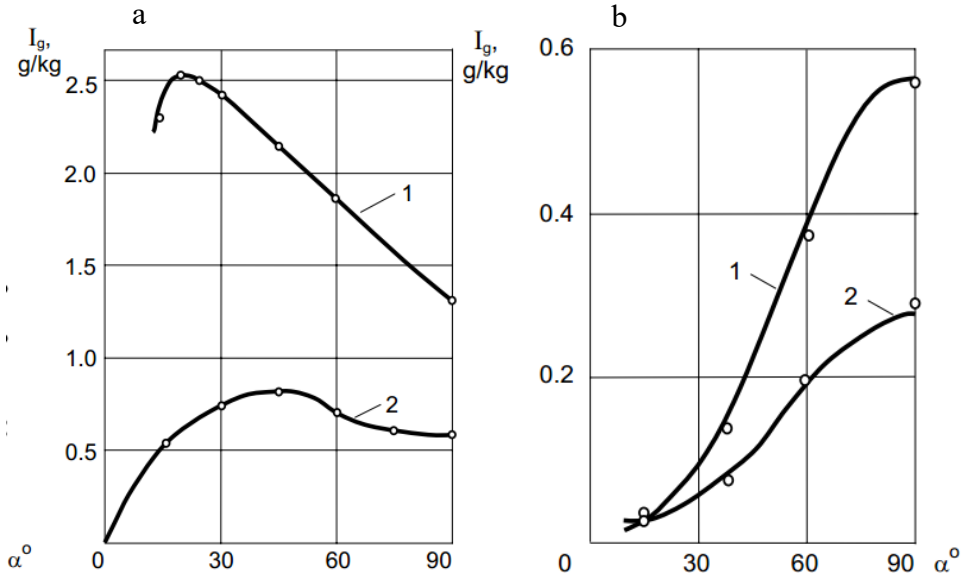

Figure 4.3: *Effect of impingement angle on ductile and brittle materials (a) wear rate of 0.2% C steel , (b) wear of brittle materials, (1) glass grit and (2) corundum* [63]

4.2 Effect of pressure/velocity

Particle velocity at the point of impact on target has the dominant influence on erosion rate among other parameters. There is a certain threshold velocity at which wear rate is negligible irrespective of the angle [62]. Kleis et al. [63] experimented the erosion rate of mild steel at different velocities with three different abrasives at an impact angle of 90°, see Figure 4.4. Stachowiak et al. [62] proposes a formula for determining wear rate above a certain threshold velocity. The formula is presented in equation 4.1.

$$-dm/dt = kv^n \tag{4.1}$$

Where m represents 'mass loss', t equals 'time duration' of the test, k is the 'empirical constant', v shows 'velocity of the abrasives' and n is the velocity exponent.

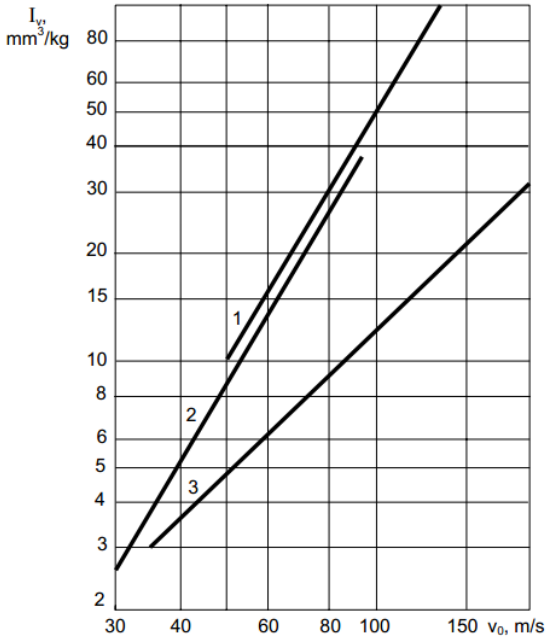

Figure 4.4: *Effect of velocity on wear rate of mild steel at impact angle of 90°. Three curves represent different abrasives; (1) quartz sand, (2) quarry sand and (3) river sand* [63]

Islam et al. [64] studied the combined effect of impingement angle and particle velocity on the wear rate of X42 pipeline steel using alumina as abrasives. According to them, at low impact angle and at low velocities (~30-40m/s) metal ploughing was the erosion mechanism, however it was also observed that alumina particles were embedded on steel under these conditions. At low impact angle and high velocities (81m/s), the wear occurred by metal cutting which were 3-5µm in size. Under these conditions, erosion occurs by fracture of ridges, material degradation by brittle fracture occurs by repeated impacts from abrasives; in certain cases, work hardened layer is also observed at high velocities at different impact angles, see Figure 4.5. Islam et al. [64] have also discussed the effect

of high impingement angle with high and low velocities on the wear rate. At 90° angle and low velocity it was observed that, alumina particles embedded into the steel matrix and resulted in ridges around dimples and material removal occurred by fracture of ridges. At high velocity and 90° angle, erosion occurred in a similar manner to low velocity, but high erosion rate was observed due to damage of embedded alumina in the steel matrix by incoming particles that led to secondary cutting.

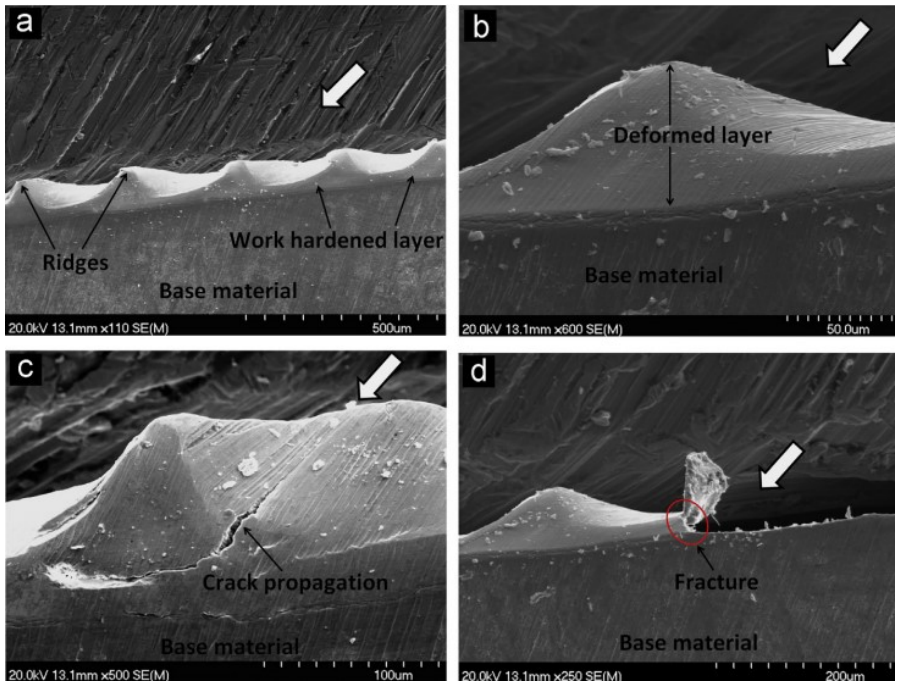

Figure 4.5: *SEM images of erosion mechanism of X42 steel at low angle and high velocity, (a) series of ridges on work hardened layer (b) deformed layer of steel (c) subsurface crack propagation (d) material fracture* [64]

4.3 Effect of particle size

Alteration in particle size can cause changes in the wear rate and can also affect the wear mechanism. Figure 4.6 shows the erosion behavior of various materials tested with a particle size distribution of 8.75-137µm against different impingement angles at a velocity of 152m/s. It can be observed that particle size not only affects the wear rate but also has significant impact on the wear resistance of materials. The factors including work hardening and toughness can also affect these results. The materials which are neither hard nor tough inhibit higher wear rates [62].

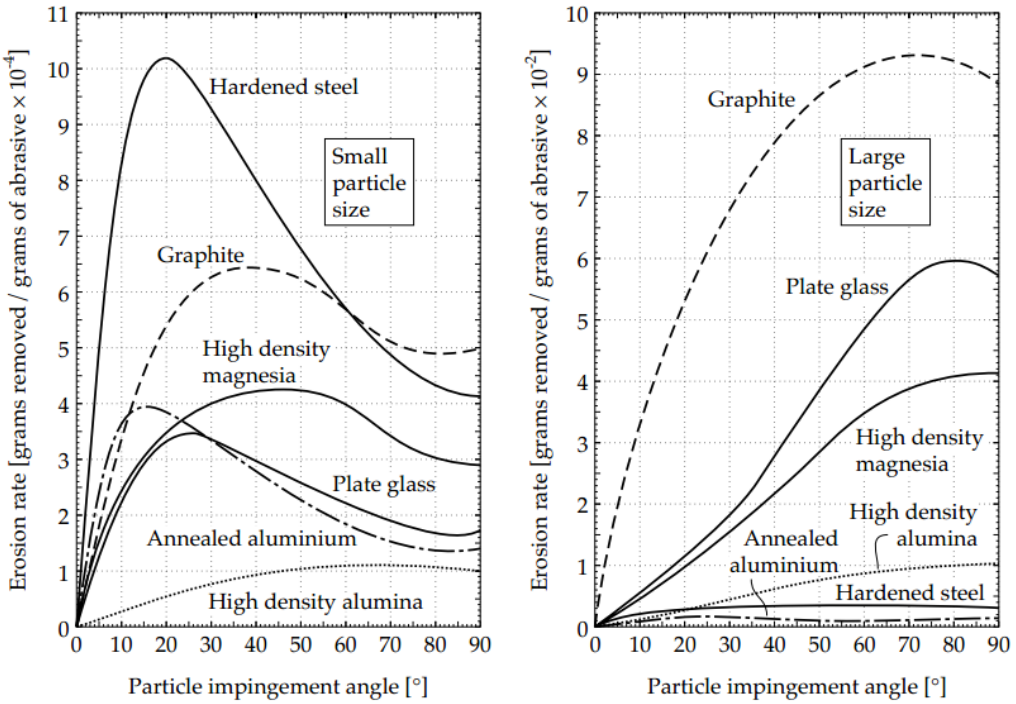

Figure 4.6: *Erosion rate of different materials with small and large particle size* [62]

4.4 Effect of erosive type

Properties of abrasives offer a considerable effect on the wear rate; it is stated by Satchowiak et al. [62] that particle hardness and shape can cause alteration in the erosion rate. The ratio of abrasive hardness to target material hardness is the controlling parameter and can be utilized to suppress wear rates. Hardness of particles also effects the mode of wear i.e. ductile or brittle. Hardness of particle has a much more severe effect on the brittle mode of fracture as compared to ductile mode. Particle shape can also have an impact on the wear rate; sharp particles with low hardness show higher wear rates than blunt particles with higher hardness [62].

5. MATERIALS AND METHODS

This chapter describes the materials that were used as base materials, filler wires for cladding and method adopted for hardfacing. The chapter also discussed different methods that were selected for examining the hardfaced coatings to determine their behaviour under high impact forces and high velocity erosive wear conditions. Additionally, the characterization methods adopted to analyse the samples are also mentioned in this chapter.

5.1 Base materials

There were two steels used to serve as base materials for hardfacing. One material was quench and tempered steel and other one is 42CrMo4 steel. The elemental composition is presented in Table 5.1. As described before, the hardfaced coatings had to be evaluated for their properties and wear resistance in as clad and heat-treated conditions. So for this purpose, both steels were selected in their non-heat-treated and heat-treated states. Both materials were received in bars, Figure 5.1 shows an image of 42CrMo4 bar.

Table 5.1: *Composition of quench and tempered steel and 42CrMo4*

Base materials	% C	%Si	%Mn	%S	%Cr	%Ni	%Mo	% Fe
Q and T steel	0.45	0.35	0.8	0.05	1.5	-	0.4	Bal.
42CrMo4	0.41	0.30	0.7	-	1.1	-	0.2	Bal.

Figure 5.1: *Image of 52×10×2.2cm 42CrMo4 bar*

5.2 Hardfacing wires

Four hardfacing were chosen in the form of tubular wires, see Figure 5.2, for examining their impact wear resistance and erosive wear resistance. The materials were chosen due to their higher wear resistance (according to the manufacturer) and availability; the wires were purchased from Durum GmbH. Two nickel alloys reinforced with tungsten carbide

powders and two iron based alloys were selected as materials to be deposited as hardfaced coating. Throughout the thesis report the alloys will be regarded with their commercial names as described by the manufacturer. The description of the alloys with their commercial names is discussed in the following sections.

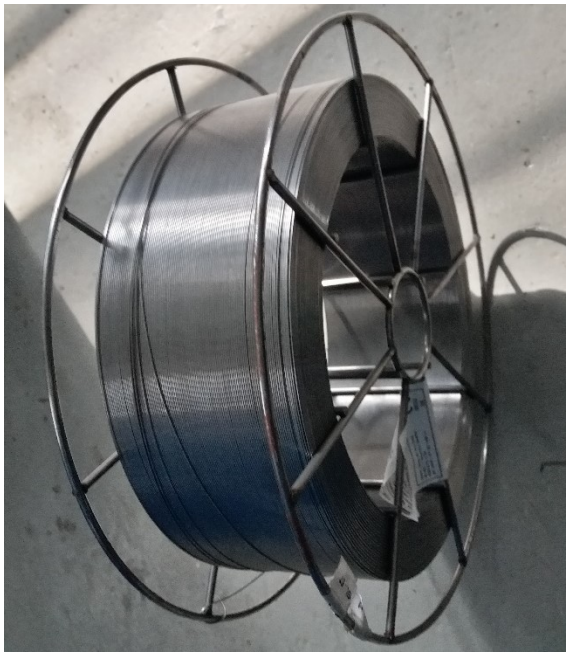

Figure 5.2: *Hardfacing tubular wires*

5.2.1 Nickel based wires

Two nickel based wires reinforced with spherical tungsten carbide (WC) powders were used as hardfacing deposits in this thesis. The difference between the two wires lie in the **diameter of the wire** and size of tungsten carbide powders; the diameter of one wire was 1.2 mm while the other had a diameter of 1.6mm. The commercial name of the 1.2mm diameter wire is **NI2 PLUS**, while the other is known as **NIFD PLUS** commercially. The matrix of both alloys included consist of Ni-Cr-B-Si and the reinforcement is composed of spherical WC powders with varying size. The ratio of alloying elements in the matrix is not same in the two wires. According to the manufacturer, NI2 PLUS also contains some other special carbides which have a hardness in the range of 3000 $HV_{0.1}$.

5.2.2 Iron based wires

Two iron based alloys were also selected to be hardfaced for this work. **FD65** and **FD605** are the commercial names of these wires and the diameter of both wires is 1.2 mm. FD65 is a hyper eutectic high alloyed wire, while FD605 is a hypoeutectic low alloyed wire consisted of some special carbides. The chemical compositions (in wt. %) of both wires is given in Table 5.2.

Table 5.2: *Composition of iron based hardfacing wires.*

Alloys	%C	%Si	%Mn	%Cr	%Mo	%Nb	%V	%W	%S.C	%Fe
FD65	5.2	1	0.4	21	7	7	1	2	-	Bal.
FD605	2.6	-	-	7	1.3	-	-	-	10-12	Bal.

5.3 Cold metal transfer welding equipment

The cladding was performed by Cold Metal Transfer welding, the theoretical details of the process is discussed in section 2.1.4. The CMT equipment is placed in the laboratory of mechanical systems and technical services at Tampere University (Hervanta Campus).

Fronius® explains a general display of CMT equipment through a schematic diagram presented in Figure 5.3. The CMT welding equipment consist of (1) Microprocessor and digitally regulated GMA power source (3200/4000/5000 A), (2) Remote control for welding and weld data monitoring, (3) FK 4000 R cooling unit (4) robot controller, (5) VR 7000 wire feeder, (6) digitally controlled welding torch, (7) wire buffer, (8) wire supply.

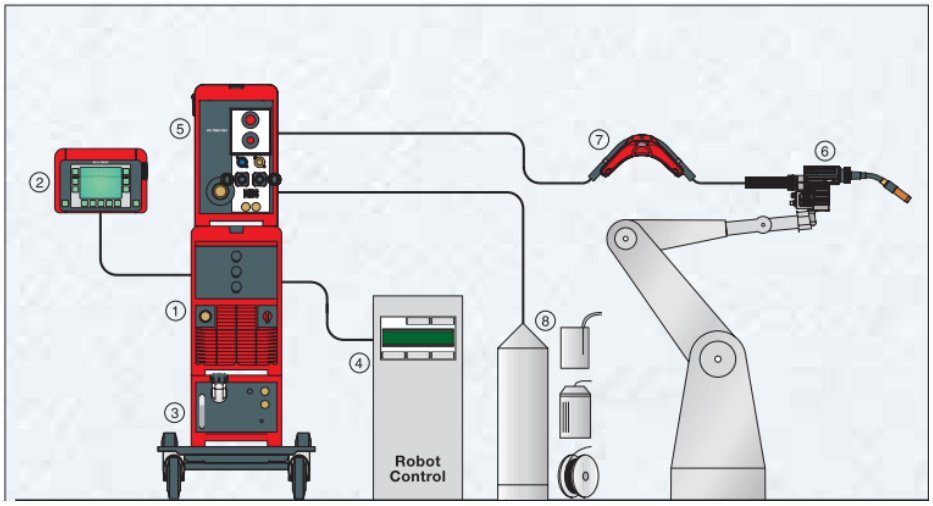

Figure 5.3: *Schematic diagram of CMT equipment* [23]

The CMT welding equipment in Tampere University is a TPS 4000A power source with a working voltage of 7-34 volts. The equipment is automated and controlled by ABB IRB 4600-40/2.55 robot, see Figure 5.4. The robot is able of perform welding in 6d motions and controlled by RCU 5000i remote control. The robot also includes a table where welding is performed. The table is also grounded with one end of the power source for welding operations. The table has an additional feature of rotating, which can be utilized during additive manufacturing.

Figure 5.4: *CMT equipment at Tampere University*

5.4 Hammer Mill impact wear tester

Hammer Mill equipment belongs to Tampere Wear Center (TWC), which is placed in Tampere University, Hervanta campus. Hammer Mill is used make large impacts on the selected materials, which is used to characterize impact wear. The hammer mill can work on a wide range of impact energies, which can be calculated from the frequency of the impacts and the angular velocity. Abrasive particles can also be introduced with the impact forces, this feature is used to characterize 3 body abrasion mainly occurring in crushers. A schematic diagram of hammer mill is presented in Figure 5.5.

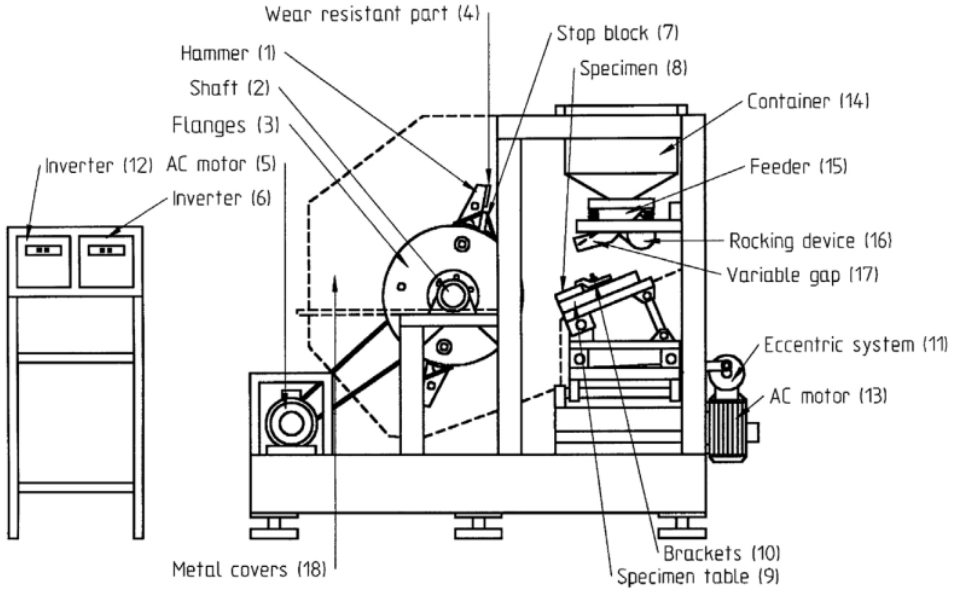

Figure 5.5: *Schematic diagram of hammer mill equipment* [65]

From Figure 5.5, it can be seen that AC current provides power for the rotation of the shaft. Alteration of the frequency in the AC power supply is used to alter impact energies. The hammer, Figure 5.6, is attached to the end of the shaft by a connecting rod; there are two connecting rods joined with the shaft, so every rotation results in two impacts. The specimen to be tested is placed on a table (9), the table is inclined and pivoted to a flat load carrying block. It is possible to change the impact angle by changing the size of the pivots. Abrasives (if needed) are introduced from above, the feed rate can be changed by adjusting the opening of the abrasive container.

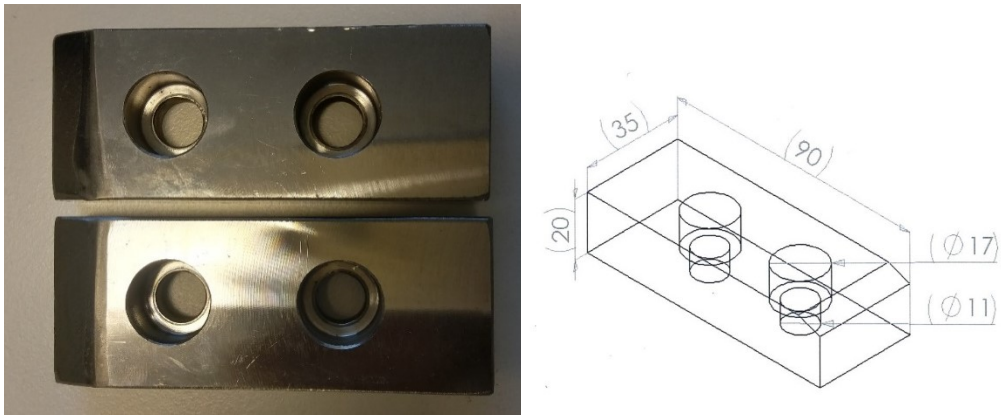

Figure 5.6: *Hammers used in hammer mill*

The objective to use hammer mill test in this work was to carry out the mass loss of the hardfaced coating under high impact forces. As the weld overlay was restricted to a single layer, it was important to know the mass loss under extreme conditions. Another task from the hammer mill test was to observe the occurrence of cracks in the HAZ after exposing to large impact forces.

5.4.1 Hammer Mill impact test procedure

It was planned that hammer mill test will be conducted at a frequency of 7.5Hz and 10.5Hz on the four weld hardfacing alloys for three hours and mass loss would be calculated after every 30 minutes. The angle of impact in the 7.5Hz test will be 90˚, while the angle of impact in the 10.5Hz frequency will be 65˚. So, a total of 16 tests had to be conducted with the hammer mill test; 8 tests with 7.5Hz of the four alloys in as clad and heat-treated conditions and 8 tests with 10.5Hz in their as clad and heat-treated states.

5.5 Pulse Jet erosion wear test equipment

To characterize erosion under zero and ninety degrees, Pulse Jet equipment was employed, see Figure 5.7. The pulse jet is designed to characterize wear occurring under high pressure air supply with a wider particle size distribution at parallel and perpendicular impingement angles.

Figure 5.7 shows the pulse jet equipment, which is placed at Tampere University. The chamber contains the nozzle and the sample holder; the chamber has a capacity to contain 5-10 kg of erosive particles depending on the size distribution. Air is supplied by the nozzle in the chamber; the air pressure is controlled by a pressure valve which is connected to a small air tank. The air tank is used to supply air at a constant flow with pressure controlled by pressure valve; 6 bar air pressure was used to test specimens in this thesis. The zero degree specimen holder is designed to hold only certain dimension specimens. 240 mm length and 20 mm wide flat specimens with thickness of 5-20mm, so the specimens had to be machined according to the dimensions dictated by the pulse jet specimen holder. According to the previous research conducted by pulse jet, the actual impingement angle for parallel specimen holder is 1.15˚, but in this work the impingement angle will be referred to as 'zero degree' or 'parallel' since the angle is too low. The other specimen holder is placed at the top of the chamber which is used for characterization of 90° impingement angles; the dimension of perpendicular specimen is not restricted as different height and width can be used, but the length must not exceed 90mm. The 0° specimen holders also has ledges attached which protect edge wear along the 240 mm length for both specimens, see Figure 5.8.

The pulses are created by the opening and closing of the relay which is controlled by the microcontroller, the amount of pulses can also be selected from the microcontroller; the current setting of microcontroller operates at 10Hz frequency cycle with same open and close time. The microcontroller is attached to a DC power supply, for some reason the relay seems to work when the voltage set is above 5 volts.

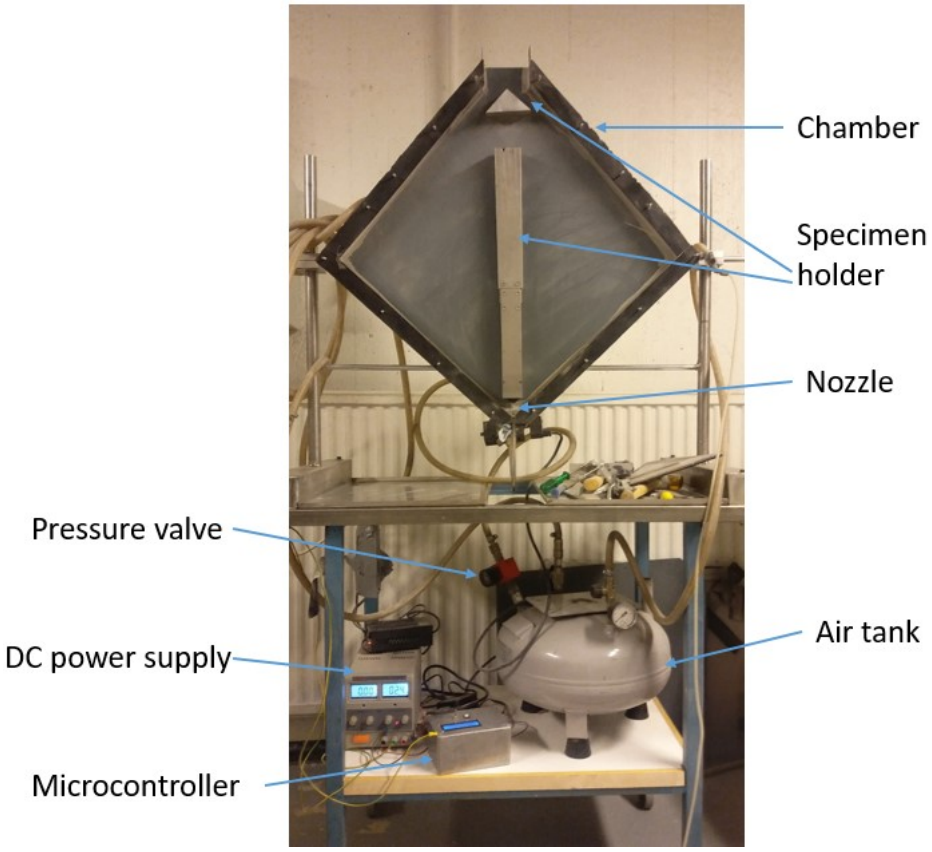

Figure 5.7: *Pulse Jet equipment*

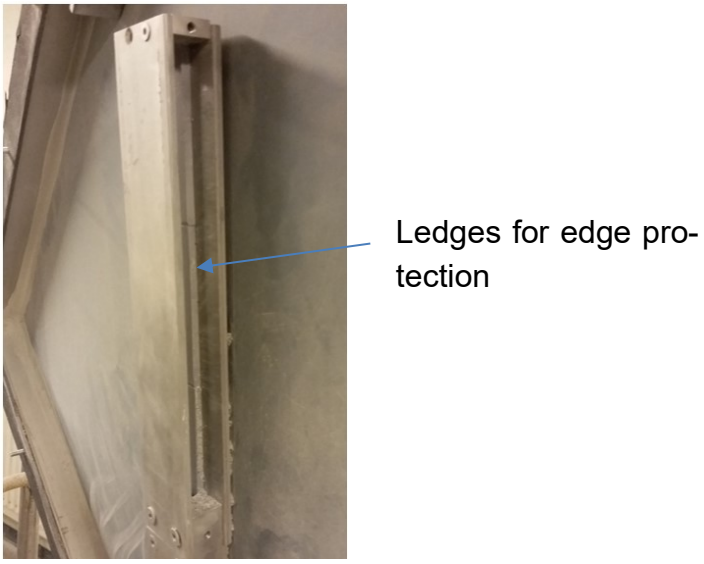

Figure 5.8: *Tungsten rod welded to the specimen holder for edge protection*

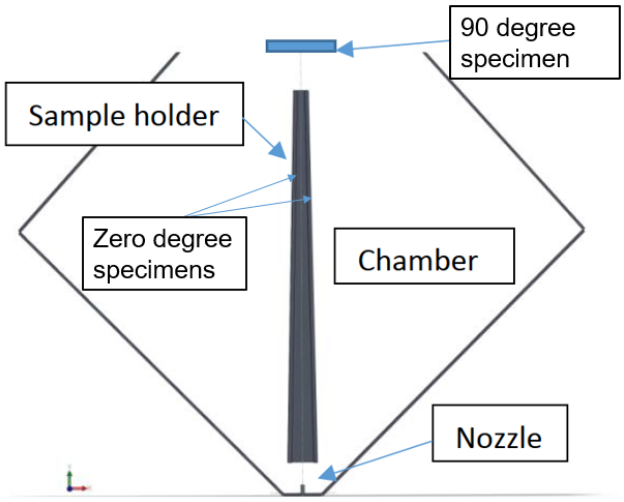

Figure 5.9: *Schematic picture of the Pulse Jet*

The working of the equipment is quite simple; the chamber is filled with erosive particles of intended size distribution. When the pulses are turned on the particles move upwards with a high velocity hitting the 0° specimens first and then interacting with 90° specimens until falling back to the chamber under gravity. The cycle goes on until the desired pulses are completed. The test creates lot of dust, specially from the small particles, so ventilation is provided at the top the equipment.

As described in section 4.2, velocity of the abrasives has a dominant effect on the wear rate of the specimens, so it is important to determine the velocity of the erosive particles that travel under a pressure of 6 bar in pulse jet equipment. The measurement of velocities was determined by previous research conducted on the pulse jet; the research was conducted for volumetric measurement for air escaping under 10 pulses. This led to the measurement of velocity of air under constant pressure (6 bar) after acquired time of 1.2 and 3ms. Average of particle size was considered for determining the particle velocity in precious studies. However, when larger particles are used as abrasives (>2mm), the particles velocity is in the range of 15-25m/s under a pressure of 6 bar.

5.5.1 Pulse jet erosion wear test procedure

Every hardfacing alloy, in their as clad and heat-treated condition, had to be experimented with the pulse jet equipment at 0˚ and 90˚ erosion tests. The tests were planned to be carried out at a pressure of 6 bar, under 40,000 pulses and mass loss would be measured after every 10,000 pulses. Granite particles of size <4mm were selected to be used as erosive particles.

5.6 Characterization Techniques

Various characterization techniques were utilized for analyzing cladding of hardfacing alloys, hammer mill specimens and pulse jet specimens. Microstructure images of cladding was analyzed by optical microscopy and Scanning Electron Microscopy (SEM). X-ray diffraction and Energy Dispersive X-ray Spectroscopy (EDS) was conducted on all hardfacing specimens, in as clad and heat-treated states, to study the microstructure and phase analysis in detail and also to observe the changes occurred in the microstructure after heat treatment. Hardness measurement were carried out by Vickers hardness and Zwick hardness tester; the surface crack density was conducted by stereomicroscopy. In addition, hammer mill specimens and pulse jet specimens were analyzed for their wear depth after testing through optical surface profilometer (Alicona), Figure 5.10 shows an image of optical surface profilometer.

Figure 5.10: *Image of optical surface profilometer*

6. CLADDING OF HARDFACING ALLOYS

Cladding had to be carried out on heat-treated and soft base materials for four hardfacing wires. The aim was to use quench and tempered steel in pulse jet test, while 42CrMo4 was planned to be used in hammer mill test.

As described in chapter 3, welding can result in cracking in the PMZ and HAZ, so to avoid cracking preheating was conducted prior to cladding. The preheating method and equipment is described in the following section.

6.1 Preheating

Advantages of preheating are described in section 3.4, it is evident that preheating can prevent cracks occurring due to temperature gradient, hydrogen and cold cracks. The estimation of correct preheating temperature is necessary for cracks prevention; the preheating temperature was selected to be 250˚C, which was calculated on the basis of carbon equivalent in the base material. The details of the calculation of the preheating temperature can be found from reference [59]; a graphical representation of the estimation of preheating temperature is presented in Figure 6.1. A portable heating device was used to heat the base materials before cladding.

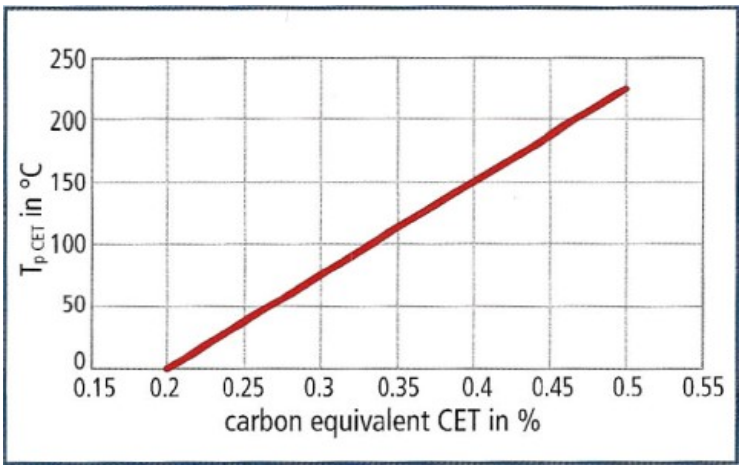

Figure 6.1: *Graphical representation of estimated preheating temperature based on carbon equivalent* [59]

6.2 Cladding

Cladding of the four hardfacing wires was conducted on the preheated base materials by CMT, the parameters were adjusted for the four different alloys, see Table 6.1. Some experience is required for selecting the cladding parameters of each hardfacing alloys, as

each alloy has different elemental composition and properties. All the claddings were deposited by weaving mode with an overlapping of 50% in multi beads. The width of single weld weave bead of FD605 is 16mm, while other alloys comprise of a weave bead of 4mm. The single weld weaving bead of FD605 is large, as compared to other alloys, that is why the velocity of deposition is kept low. As can be seen from Table 6.1, that wire feed rate (WFR) is comparatively low for NIFD PLUS, the main reason is due to a large diameter of 1.6mm. Mison 2 and Mison 8 shielding gases were used during the cladding; Mison 2 includes Ar, 0.03% NO and 2% CO_2, while Mison 8 consists of Ar, 0.03% NO and 8% CO_2.

Table 6.1: *Cold Metal Transfer welding parameters for different hardfacing alloys*

Alloys	**Wire Diameter (mm)**	**Mean Wire Feed Rate (WFR), m/min**	**Mean Voltage (volts)**	**Mean Current (ampere)**	**Travel Speed (mm/sec)**	**Shielding gases**
NI2 PLUS	1.2	5.6	14.2	164	10	Mison 2
NIFD PLUS	1.6	3.5	12.5	192	10	Mison 8
FD65	1.2	4.3	16.5	153	10	Mison 2
FD605	1.2	5.5	15.3	155	2.8	Mison 2

First the cladding was completed on 42CrMo4 bars (soft and heat-treated) to complete specimens required for hammer mill test. NI2 PLUS was the first hardfacing wire to be cladded, then FD65, FD605 and NIFD PLUS was the last one; the parameters are listed in Table 6.1. On a single 42CrMo4 bar, three claddings were completed for hammer mill specimens along with a cross section specimen (for microscopic study); the three claddings were separated from each other by a distance of 20mm. The clads were separated by saw cutter to obtain individual hammer mill specimen. Each hammer mill specimen had a weld bead length of 77mm, and total width varied with the number of single weave bead clads; 23 single weld clads were made on FD65 and NI2 PLUS, while 14 clads were made on NIFD PLUS and 8 clads on FD605. Figure 6.2 presents an image of claddings made on 42CrMo4 bars, then cut to make specimen for hammer mill test.

Next, the cladding was conducted on other selected base material in soft and heat-treated specimens required for the pulse jet test. After the cladding on quench and tempered steel

specimens, the specimens were cut in half by saw cutter. Water jet cutting was utilized for further separation of the cladding to obtain two 240mm long 0° samples, see Figure 6.3.

As described earlier each hardfacing alloy has its own unique characteristics, to study these characteristics claddings for cross sections were also prepared. Figure 6.4 presents cross sections of the four hardfacing alloys.

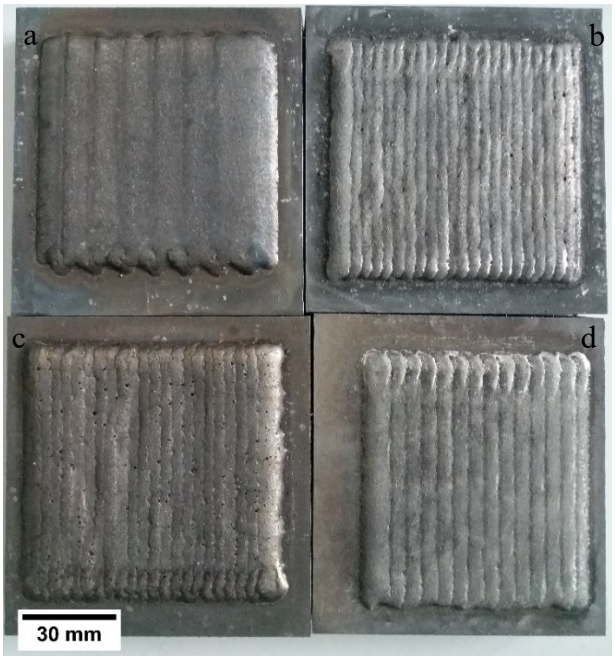

Figure 6.2: *Claddings of the four hardfacing alloys for hammer mill test, (a) FD605 (b) NI2 PLUS (c) FD65 (d) NIFD PLUS*

Figure 6.3: *(a) Cladded specimen from quench and tempered steel specimen (b) Sample obtained by cutting the cladded specimen in half by water jet cutting*

Figure 6.4: *Cross section clad images of the four selected alloys. From left to right, (1) Single weld weave bead of FD605, (2) five beads of FD65, (3) four beads of NIFD PLUS, (4) five beads of NI2 PLUS*

6.2.1 Calculation for cooling time ($T_{8/5}$)

The cooling time affects the microstructure of HAZ, as described in chapter 3. So, it is important to calculate the cooling time from 800-500˚C ($T_{8/5}$) to estimate the microstructure of HAZ. The cooling time can be calculated from the welding energy (E), heat input (Q) and pre-heating temperature (T_0). The formulas for calculation of $T_{8/5}$ are listed in equations 6.1, 6.2 and 6.3, while the values for E, Q and $T_{8/5}$ for each individual alloy is listed in Table 6.2. The details of these welding parameters can be found in reference [66] and [67].

$$\text{Welding Energy (E)} = 60 \times U \times I / 1000 \times V \tag{6.1}$$

$$\text{Heat Input (Q)} = E \times k \tag{6.2}$$

$$T_{8/5} = (6700 - 5 \times T_0) .Q. \{(1/ 500 - T_0) - (1/800\text{-}T_0)\}.F_3 \tag{6.3}$$

Where,

U= mean voltage (volts)

I = mean current (ampere)

V= travel speed (mm/min)

k= welding efficiency (for this case k=0.8)

F_3= three-dimension welding coefficient (for cladding F_3= 1)

Table 6.2: *Welding energy, heat input and cooling time values of the hardfacing alloys*

Alloys	E (KJ/mm)	Q (KJ/mm)	$T_{8/5}$ (sec)
NI2 PLUS	0.23	0.18	2.21
NIFD PLUS	0.24	0.19	2.28
FD65	0.25	0.20	2.40
FD605	0.84	0.67	7.96

6.3 Heat treatment and grinding

After preparation of the cladded specimens of all four hardfacing alloys on both selected base materials in soft and as clad states, the clads on both soft base materials were undergone **heat treatment**. The parameters selected were, heating to 850°-860°C, oil quenching then tempering at 450°C.

After the heat treatment of claddings on soft substrates, all the prepared specimens, in as clad and heat-treated, for hammer mill and pulse jet test were **grinded** for making smooth surface on the cladding. The grinding of specimens was done outside the university premises in a workshop specializing in grinding; it is a costly process. Figure 6.5 shows grinded hammer mill specimens.

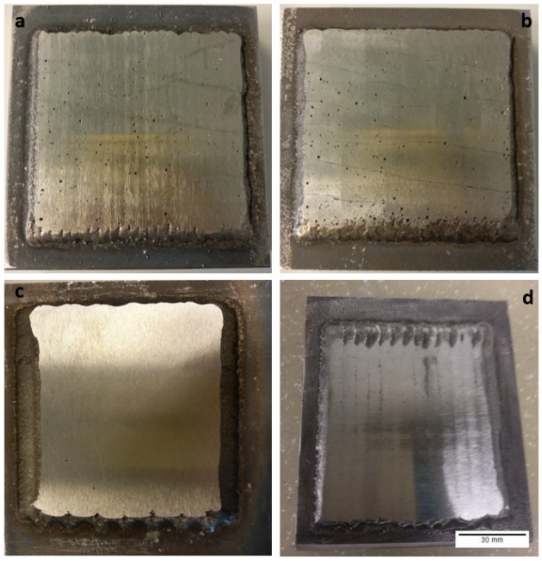

Figure 6.5: *Grinded hammer mill specimens (a) NI2 PLUS (b) FD65 (c) FD605 (d) NIFD PLUS*

7. RESULTS

This chapter includes the results acquired through the cladding of the selected alloys, in as clad and heat-treated states, by different analysis and measurements. The chapter also includes the outcome of the hammer mill impact wear test and pulse jet erosion wear test.

7.1 Cladding Results

The claddings of the hardfacing alloys were analyzed by different techniques. Cross sections were prepared for the four hardfacing alloys in as clad and heat-treated conditions; cross sections were appropriately cut, mounted as 50mm SEM buttons, grinded and polished. Grinding was completed by Struers Tegramin 30 with 200µm, 500µm and 1000µm SiC grinding papers respectively, while polishing was also done by Tegramin 30 with 3µm, 1µm and OP-U polishing cloths. The samples were then etched in 5% nital before analysis; etching in nital was done to reveal HAZ in the specimens. Figure 7.1 shows image of the grinded, polished and etched specimens of the four samples.

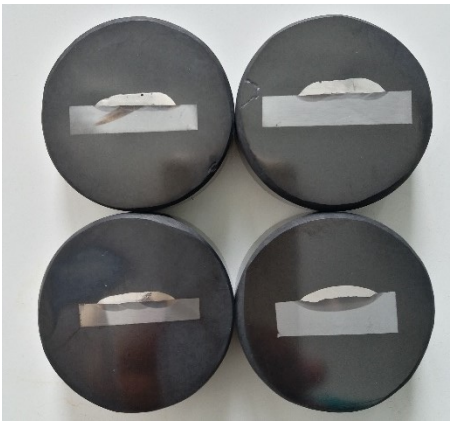

Figure 7.1: *Cross section specimen prepared as 50mm SEM buttons*

As described in chapter 2, dilution is one of the deciding factors when analyzing hardfacing deposits, dilution, deposition rate and net melting rate for as clad conditions are also presented in following sections for each alloy; heat treatment did not affect the dilution so, the dilution is same for as clad and heat-treated states. The dilution, deposition rate and net melting rate were calculated from image analysis by Image J; the details of the method of calculation can be found from reference [68]. The calculation of deposition rate and net melting rate required the density of each hardfacing alloy; the density was measured by Wallace density meter.

7.1.1 Cladding results of NI2 PLUS hardfacing alloy

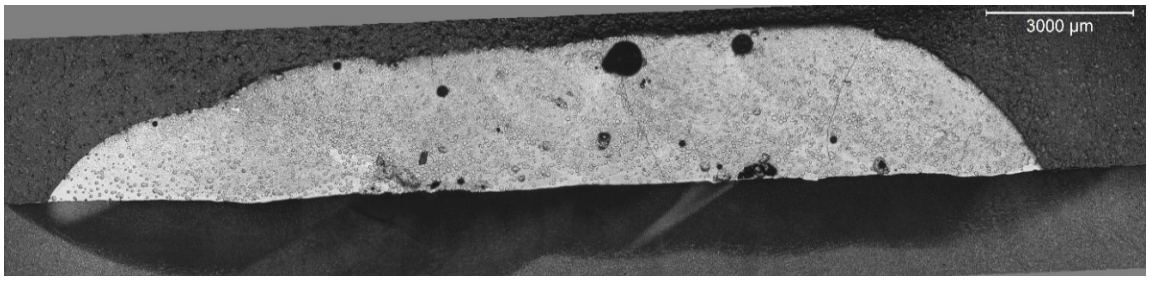

Figure 7.2: *Cross section image of as clad NI2 PLUS acquired at 2.5x*

Figure 7.2 presents a profile image of as clad NI2 PLUS cross section deposited on 42CrMo4 bar. The image shows small tungsten carbide particles spread throughout the coating with long vertical cracks and pores. The volume fraction of the tungsten carbides was analyzed by Image J and was found to be around 12%, while the average porosity levels revolved around 3%. The average size of tungsten carbides were found to be in the range of 30-35µm. The coating thickness, dilution, deposition rate and net melting rate are presented in Table 7.1.

The HAZ is quite visible and only affected a small percentage below the cladding; the average depth of HAZ below the clad is 1.4mm. Higher magnifications of the cladding were captured to analyze the cladding at a greater depth. Figure 7.3 presents images of the cladding taken with optical microscopy at 50x magnification. The Figure shows primary γ-Ni dendrites and nickel alloy matrix surrounded with tungsten carbides, the cladding also contains some secondary carbides that are difficult of characterize from optical microscopy.

While cladding NI2 PLUS by CMT, it was observed that lot of black colored powder was produced that surrounded the clad area, it was collected and planned to be analyzed later.

Table 7.1: *Calculated parameters of NI2 PLUS cladding by image analysis*

Average Coating thickness (mm)	**Density (gm/cm^3)**	**Dilution (%)**	**Deposition rate (kg/hr)**	**Net melting rate (kg/hr)**
2.91	9.1	2.2	3.112	3.19

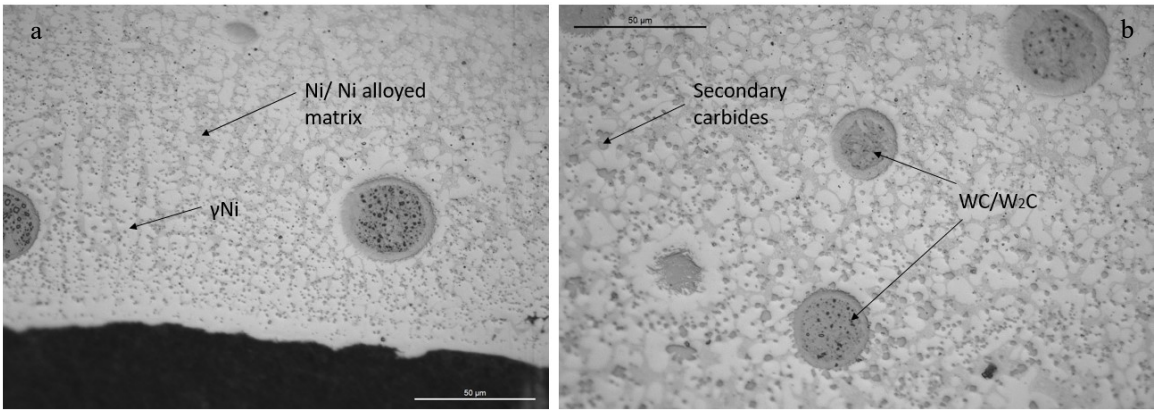

Figure 7.3: *50x magnification image of as clad NI2 PLUS (a) clad interface (b) main clad structure*

XRD analysis was conducted on the grinded as clad NI2 PLUS specimen to obtain accurate results that presents information about phase and elemental analysis. Figure 7.4 presents the results of XRD on NI2 PLUS in as clad state. XRD reveals that secondary carbides in Figure 7.3 are actually vanadium carbides and matrix consist of Ni_3B and Ni_2B. SEM images and EDS analysis were also conducted on the cross section specimens, SEM images and EDS analysis are presented in Figure 7.5 and table 7.2 respectively. The analysis confirm that the structure of NI2 PLUS consist of primary dendritic γ-Ni, nickel alloyed matrix, vanadium carbides and tungsten. The matrix mainly consists of nickel alloyed with carbon and tungsten; presence of boron in the matrix was confirmed by XRD, but EDS cannot detect boron because of its light weight.

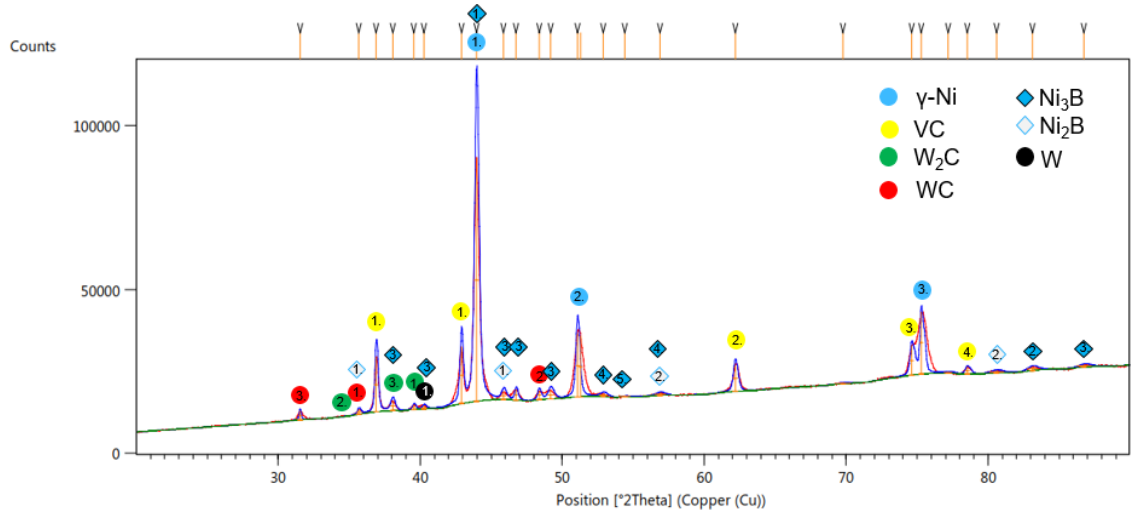

Figure 7.4: *XRD of NI2 PLUS hardfacing alloy in as clad state*

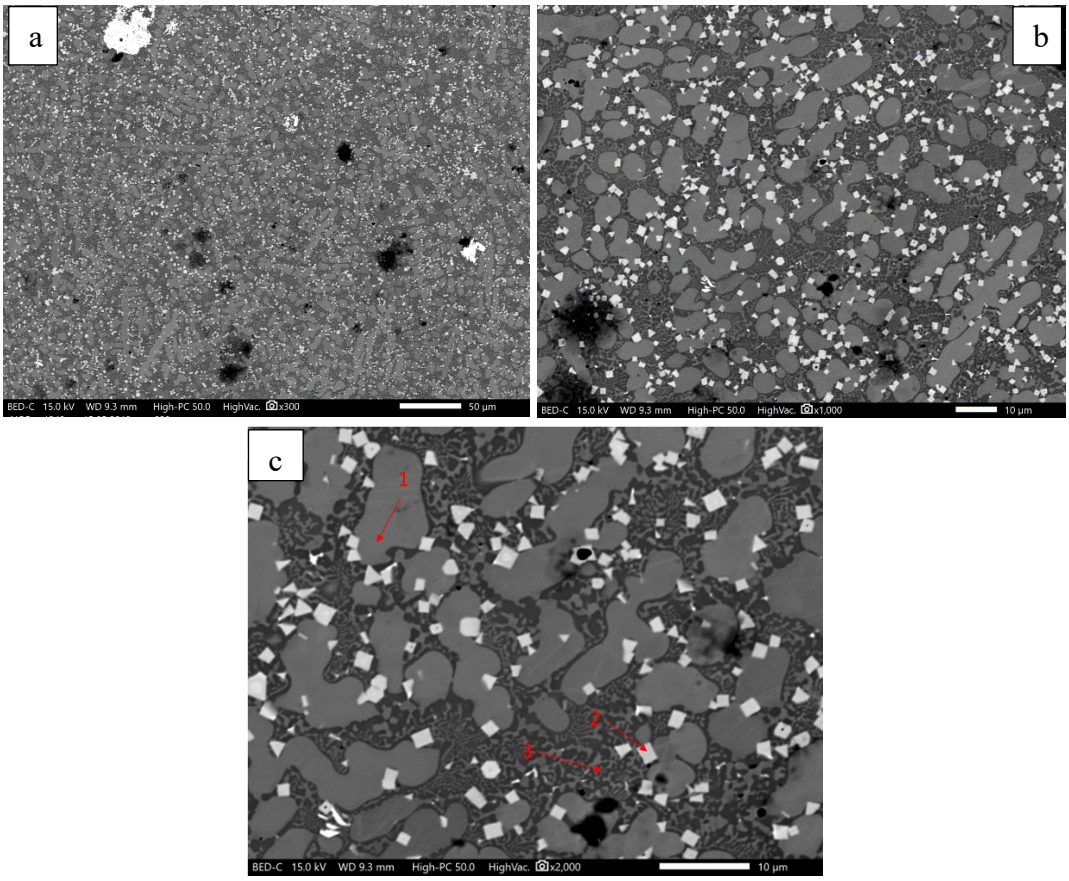

Figure 7.5: *SEM images of NI2 PLUS in as clad condition, (a) 300x (b) 1000x (c) 2000x with EDS analysis points*

Table 7.2: *EDS analysis of NI2 PLUS as clad*

Element (wt%)	C	Ni	V	W
Point 1	10.96	79.66	-	9.38
Point 2	8.48	90.30	-	1.22
Point 3	12.84	4.67	22.93	59.56

The clad on soft base materials were subjected to heat treatment, a cross section profile image of the heat-treated NI2 PLUS is presented in Figure 7.6. It can be seen that the heat treatment of the cladding produced cracks in the clad as well as in the base material. The crack is generated in the middle of the coating and extended to the base material. The HAZ region is no longer visible because of tempering of the specimen. The hardness of as clad and heat-treated NI2 PLUS was measured at a load of 1000g to characterize the variations in hardness before and after heat treatment; the hardness profile of as clad NI2 PLUS and heat-treated NI2 PLUS is presented in Figure 7.7. The hardness values that

exceeds 600HV are basically the hardness from the corners of the carbide, while the peak hardness of 2400HV corresponds the WC/W_2C hardness from the center of the carbide. Separate hardness was measured at a load of 300gm on five different points (for both matrix and tungsten carbides) and the average of the values was measured, the results are presented in Figure 7.8.

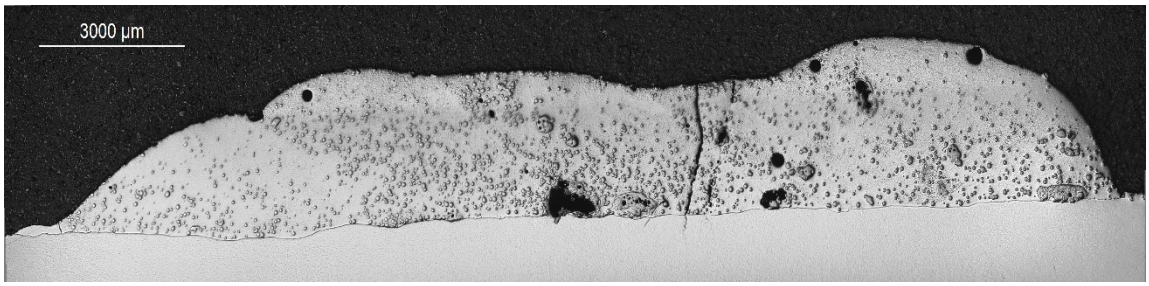

Figure 7.6: *Cross section image of heat-treated NI2 PLUS acquired at 2.5x*

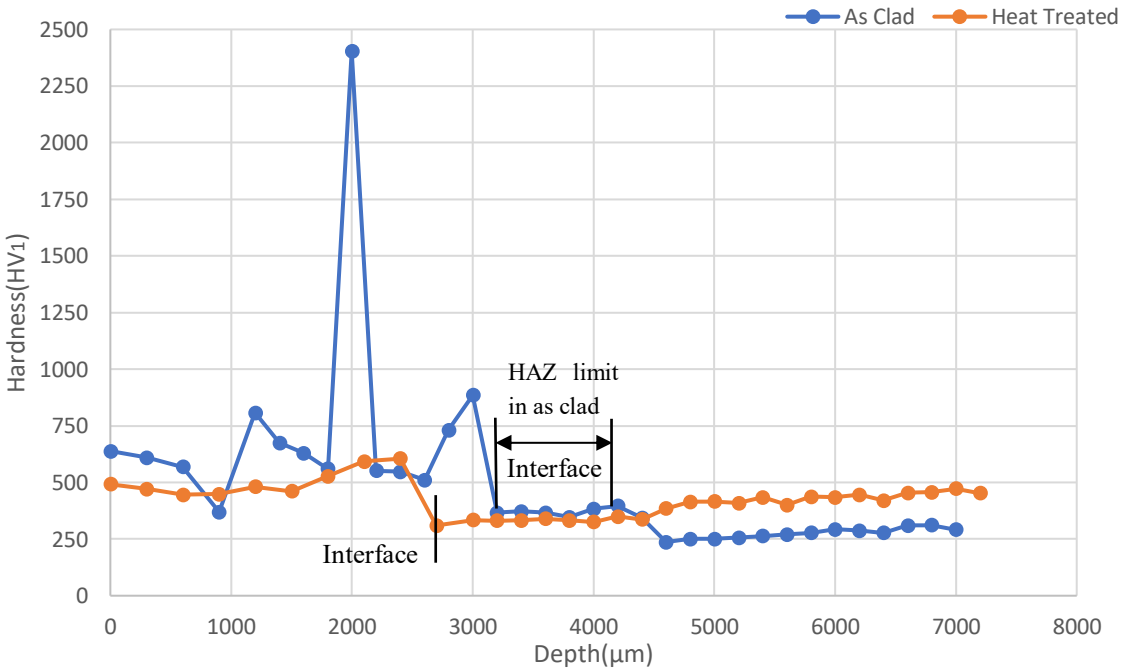

Figure 7.7: *Hardness (HV_1) profile of NI2 PLUS alloy in as clad and heat-treated condition*

For observing changes in the cladding after heat treatment, high magnification images were taken, Figure 7.9. From Figure 7.9, it is seen that no major changes occurred in the cladding and images of NI2 PLUS alloys in as clad and heat-treated condition resemble each other. XRD analysis of NI2 PLUS heat-treated is presented in Figure 7.10, the analysis by XRD also reveals that there are no phase changes occurred after heat treatment for this alloy. SEM images and EDS analysis were also carried out to observe post heat treatment affects; the results are presented in Figure 7.11 and Table 7.3. Interface of both

clad were also observed with SEM at a magnification of 300x, see Figure 7.12; cracks are clearly visible at interface in heat-treated image.

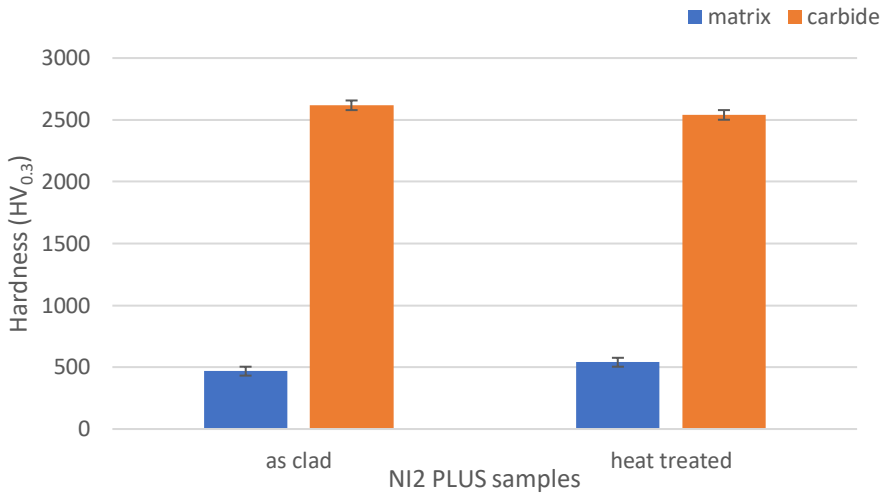

Figure 7.8: *Hardness of NI2 matrix and carbides in as clad and heat-treated conditions*

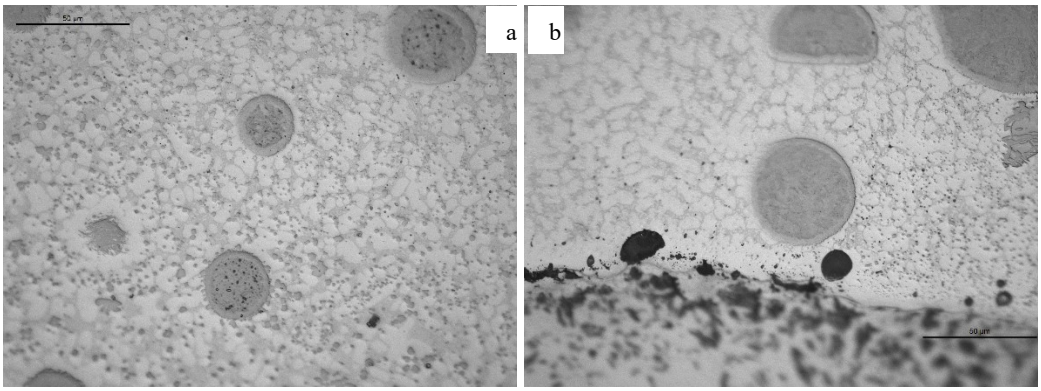

Figure 7.9: *High magnification (50x) images of NI2 PLUS in heat-treated condition, (a) basic clad structure (b) clad interface*

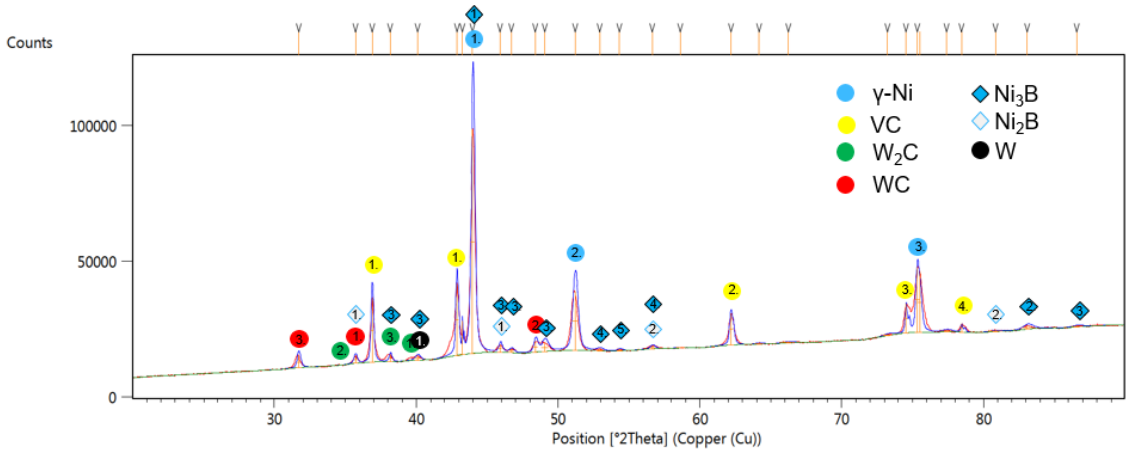

Figure 7.10: *XRD analysis of NI2 PLUS in heat-treated condition*

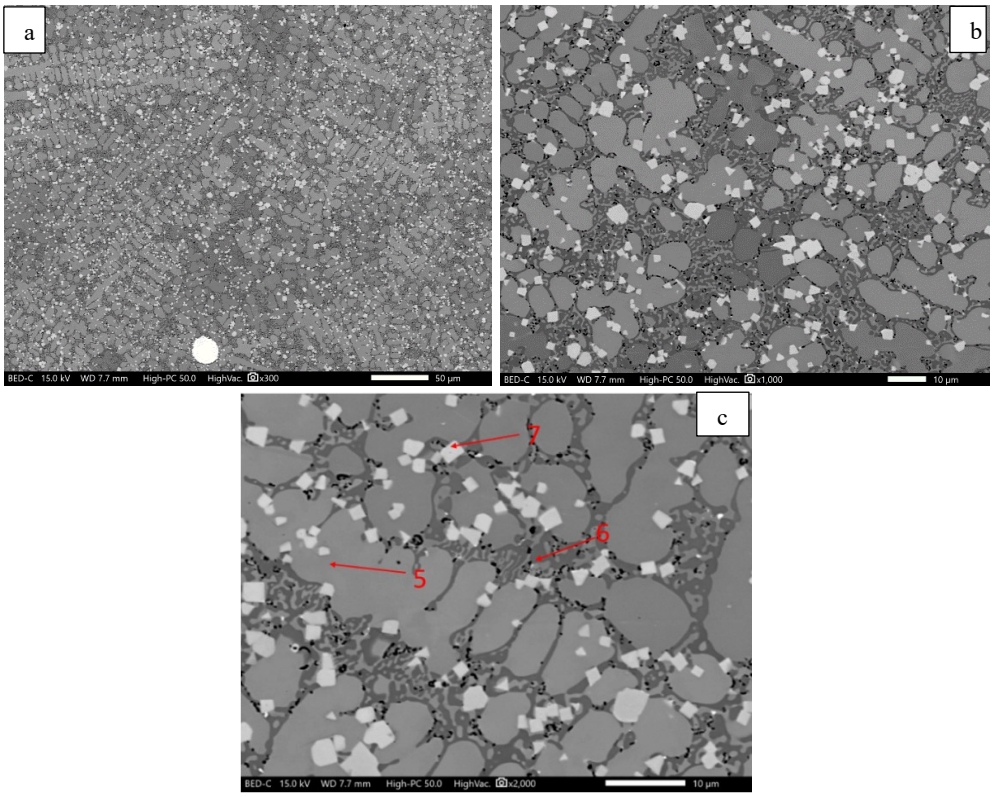

Figure 7.11: *SEM images of NI2 PLUS heat-treated (a) 300x (b) 1000x (c) 2000x with EDS points*

Table 7.3: *EDS analysis of NI2 PLUS heat-treated*

Element (wt%)	C	Ni	V	W	O
Point 5	9.90	80.31	-	9.78	-
Point 6	10.73	80.64	0.75	7.89	-
Point 7	13.35	5.13	23.24	56.67	1.42

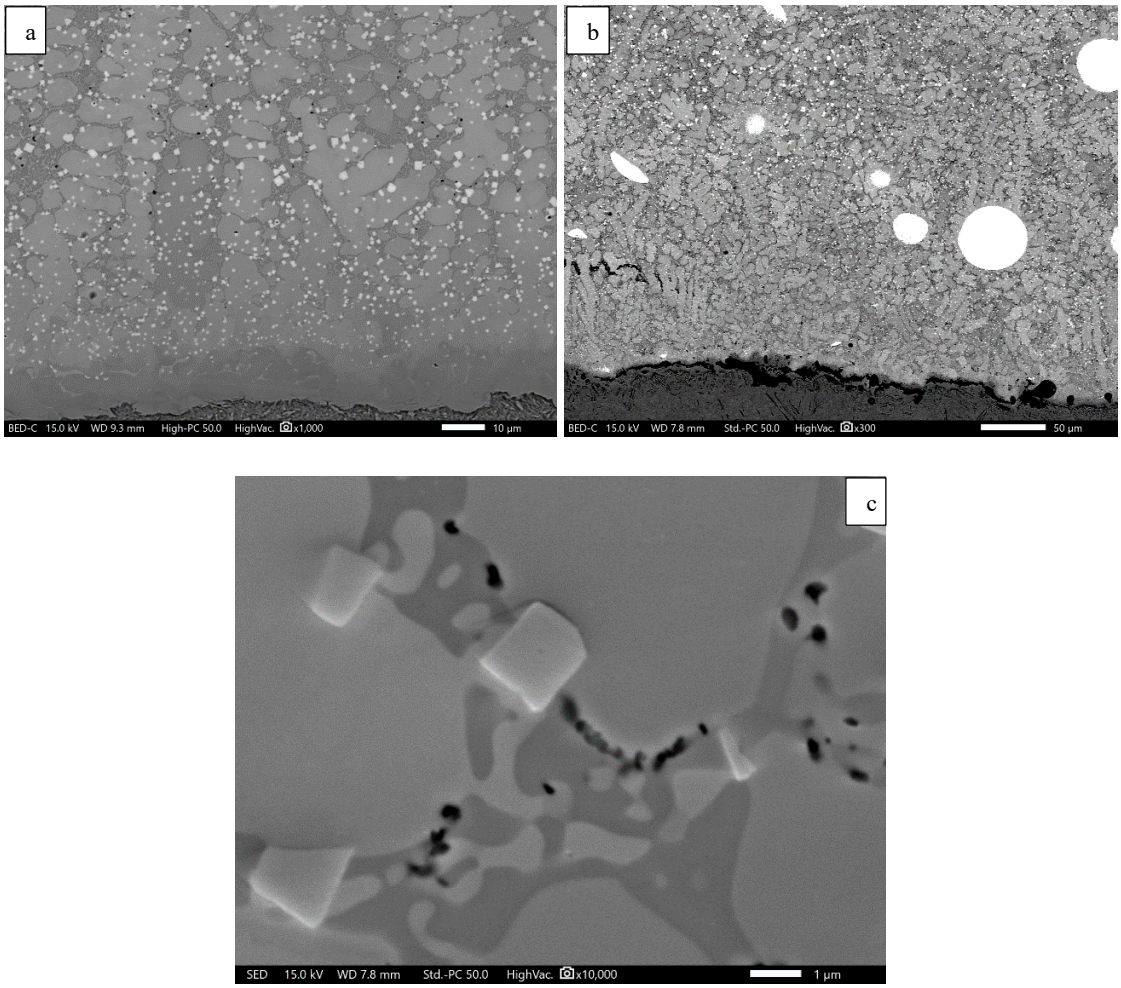

Figure 7.12: *Interface of NI2 hardfacing at 300x (a) as clad (b) heat-treated (c) Secondary electron image at 10,000x*

Figure 7.11 obtained at 2000x also shows some black holes throughout the coating, which seems like pores, to confirm that it is porosity secondary electron (SE) image was taken at high magnification, Figure 7.12c. SE image also indicates same black holes, which confirms that they are very tiny pores with in the coating.

7.1.2 Cladding results of FD65 hardfacing alloy

FD65 is a hypereutectic hardfacing alloys with large compositions of chromium, Figure 7.13 presents a clad profile image of FD65. There are long brittle cracks in the coating, these cracks are characteristic of this hardfaced coating and they are because of M_7C_3 carbides. Besides the cracks, the coating contains porosity that can be seen throughout the coating; the average porosity levels for FD65 is around 2%. Inconsistencies are also visible at the interface of the coating; they are bonding defects due to insufficient welding energy. The parameters related to this hardfaced deposit is presented in table 7.4. The coating is bit thicker than NI2 PLUS, while the HAZ region affected an area of 1.5mm below the clad.

Figure 7.13: *Clad profile of FD65 with 2.5x magnification*

Table 7.4: *Calculated parameters of FD65*

Average Coating thick-ness (mm)	Density (gm/cm^3)	Dilution (%)	Deposition rate (kg/hr)	Net melting rate (kg/hr)
3.45	7.6	3.4	3.28	3.31

Optical microscopy images were taken from the cross sections to observe the structure in an enhanced magnification, Figure 7.14. The images show the long columnar grains at the top of the coatings, while these columnar grains seem to be absent at the interface. Figure 7.15 shows SEM images of FD65 in as clad condition and table 7.5 presents the acquired EDS analysis. XRD results were also gathered to achieve phase analysis of the coating, Figure 7.16.

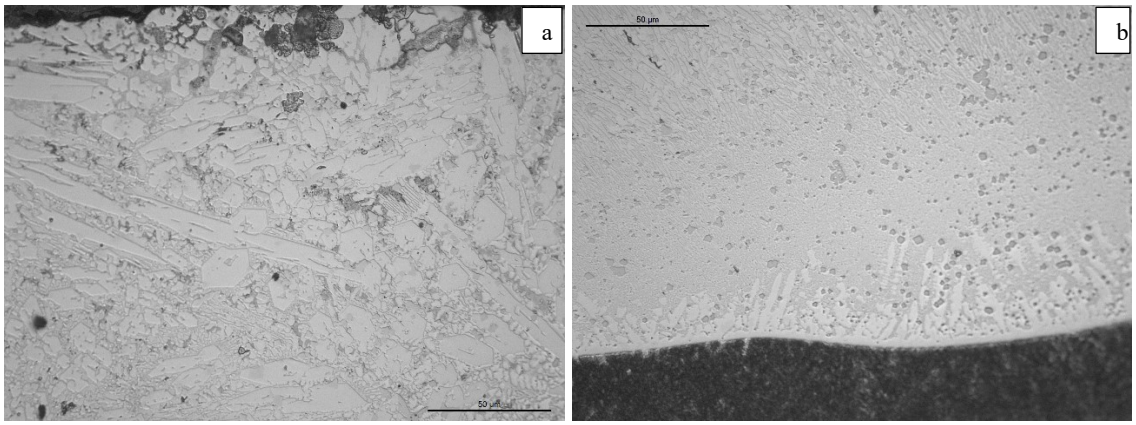

Figure 7.14: *50x images of FD65 in as clad state (a) top coat (b) interface*

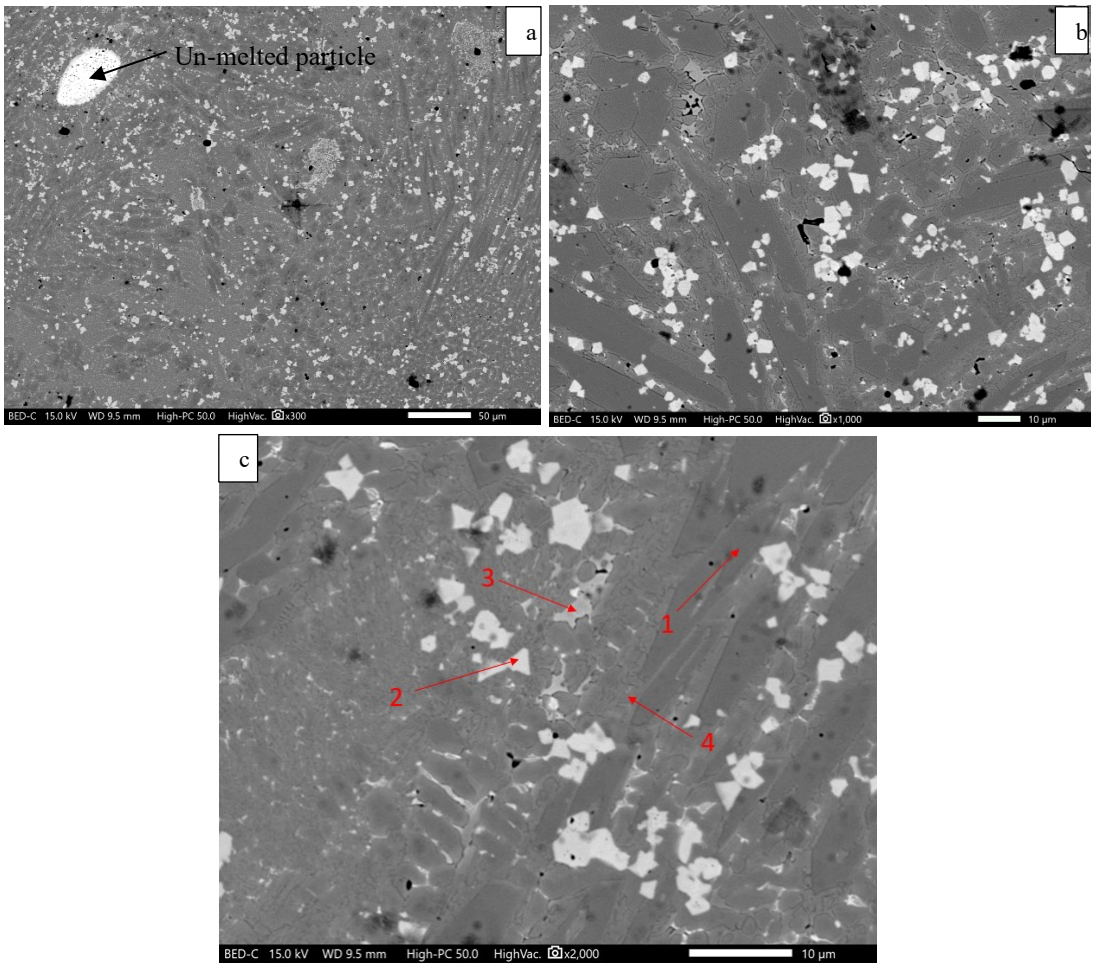

Figure 7.15: *SEM images of FD65 as clad (a) 300x (b) 1000x (c) 2000x with EDS analysis points*

Table 7.5: *EDS analysis of FD65 as clad*

Element (wt%)	Fe	C	Cr	Mo	Nb	W
Position 1	37.50	13.78	44.29	3.89	-	-
Position 2	2.28	17.20	2.59	-	76.20	
Position 3	52.09	11.64	9.03	20.13	-	4.89
Position 4	66.68	11.16	14.92	3.59	-	-

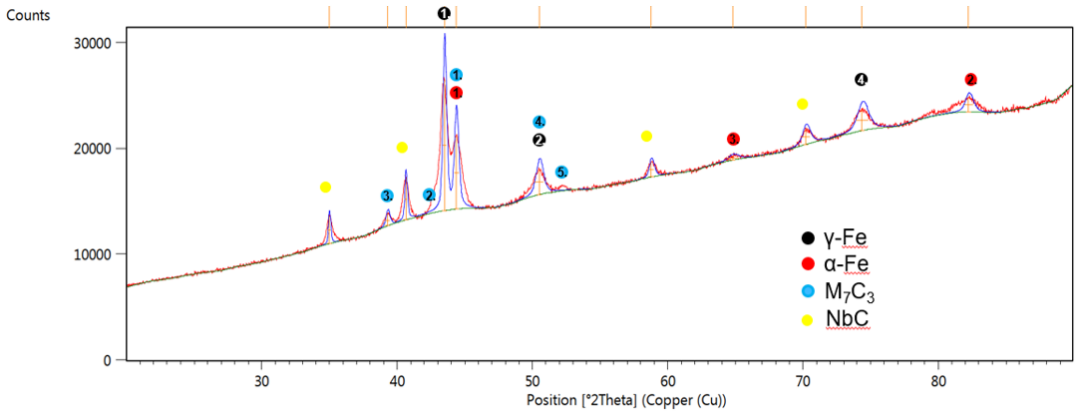

Figure 7.16: *XRD analysis of FD65 as clad*

The results from SEM, EDS, XRD and information from literature suggests that FD65 mainly consist of primary iron, chromium carbides of the form M_7C_3 in a eutectic matrix of austenite, ferrite and some carbides of the form $M_{23}C_6$ which contain molybdenum and tungsten. The cladding also contains niobium carbides and some un-melted particles; un-melted particles are often found in CMT welding because it is a low heat input process. The M_7C_3 carbides have a ledeburitic structure and optical microscopic images suggests that they are favorable at high cooling rates.

The FD65 clad on soft substrate was subjected to heat treatment, image of clad profile of heat-treated FD65 is presented in Figure 7.17. The cladding has additional cracks than as clad condition, which seems to be a result of heat treatment. Bonding defects at the interface is also again visible, that was also seen in as clad image. HAZ is not visible in the base metal because of the heat treatment. Cracking also did not occur in the base metal for this case, as compared to NI2 PLUS where cracks were seen in the base metal after heat treatment.

Hardness profile of heat-treated FD65 is presented in Figure 7.18, it is visible that there is a certain drop in hardness values. To study the structure in detail high magnification images were taken from the optical microscope, images from optical microscope are presented in Figure 7.19. From the Figures it seems that the carbides have broken from the top, but the middle structure and interface resemble the features of as clad condition.

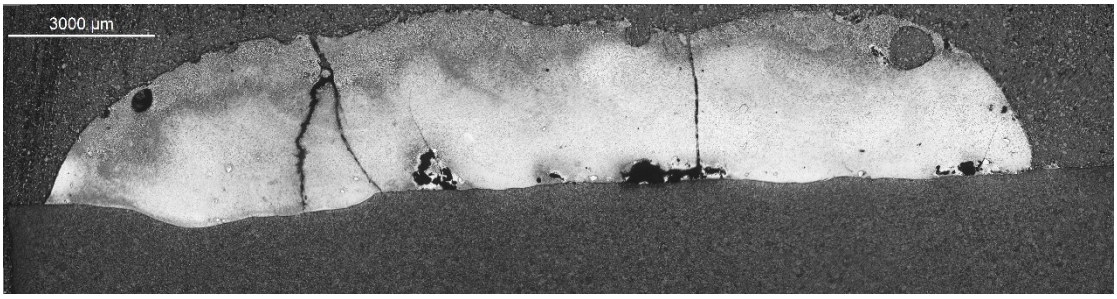

Figure 7.17: *Clad profile of FD65 after heat treatment*

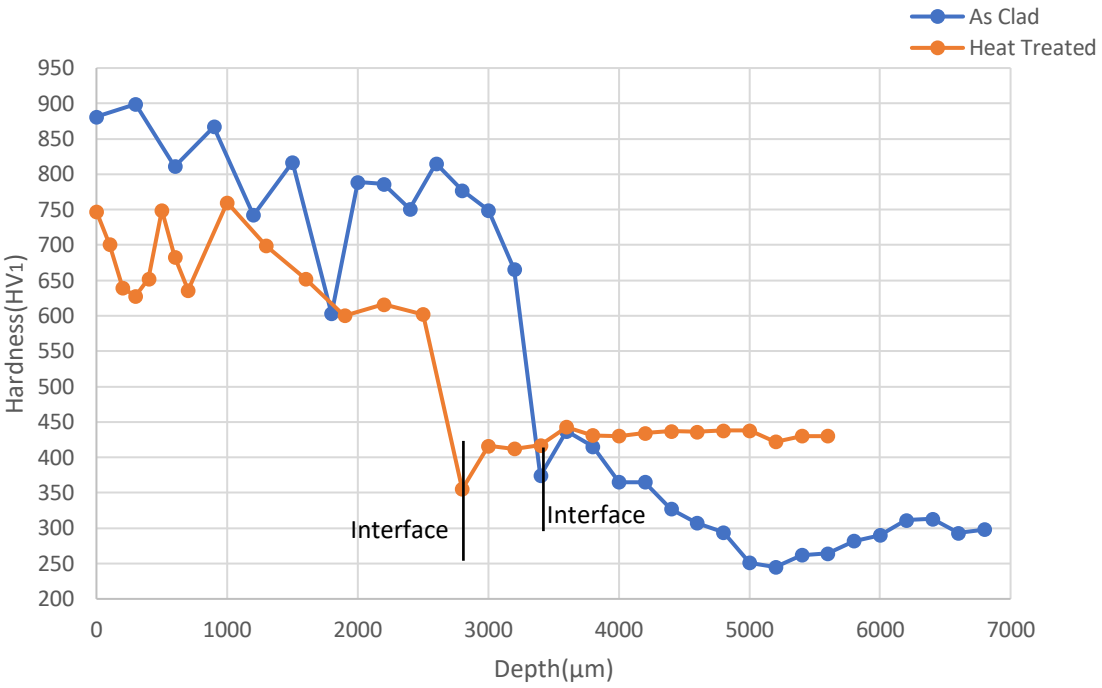

Figure 7.18: *Hardness profile of FD65 in as clad and heat-treated condition.*

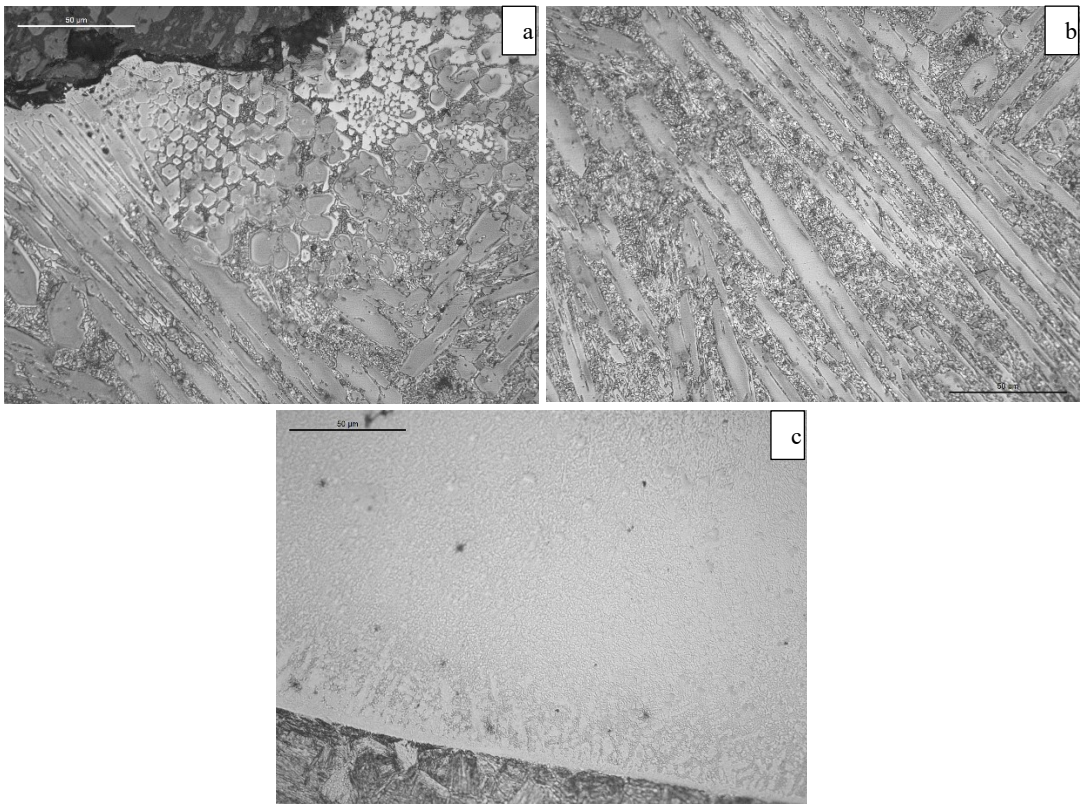

Figure 7.19: *50x images of FD65 heat-treated (a) top clad (b) middle of clad (c) interface*

Results of XRD of this clad are shown in Figure 7.20, XRD reveals that there is conversion of ferrite from austenite after heat treatment; this can be the reason for the drop in

hardness values. High magnification SEM images of heat-treated FD65 are presented in Figure 7.21, the specimen was also undergone EDS analysis, which are presented in table 7.6.

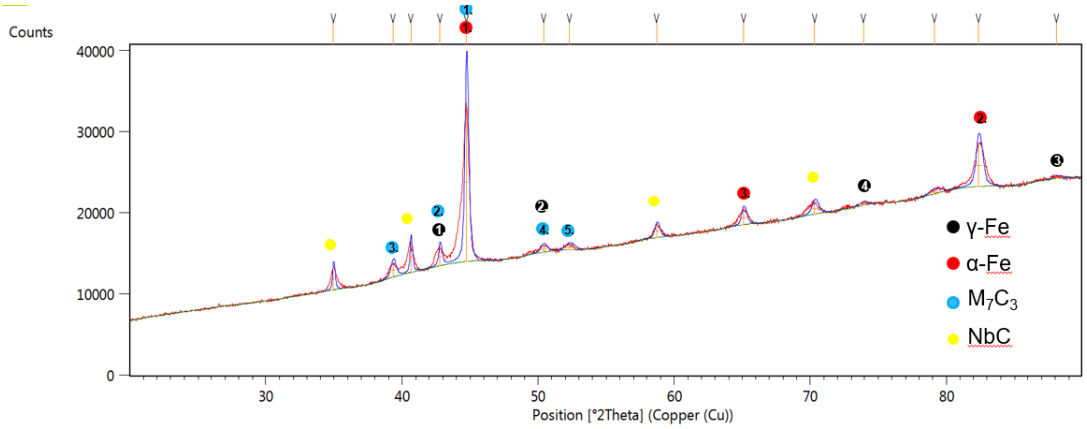

Figure 7.20: *XRD analysis of FD65 heat-treated*

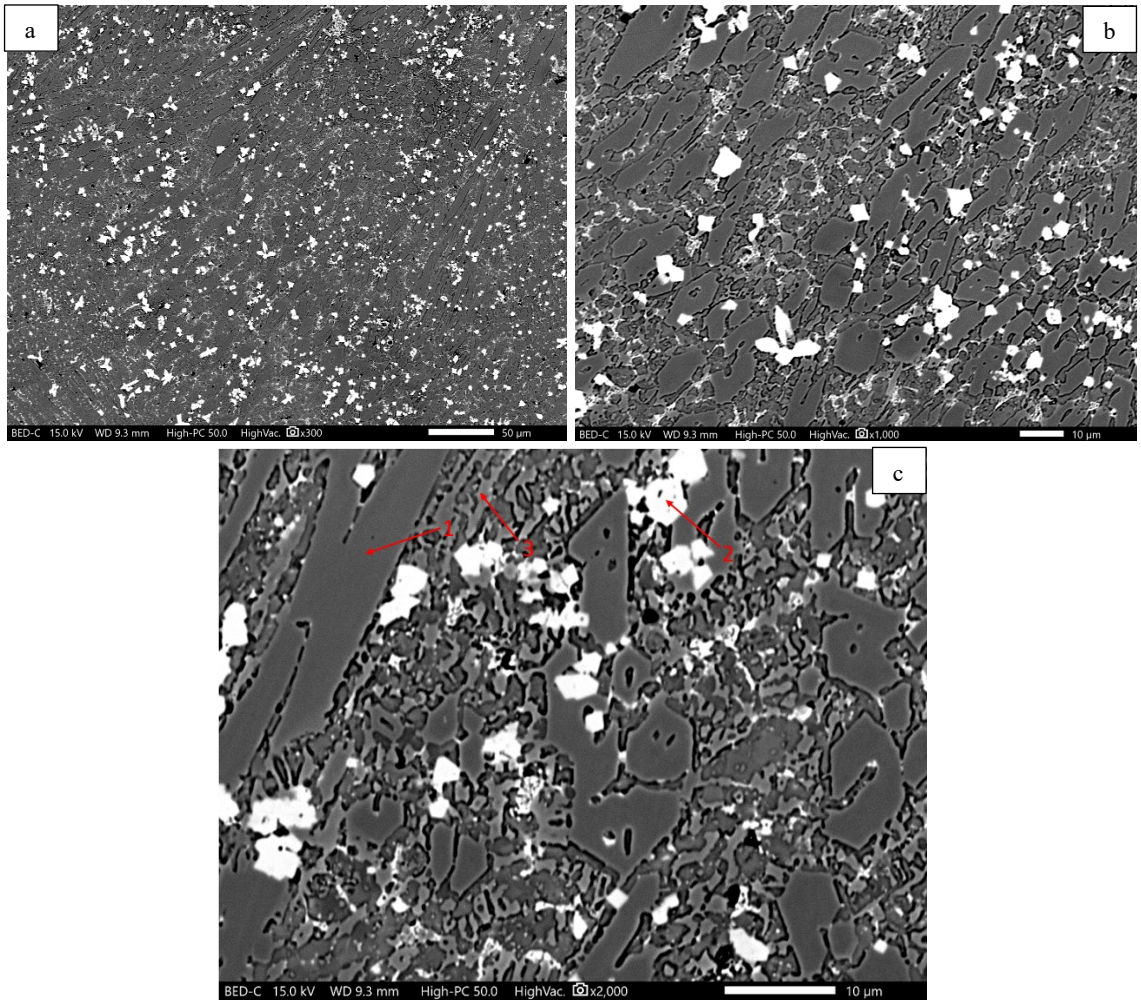

Figure 7.21: *SEM images of FD65 heat-treated (a) 300x (b) 1000x (c) 2000x with EDS analysis points.*

Table 7.6: *EDS analysis of heat-treated FD65*

Element (wt%)	Fe	C	Cr	Mo	Nb	Ti
Position 1	42.02	9.91	44.07	3.98	-	-
Position 2	2.59	2.76	-	-	93.54	1.11
Position 3	61.68	9.54	21.53	5.71	-	-

EDS analysis reveals that iron concentrations in the heat-treated condition have been increased to a certain degree as compared to as clad. Results of XRD, SEM and EDS analysis suggests that there is not much change in the structure rather than transformation of ferrite from austenite; the drop in hardness is due to this transformation. Images from optical microscopy shows that crack density in FD65 alloy increased after heat treatment, these cracks progressed throughout the length of the coating and seemed to break the coating; this can be inferior to the wear resistance of the alloy.

7.1.3 Cladding results of FD605 hardfacing alloy

As described in section 5.2.2 FD605 is low carbon hardfacing alloy containing small amounts of chromium and molybdenum along with some special carbides. Figure 7.22 presents an image of FD605 clad, the clad is free of cracks and porosity with a smooth interface. The calculated parameters for FD605 are given in table 7.7; the dilution of FD605 is higher as compared to the previous cladding, but it is only seen at the ends of a wide single bead. The reason for high dilution is the weaving mode selected; CMT torch turns the direction at the end and speed almost stops instantaneously, which results in high dilution. The average depth of HAZ measured from the middle of the cladding is 3.2mm; which is also large as compared to previous claddings; high depth of HAZ is due to the high heat input for this hardfacing.

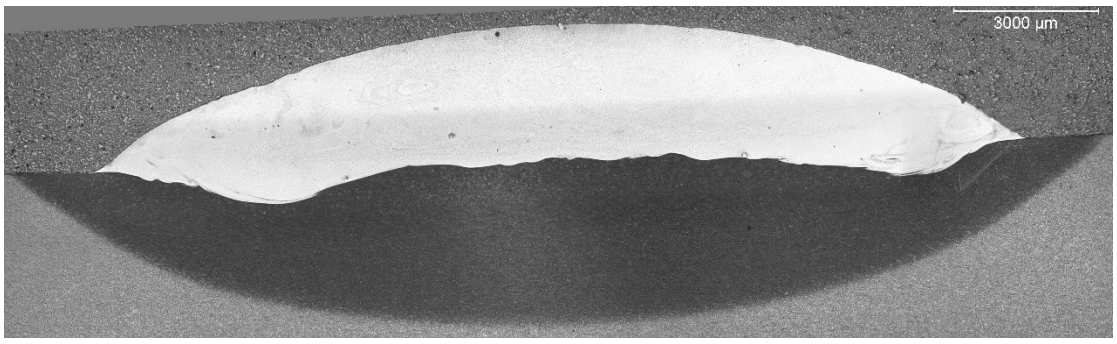

Figure 7.22: *Clad profile of FD605 in as clad condition*

Table 7.7: *Calculated parameters of FD605*

Average Coating thick-ness (mm)	Density (gm/cm^3)	Dilution (%)	Deposition rate (kg/hr)	Net melting rate (kg/hr)
3.65	7.4	11.2	3.07	3.39

For observing microstructure of the cladding higher magnification images were taken from the optical microscope, Figure 7.23. From Figure 7.23, it can be seen that the structure is not complex and basically consist of a matrix and well dispersed carbides. XRD analysis was conducted to study the phases in this alloy, Figure 7.24. The SEM images and EDS results are presented in Figure 7.25 and table 7.8 respectively.

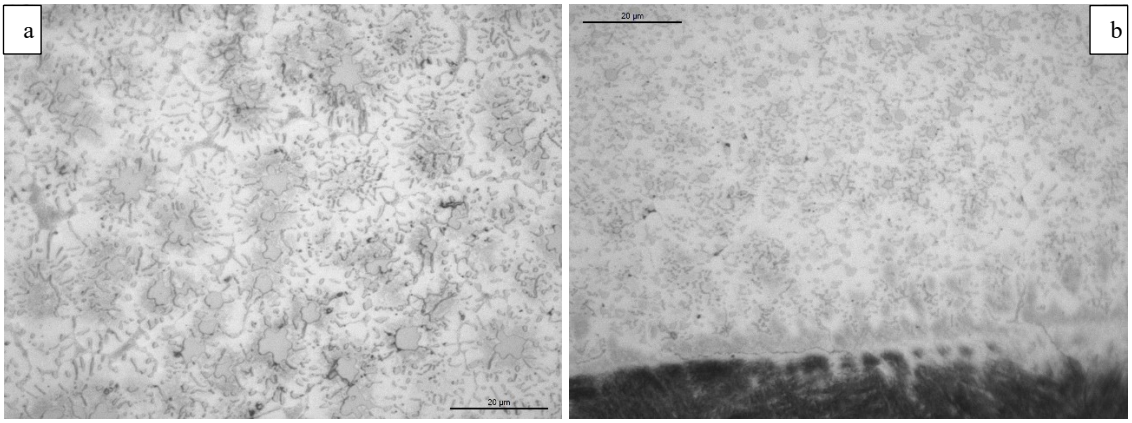

Figure 7.23: *100x images of FD605 as clad (a) main coat (b) interface*

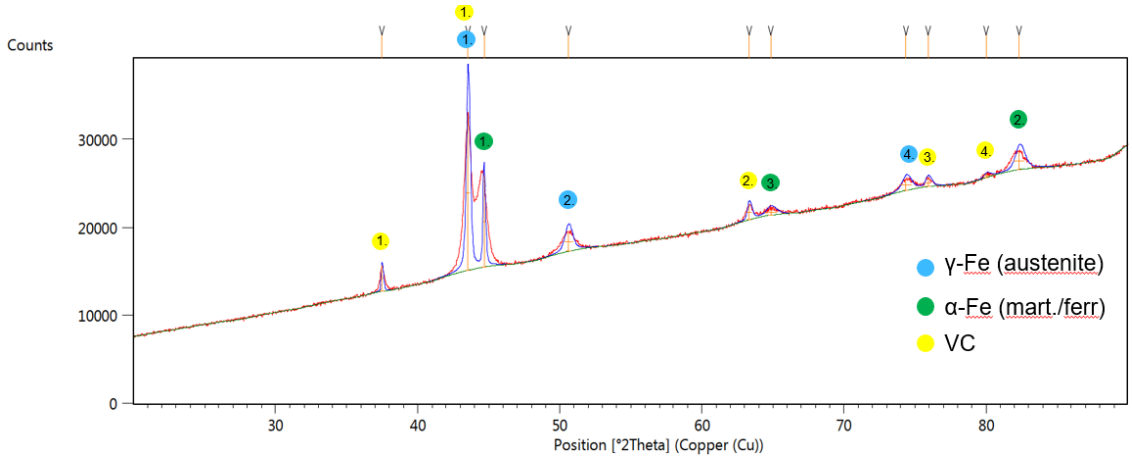

Figure 7.24: *XRD analysis of FD605 as clad*

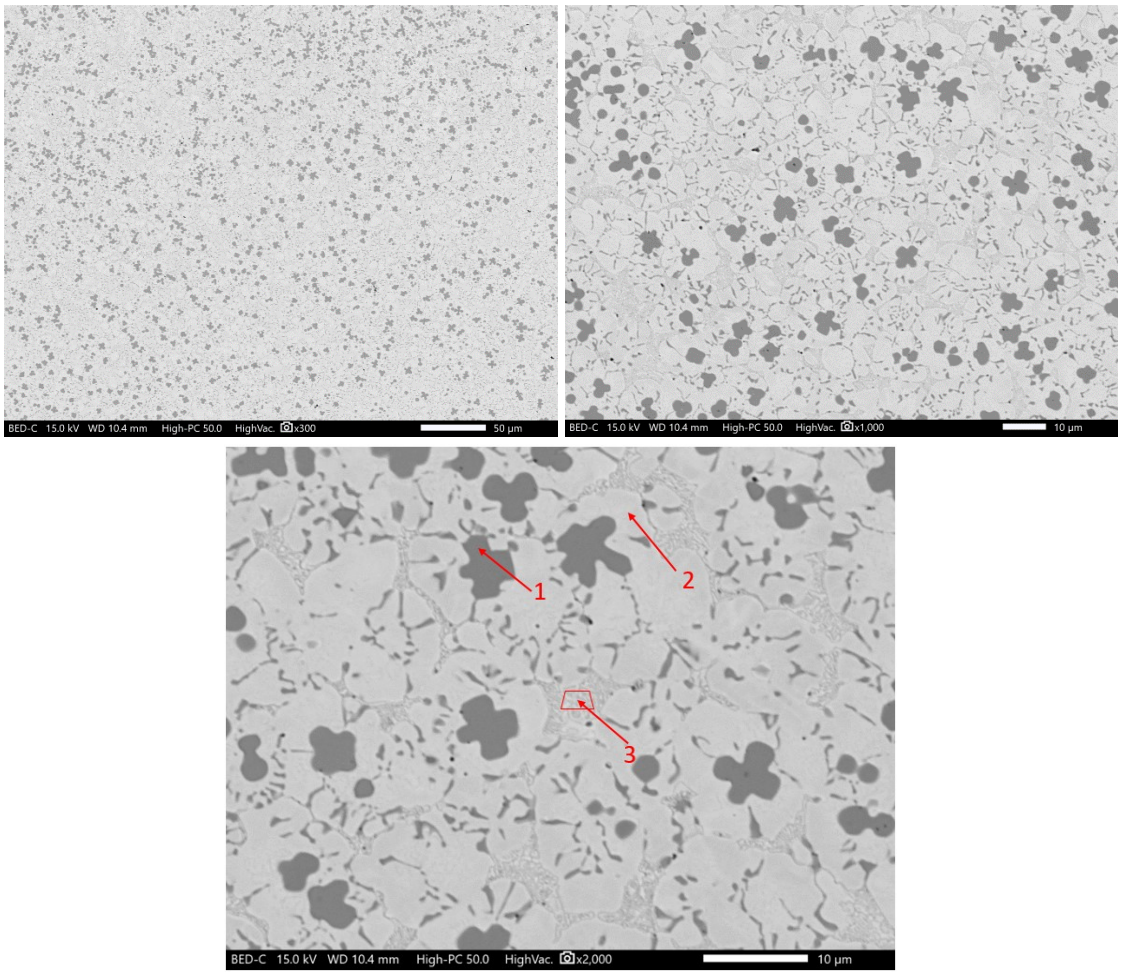

Figure 7.25: *SEM images of FD605 in as clad condition (a) 300x (b) 1000x (c) 2000x with EDS analysis points*

Table 7.8: *EDS analysis of FD605 as clad*

Element (wt%)	Fe	C	Cr	Mo	Si	V
Position 1	2.96	18.22	3.07	-	-	75.16
Position 2	83.32	7.43	4.32	-	1.20	3.10
Polygon 3	71.58	6.58	12.08	3.39	0.82	4.41

The results from XRD, EDS and SEM reveals that the matrix consist of ferritic/austenitic structure with small sized precipitated carbides. The special carbides mentioned in section 5.2.2 are vanadium carbides, which are present in varying sizes; correct estimation of size and volume fraction of vanadium carbides is difficult because they get interconnected to each other.

Analysis of Heat Affected Zone (HAZ) is necessary to estimate the hardness variations from the base metal and levels of stresses. Figure 7.26 presents images acquired from the HAZ of FD605. According to the theory presented in section 3.3, Figure 7.26a relates to coarse grain zone that has a high hardness due to dissolved carbides, 7.26b is an image of fine grain zone, 7.26c of the inter-critical zone and 7.26d is an image of the base metal. Hardness profile of HAZ in FD605 are given in Figure 7.28, it can be seen that HAZ of FD605 has a high hardness to a greater depth as compared to FD65 and NI2 PLUS.

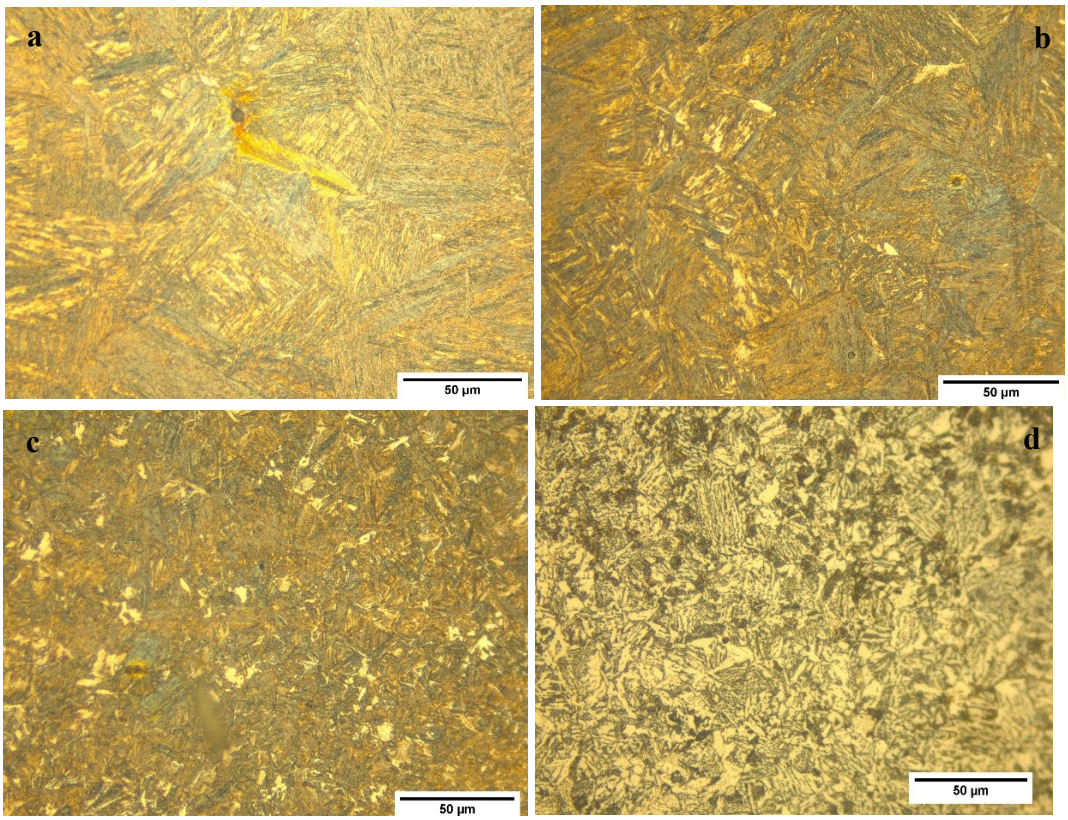

Figure 7.26: *HAZ images of FD605 (a) coarse grain zone (b) fine grain zone (c) Inter-critical zone (d) base metal*

As all the claddings had to be subjected to heat treatment, FD605 cladded on soft base metal was also undergone heat treatment, Figure 7.27 presents an image of clad profile of FD605 in heat-treated condition. Clad profile in the heat-treated condition is similar to the as clad state and no cracks or inconsistencies are visible after heat treatment. Hardness profile at a load of 1000kg was conducted to measure the variations in hardness, Figure 7.28. Hardness of FD605 dropped to around 500HV from 800HV after heat treatment, so heat treatment has a considerable effect on the hardness of FD605. For analyzing phase changes after heat treatment XRD analysis was conducted, Figure 7.29.

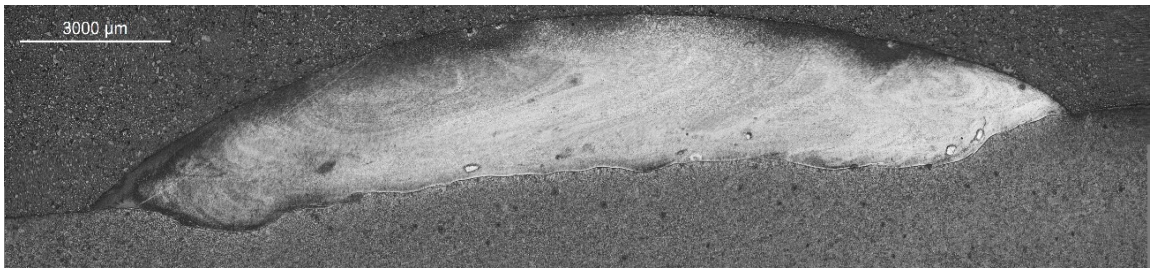

Figure 7.27: *Clad profile of FD605 heat-treated.*

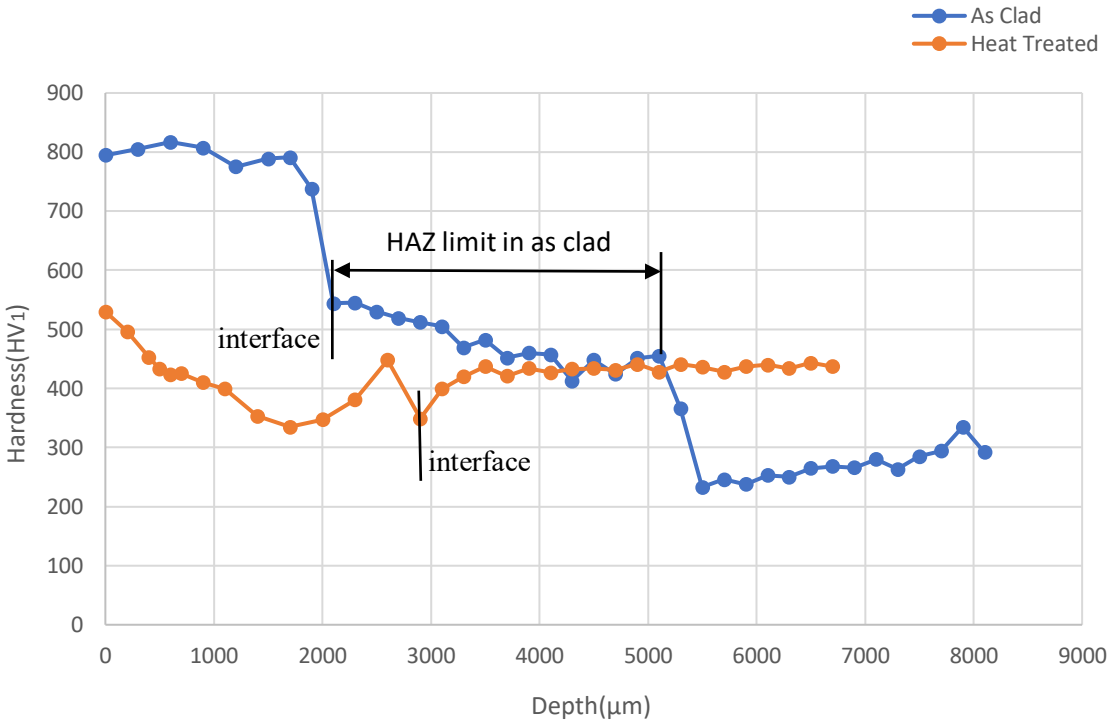

Figure 7.28: *Hardness profile of FD605 in as clad and heat-treated conditions.*

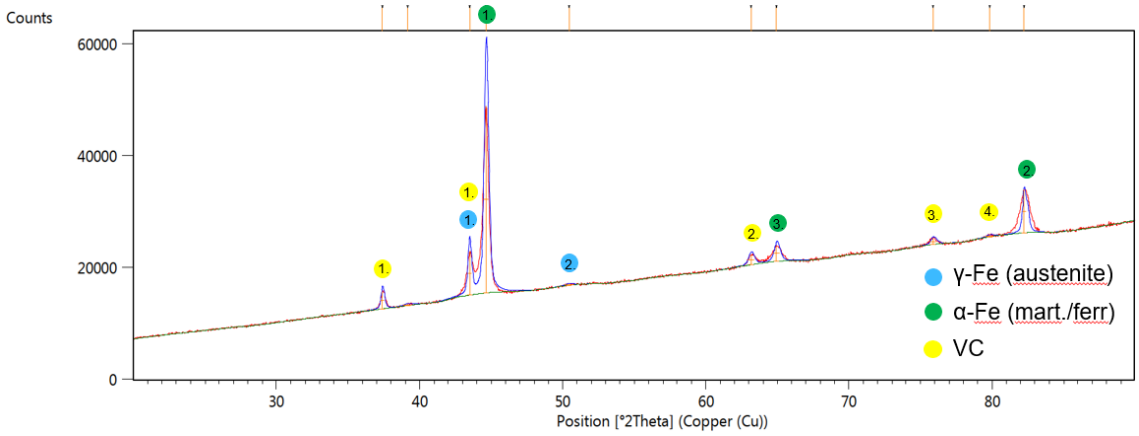

Figure 7.29: *XRD analysis of FD605 heat-treated*

XRD analysis only shows the transformation of ferrite from austenite in the matrix, otherwise the results from XRD is similar to as clad. SEM images and EDS analysis were conducted to acquire a detail study of the changes in heat-treated state, Figure 7.30 presents the SEM images and table 7.9 presents the EDS analysis.

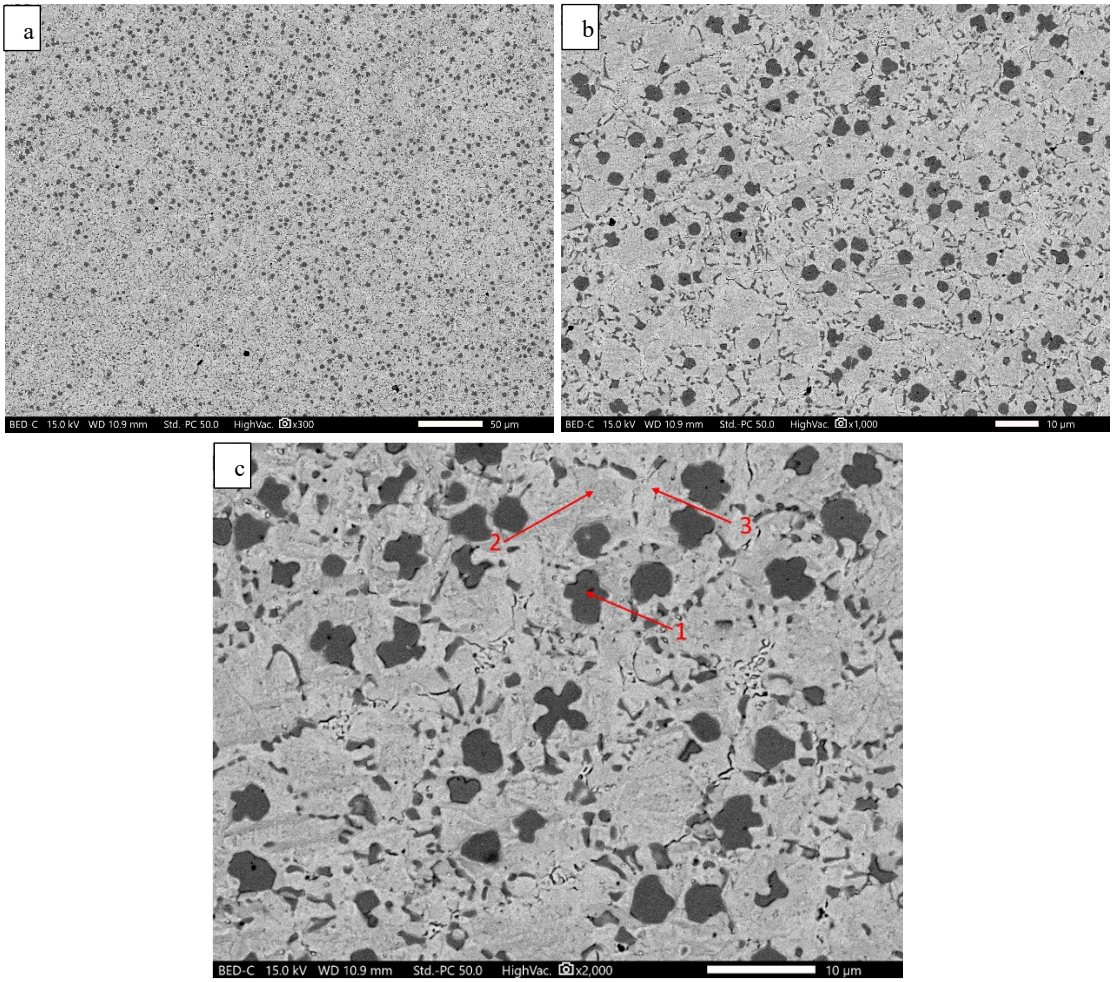

Figure 7.30: *SEM images of FD605 heat-treated (a) 300x (b) 1000x (c) 2000x with EDS analysis points*

Table 7.9: *EDS analysis of FD605 heat-treated*

Element (wt%)	Fe	C	Cr	Mo	Si	V
Position 1	2.49	29.63	-	1.49	-	65.30
Position 2	69.01	20.45	3.87	-	0.97	4.98
Position 3	67.10	21.38	8.86	-	0.65	2.02

SEM images show that the precipitated carbide region is not longer visible in the heat-treated sample, so it is possible that precipitated carbides have undergone dissolution after heat treatment. The vanadium carbides did not went through any changes and the composition is also similar to as clad, according to the analysis by EDS.

FD605 is a low carbon alloy and according to literature it has the tendency to work harden under stress; determining the depth of work hardening layer is important as it influences the wear resistance of the alloy. As mentioned earlier, all the hardfacing samples were grinded before testing, so a small specimen of the grinded FD605 (as clad) was mounted on the 30mm SEM button to study the depth of work hardened layer. Figure 7.31 presents the clad profile of FD605 cut from the grinded specimen; hardness values were taken from the very top at a load of 100g. Three positions were selected for plotting the hardness profile, the indents were separated at a distance of 50µm, Figure 7.32 presents the graphical representation of the average hardness profile. From Figure 7.32, it can be seen that the grinded FD605 undergoes work hardening, and estimated hardness depth of the work hardening layer after grinding is around 200µm.

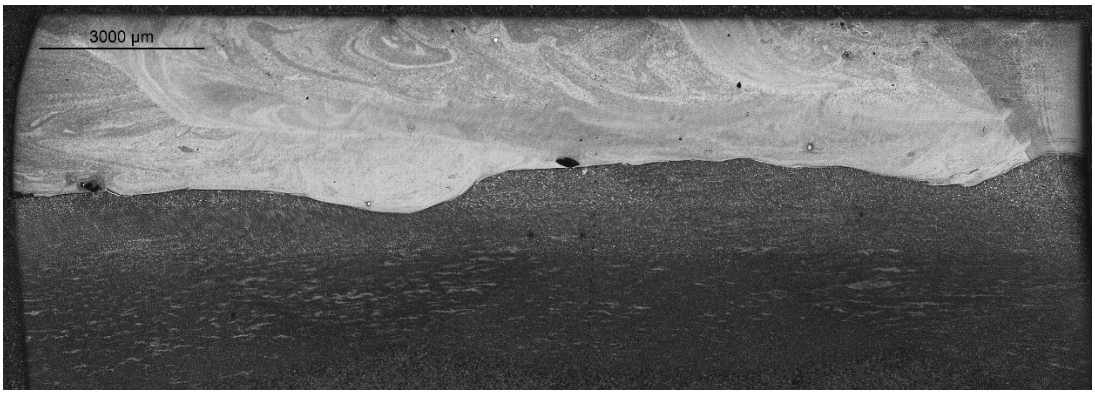

Figure 7.31: *Clad profile of grinded FD605 on 30mm SEM button*

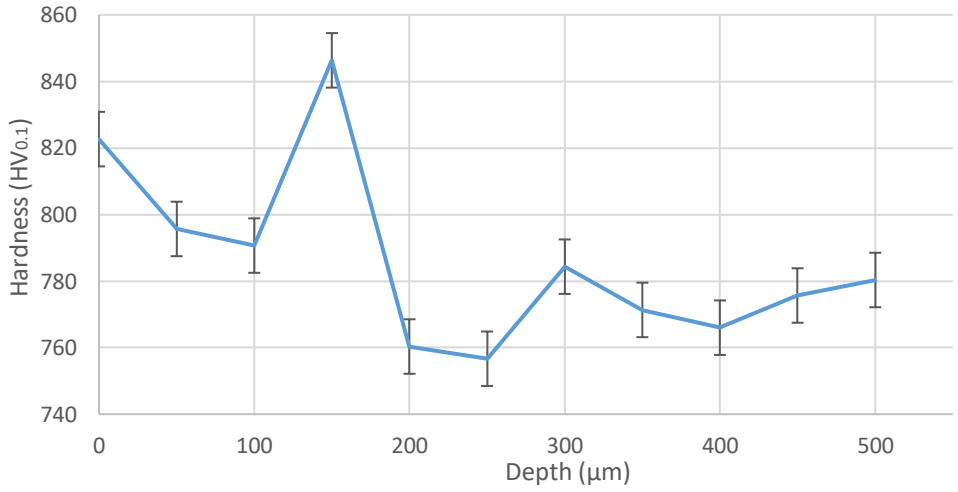

Figure 7.32: *Hardness profile of grinded FD605*

7.1.4 Cladding results of NIFD PLUS hardfacing alloy

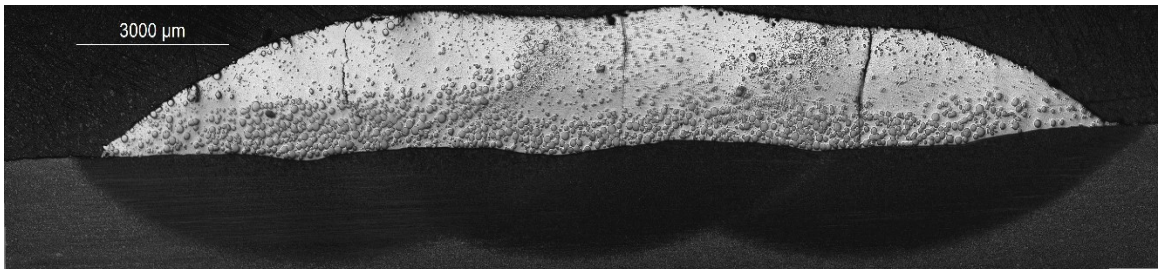

Figure 7.33: *Clad profile of NIFD PLUS as clad at a magnification of 2.5x*

NIFD PLUS is the fourth selected hardfacing alloy, Figure 7.33 presents an image of the clad profile of NIFD PLUS at a magnification of 2.5x. Table 7.10 presents the calculated parameters of the image analysis of NIFD PLUS; coating of NIFD PLUS has the least thickness as compared to other hardfacing alloys. The dilution values are also low, and the average depth of heat affected zone is 1.8mm below the interface. Volume fraction of the primary tungsten carbides is 22%, but it is due to the higher size of carbides; the porosity levels were negligible in NIFD PLUS. A few cracks are also seen in Figure 81, these seem to be present in the coating appearing from the surface; these cracks are more prominent than encountered with NI2 PLUS.

The image shows tungsten carbide particles spread in the coating; large population of carbides are near the bottom of the coating. The carbides are larger in size as compared to the NI2 PLUS because of the larger wire diameter; the average size of carbide in NIFD PLUS was found to be around 60µm, Figure 7.34 shows the WC/W_2C size distribution in NI2 PLUS and NIFD PLUS for twenty carbides. The carbides seem that they are flowing from left to right in the coating; reason is overlapping of the beads.

Table 7.10: *Calculated parameters of NIFD PLUS*

Average Coating thick-ness (mm)	**Density (gm/cm^3)**	**Dilution (%)**	**Deposition rate (kg/hr)**	**Net melting rate (kg/hr)**
2.3	9.6	4.6	2.81	3.01

Figure 7.35 shows the optical microscopy images of NIFD PLUS in as clad condition, the carbides primary carbides are spherical, while the secondary carbides are irregular and blocky; the secondary tungsten carbides precipitated from the melt due to dissolved primary tungsten carbides. The clad microstructure resembles the structure of NI2 PLUS; the matrix consists of primary dendrites and secondary nickel alloyed matrix, however

there is absence of vanadium carbides. Porosity is much more visible at high magnification and image analysis shows that the average porosity levels are in the range of 2-3%.

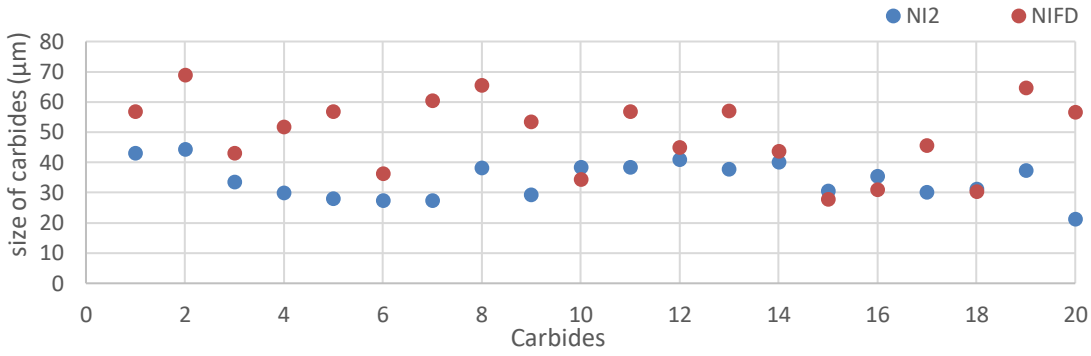

Figure 7.34: *Comparison of carbide size between NI2 PLUS and NIFD PLUS*

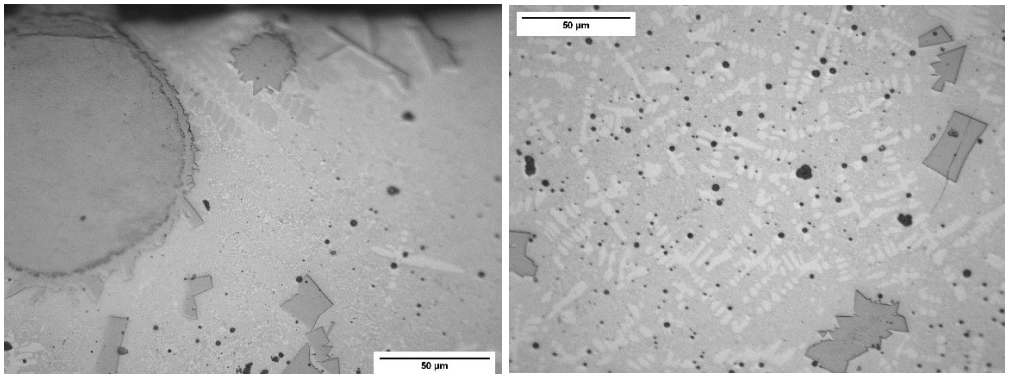

Figure 7.35: *Features of NIFD PLUS as clad at 50x magnification*

XRD analysis of NIFD PLUS in as clad condition is presented in Figure 7.36, the analysis shows a high number of phases present. High number of phases indicate a high degree of dissolution of the alloy, also the presence of elemental tungsten and blocky secondary tungsten carbides gives an idea that there is a certain degree of dissolution. Vanadium carbides are not present as encountered with NI2 PLUS.

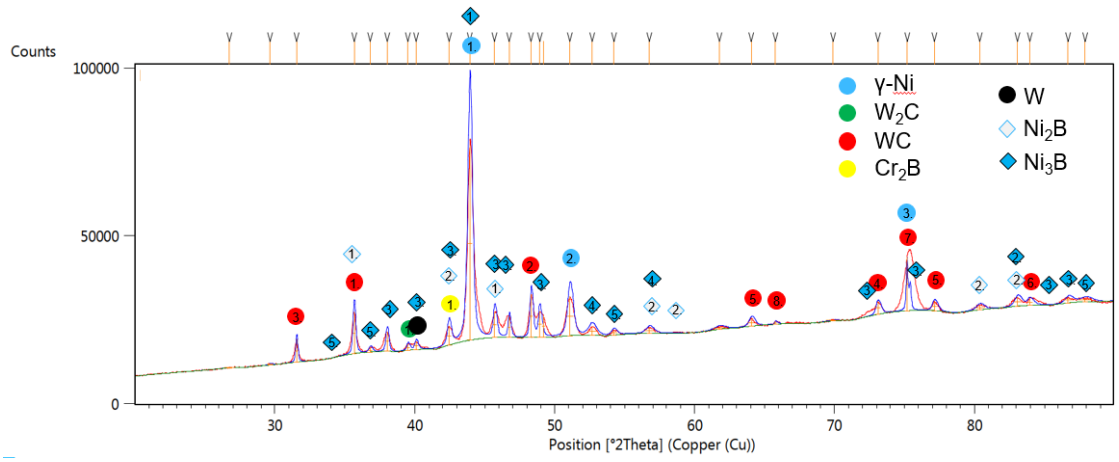

Figure 7.36: *XRD analysis of NIFD PLUS as clad*

SEM images and EDS analysis were also conducted for NIFD PLUS, SEM images are presented in Figure 7.37 and EDS analysis in table 7.11. Phases containing boron are not detected by EDS, so not quite good results were gathered by EDS. Carbon and iron were found in all phases; presence of carbon may be a result of diffusion out of the WC/W_2C.

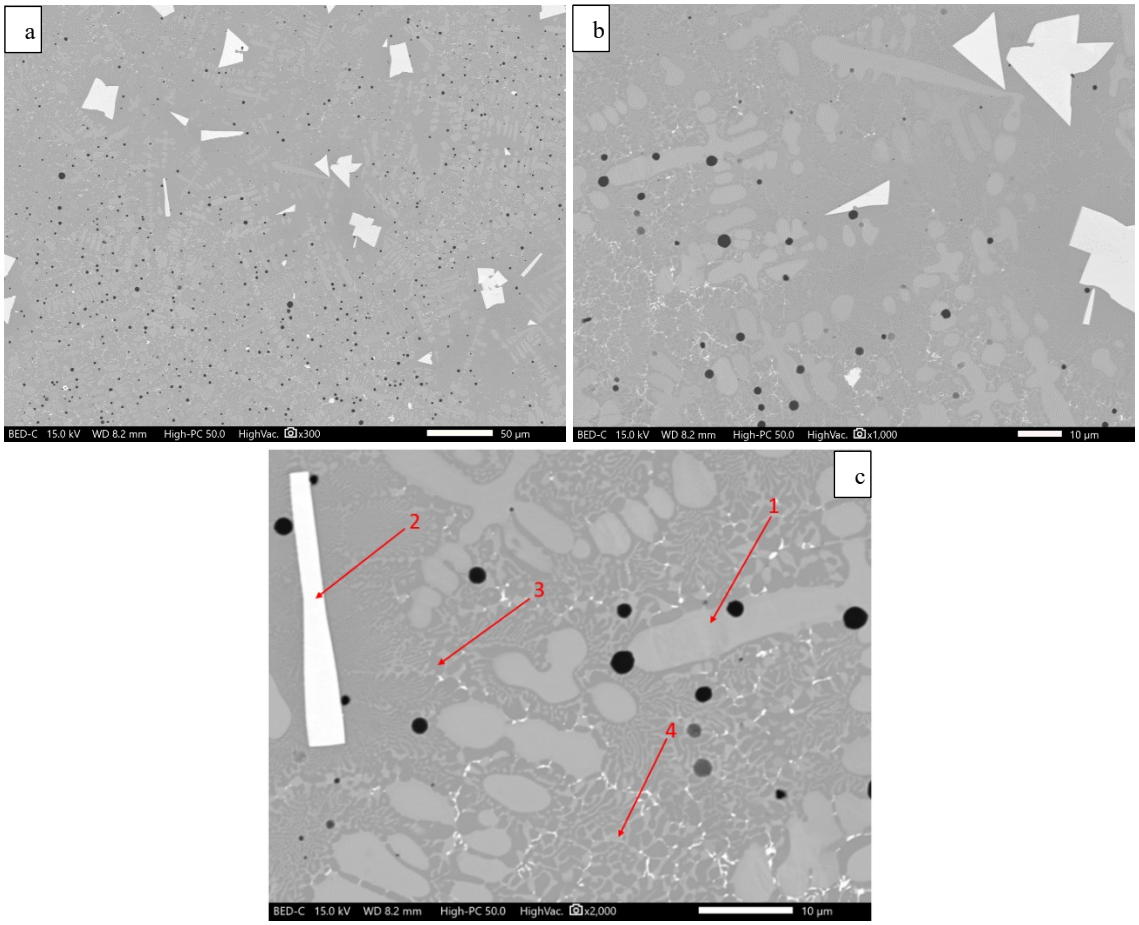

Figure 7.37: *SEM images of NIFD PLUS as clad (a) 300x (b) 1000x (c) 2000x with EDS analysis points*

Table 7.11: *EDS analysis of NIFD PLUS as clad*

Element (wt%)	C	Fe	Ni	W
Position 1	10.69	6.01	64.60	18.70
Position 2	15.25	0.90	4.31	79.54
Position 3	10.38	4.36	80.61	4.65
Position 4	10.39	6.40	70.38	12.83

NIFD PLUS cladded on soft substrate was subjected to heat treatment, a cross section profile of NIFD PLUS in heat-treated condition is presented in Figure 7.38. It can be seen that after heat treatment, severe cracks in the coating as well as in the base metal are produced. Coating was cracked from the middle and crack extended to the base metal, there is also a secondary crack that is produced from the HAZ; on the extreme right side of the Figure 7.38, it is visible that coating has been broken from the corner and middle that can be detached from the clad.

Hardness was measured at a load of 1000g on as clad and heat-treated to compare the variations, see Figure 7.39. The hardness values between as clad and heat-treated a not varied to a great extent, hardness of matrix and carbide were taken separately at a load of 300gm to analyze any specific variations in hardness, see Figure 7.40; hardness of matrix has been suppressed to a certain degree after heat treatment according to Figure 7.40.

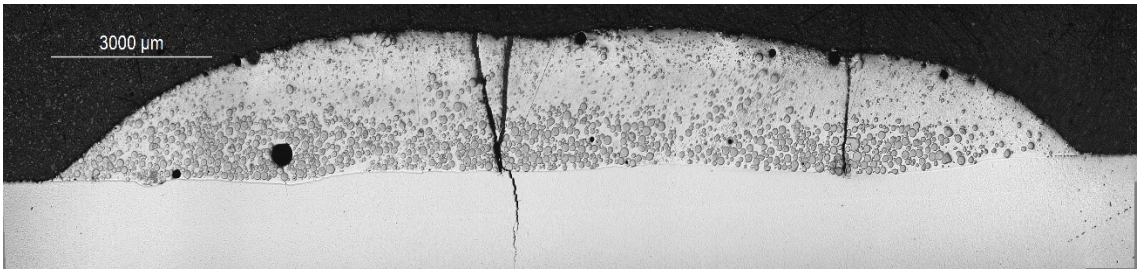

Figure 7.38: *Clad profile of NIFD PLUS heat-treated*

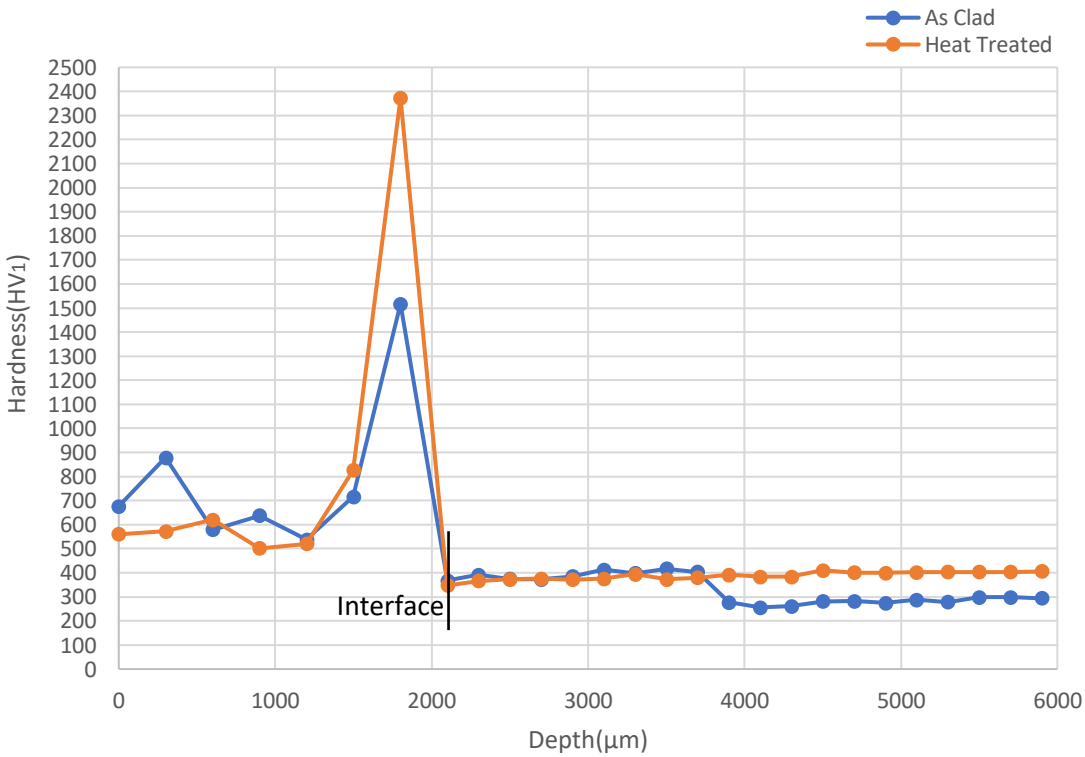

Figure 7.39: *Hardness profile of NIFD PLUS in as clad and heat-treated conditions*

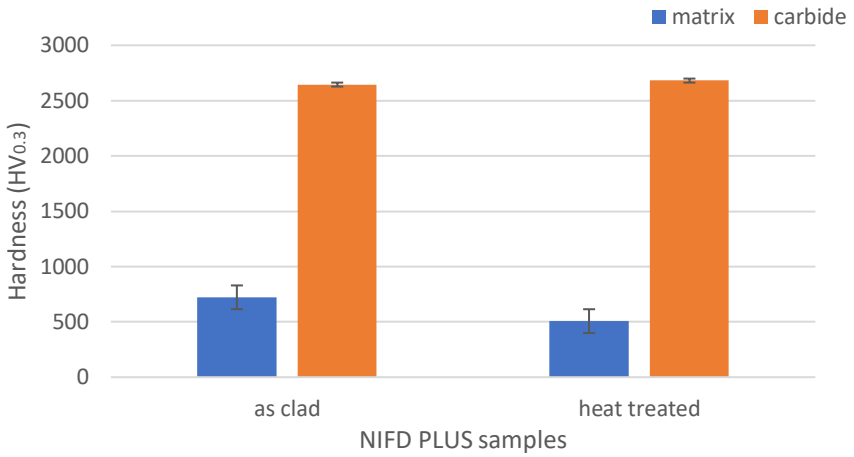

Figure 7.40: *Matrix and carbide hardness of NIFD in as clad and heat-treated state*

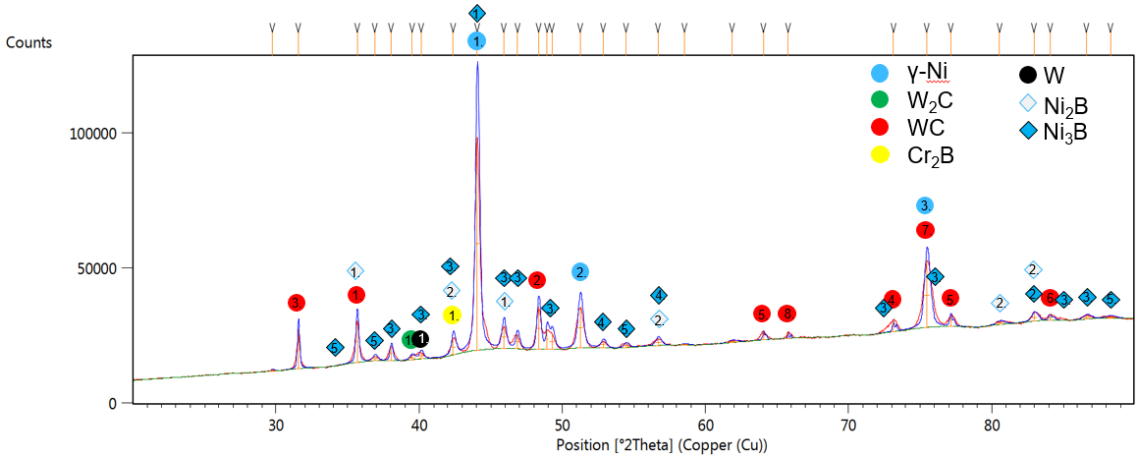

Figure 7.41: *XRD analysis of NIFD PLUS heat-treated*

The hardness of NIFD PLUS matrix is higher as compared to NI2 PLUS; the reason cam be due to precipitation of secondary carbides. XRD analysis were carried out to investigate the phase changes after heat treatment, see Figure 7.41. The XRD pattern gives similar result as of as clad condition and gives no evidence of the suppression of hardness in the matrix. SEM images and EDS analysis were conducted after XRD, Figure 7.42 and table 7.12 presents the SEM images and EDS results respectively. In NI2 PLUS alloy, there were visible cracks at the interface after heat treatment; interface images of NIFD PLUS in both as clad and heat-treated condition were also captured to investigate the cracks, Figure 7.43. It can be seen from Figure 7.43 that cracks are also present in NIFD PLUS as well after heat treatment.

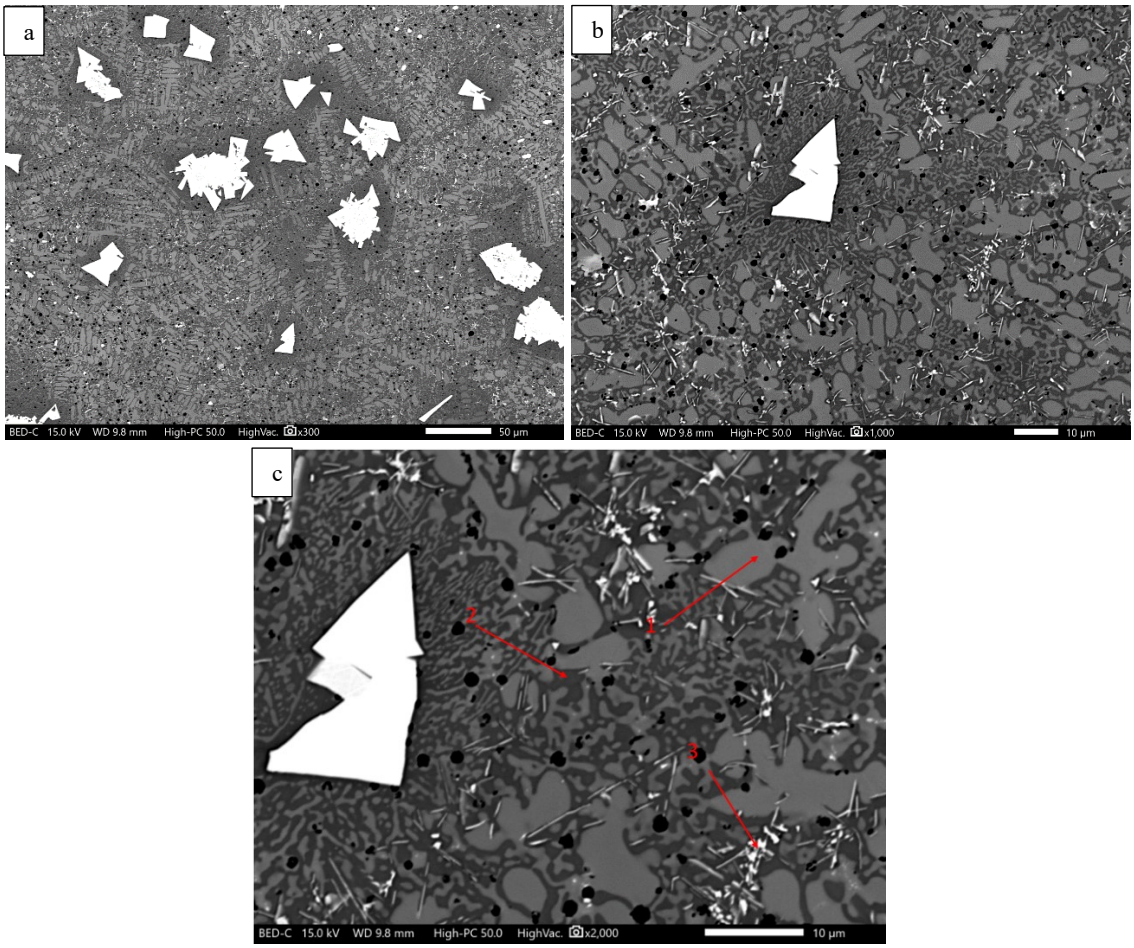

Figure 7.42: *SEM images of NIFD PLUS heat-treated (a) 300x (b) 1000x (c) 2000x with EDS analysis points*

Table 7.12: *EDS analysis of NIFD PLUS heat-treated*

Element (wt%)	C	Fe	Ni	W
Position 1	7.47	3.06	68.04	21.43
Position 2	6.65	2.30	83.74	7.31
Position 3	7.32	1.25	78.00	13.42

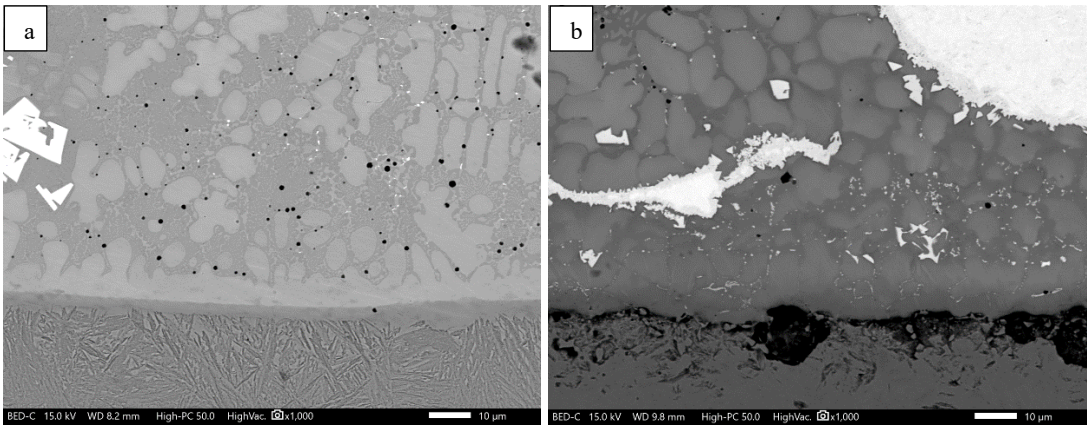

Figure 7.43: *SEM images of NIFD PLUS alloy interface at 1000x (a) as clad (b) heat-treated*

7.2 Impact resistance in hammer mill test

Hammer mill test was conducted at impact frequencies of 7.5Hz and 10.5Hz and two different impact angles for the four selected alloys; So, a total of 16 tests were conducted on hammer mill. The total time of the test was 3 hours and mass loss was calculated after every 30 minutes. Figure 7.44 presents an image of the hammer hitting the specimen at 90˚ angle during the hammer mill test. The values of impact energies and rotation speed of the hammer calculated from the hammer mill test are presented in Table 7.13. The details of the calculation can be found from references [65] and [69].

Figure 7.44: *Image of hammer mill test during the test*

Table 7.13: *Calculated values from the hammer mill test*

Frequency (Hertz)	Impact Energy (Joules)	Angular velocity, ω (rpm)	Impacts per minute
7.5	22	47	94
10.5	31	66	123

Before the test the specimen were tested for hardness measurements and crack density; hardness was measured by Zwick hardness tester at a load of 5 kg. Figure 7.45 shows the graphical representation of average hardness values of hardfacing alloys in as clad and heat-treated conditions. Crack density was measured by stereo microscope, and measurement was taken at three different positions along the specimen in perpendicular and parallel direction to the welding; Table 7.14 shows the average surface crack density for a single position along the parallel and perpendicular welding direction.

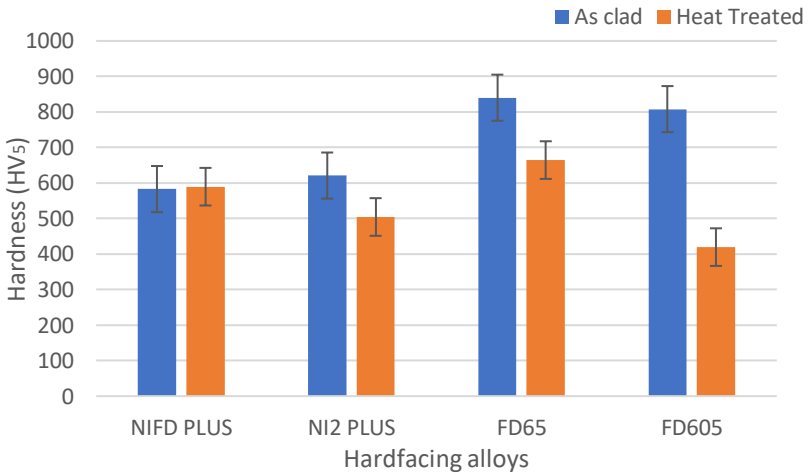

Figure 7.45: *Surface hardness values of hammer mill specimens*

Table 7.14: *Surface crack density (cracks/70mm)*

Alloys	Perpendicular cracks	Parallel cracks
NI2	8	-
NIFD	9	7
FD65	11	6
FD605	-	-

The results of the conducted hammer mill test were recognized with mass loss and wear depth after the test; the mass loss was calculated by a weighing scale while the wear depth was analyzed by Alicona. The results are given separately for each alloy in as clad and heat-treated state in the following chapters.

7.2.1 Impact wear resistance of NI2 PLUS hardfacing alloy

The mass loss results from the hammer mill impact test conducted on NI2 PLUS hardfacing alloy, in as clad and heat-treated state, after 3 hours at an impact frequency of 7.5Hz is presented in Figure 7.46. Figure 7.47 shows an image of NI2 PLUS in as clad state after the hammer mill test at 7.5Hz. After the test, the wear depth of the coating was analyzed by Alicona at three different positions, the average wear depth for the three positions is shown in Figure 7.48.

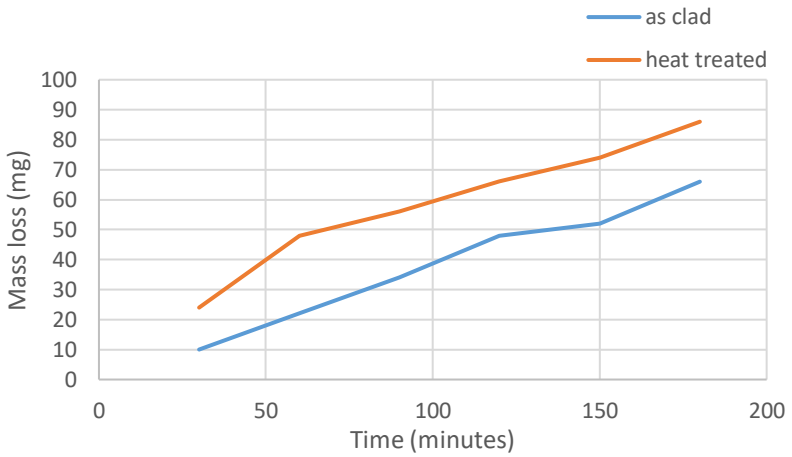

Figure 7.46: *Cumulative mass loss of NI2 PLUS in as clad and heat-treated condition from hammer mill at 7.5Hz*

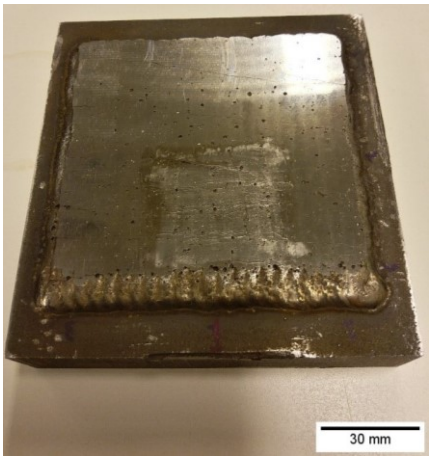

Figure 7.47: *NI2 PLUS as clad after hammer mill test*

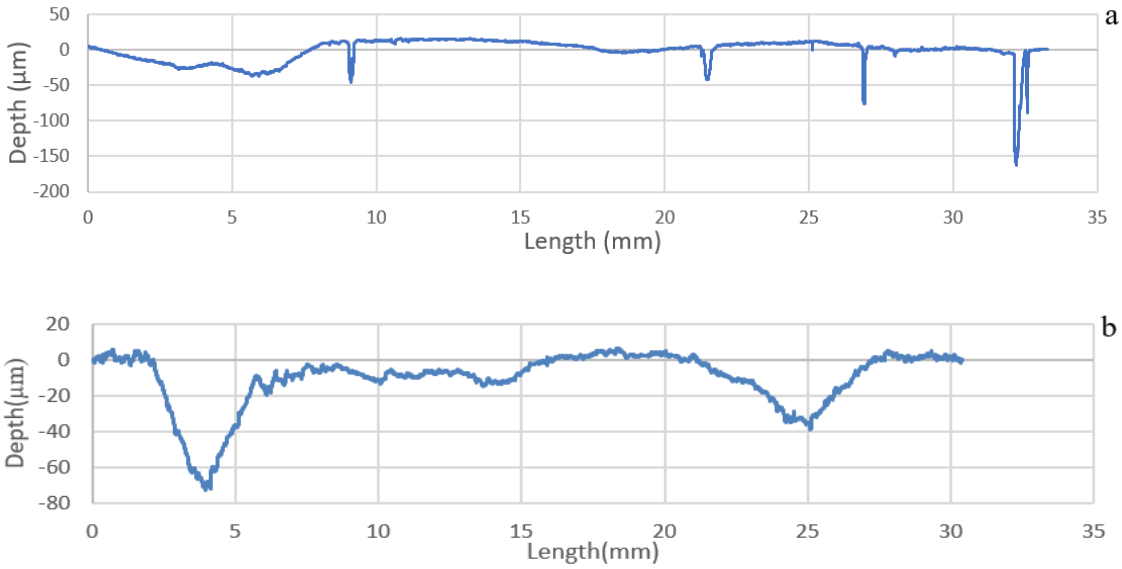

Figure 7.48: *Wear depth profile of NI2 PLUS at 7.5Hz impact frequency (a) as clad (b) heat-treated*

From Figures 7.46 and 7.48, it can be seen that mass loss and wear depth are very slightly on the higher side in heat-treated condition. The mass loss results from NI2 PLUS alloy tested by hammer mill at higher impact energy is presented in Figure 7.49; the wear depth analysis is shown in Figure 7.50. Heat-treated specimens showed elevated wear and higher wear depth as compared to as clad in 10.5Hz as well, as shown by Figures 7.49 and 7.50.

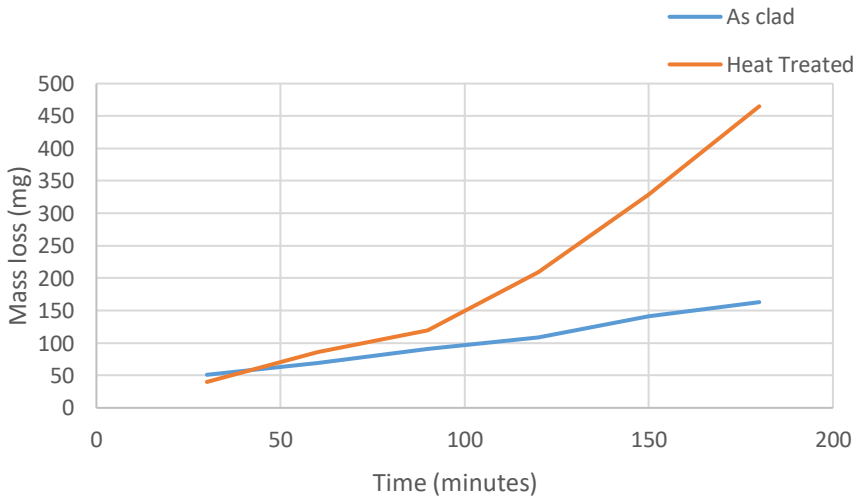

Figure 7.49: *Mass loss of NI2 PLUS as a function of test time in as clad and heat-treated condition from hammer mill at 10.5Hz*

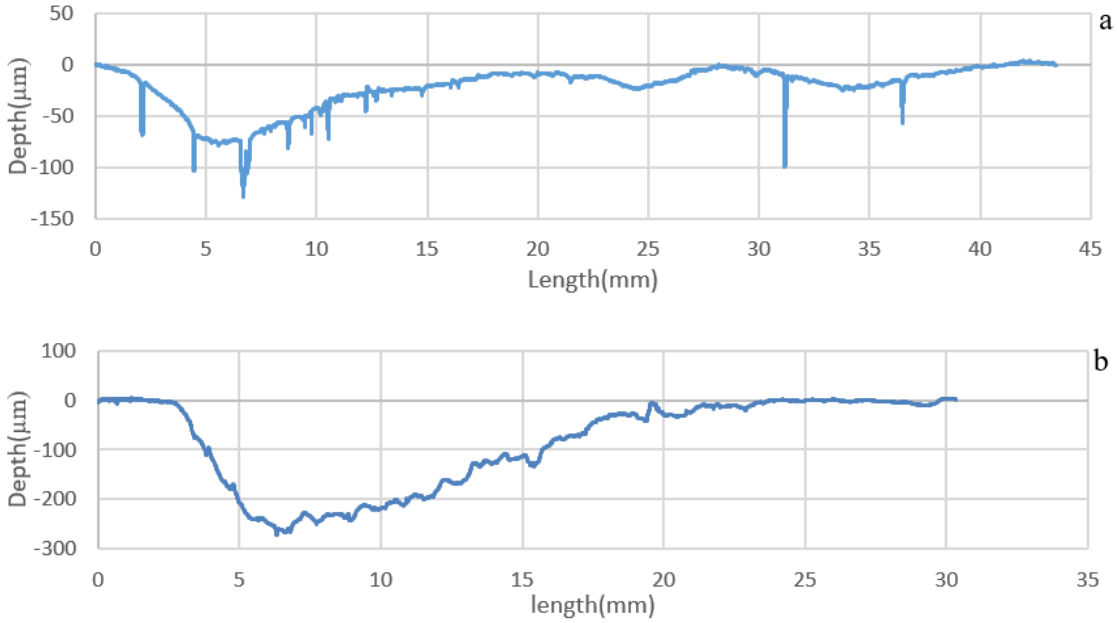

Figure 7.50: *Wear depth of NI2 PLUS at 10.5Hz (a) as clad (b) heat-treated*

7.2.2 Impact wear resistance of FD65 hardfacing alloy

Hammer mill results of FD65 alloy at an impact frequency of 7.5Hz are presented in Figure 7.51; the results indicate that heat-treated specimens show larger wear loss. The mass loss is higher at the initial impact cycle and the impact resistance seems to increase with increasing impacts; the wear depths of the specimens are shown in Figure 7.52. The mass loss results from 10.5Hz cycle is presented in Figure 7.53 and the wear depth of as clad and heat-treated specimens are presented in Figure 7.54.

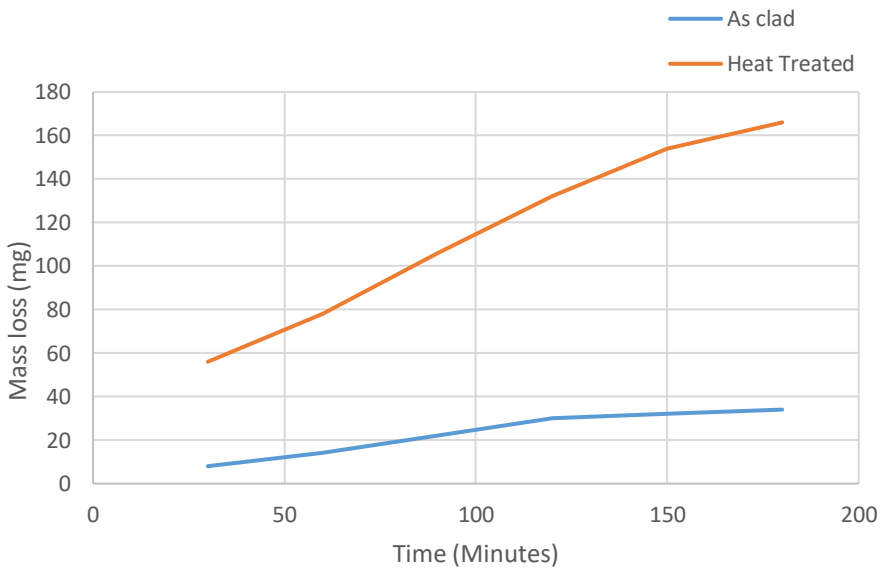

Figure 7.51: *Mass loss of FD65 as a function of test time in as clad and heat-treated condition from hammer mill at 7.5Hz*

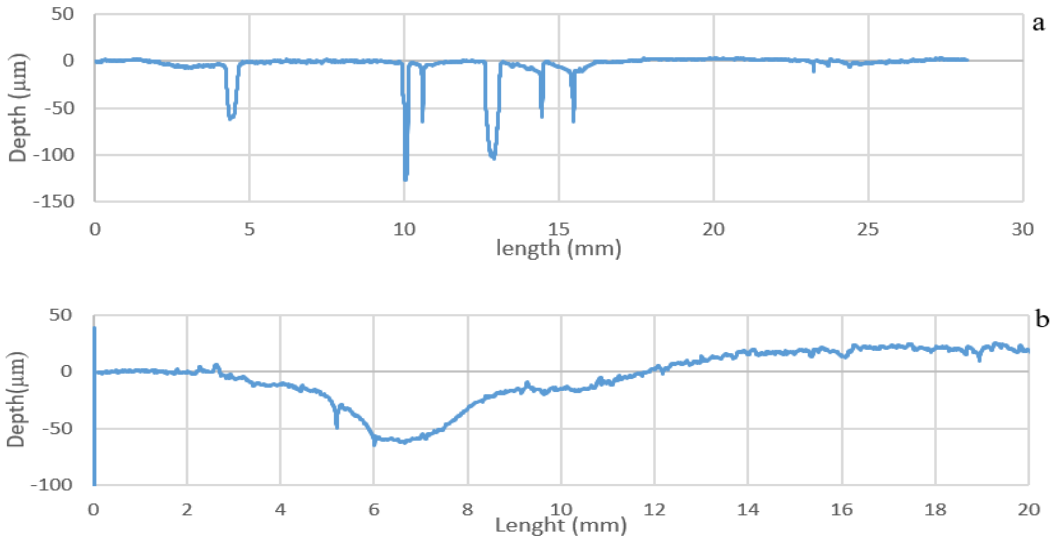

Figure 7.52: *Wear depth analysis of FD65 at 7.5Hz (a) as clad (b) heat-treated*

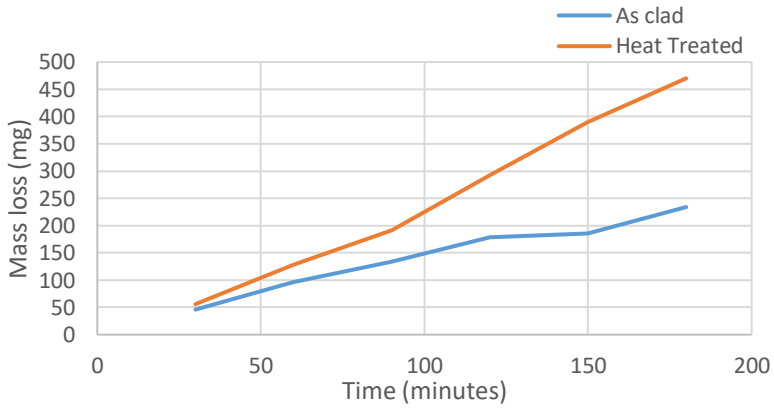

Figure 7.53: *Mass loss of FD65 as a function of test time in as clad and heat-treated condition from hammer mill at 10.5Hz*

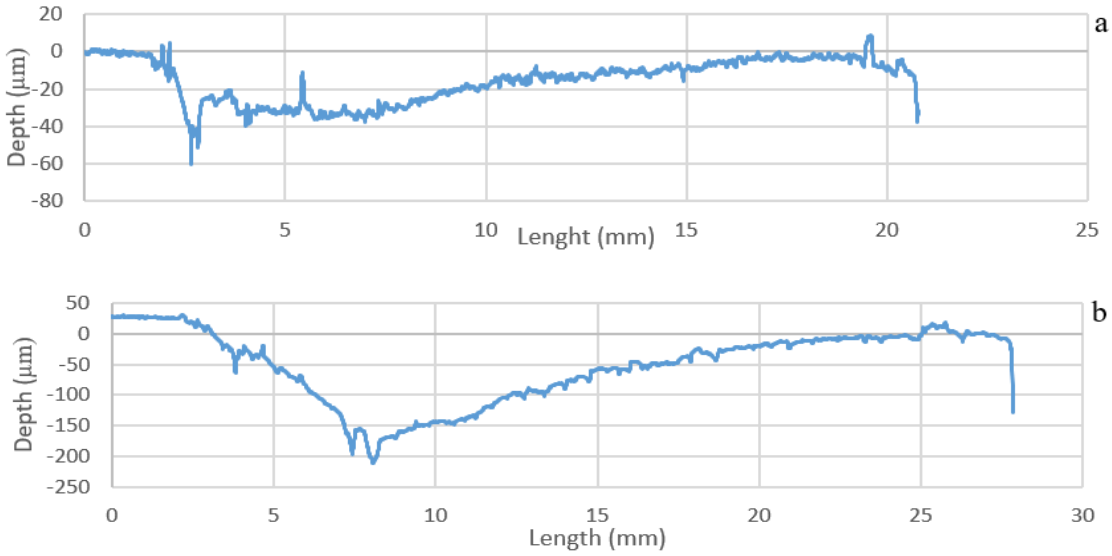

Figure 7.54: *Wear depth analysis of FD65 at 10.5Hz (a) as clad (b) heat-treated*

7.2.3 Impact wear resistance of FD605 hardfacing alloy

The mass loss of FD605, in as clad and heat-treated, condition from hammer mill test at an impact frequency of 7.5Hz is presented in Figure 7.55; the wear depth results from Alicona is presented in Figure 7.56. The mass loss is very small as compared to other selected hardfacing alloys; the reason seems to be the absence of cracks and porosity, Figure 7.57 shows an image of FD605 specimen after hammer mill test. Next hammer mill test on FD605 was conducted at 10.5Hz, the results of mass loss and wear depth are presented in Figure 7.58 and 7.59 respectively. The mass loss is on the slightly higher degree in second test, but that is mainly due to higher impact energies.

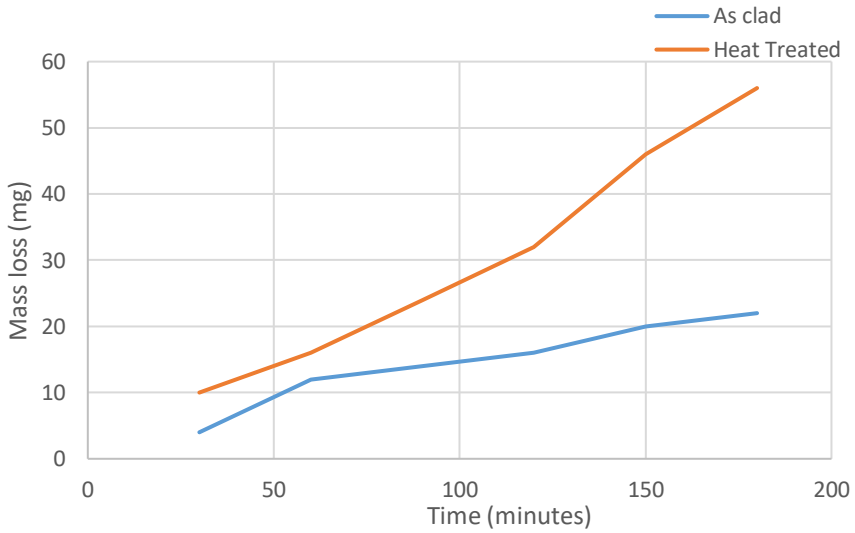

Figure 7.55: *Mass loss of FD605 as a function of test time in as clad and heat-treated condition from hammer mill at 7.5Hz*

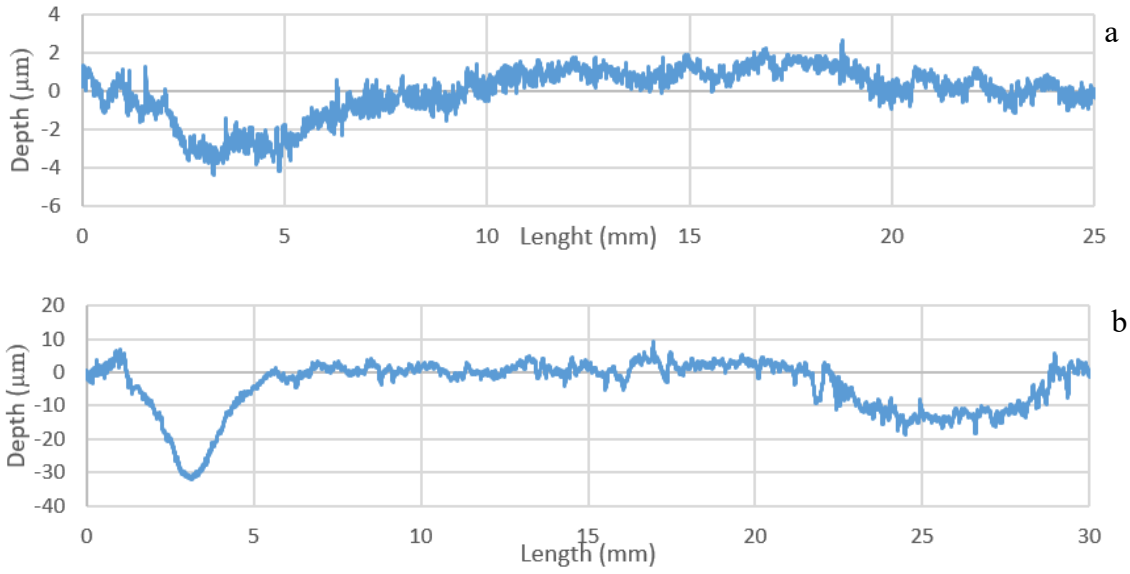

Figure 7.56: *Wear depth profile of FD605 at 7.5Hz (a) as clad (b) heat-treated*

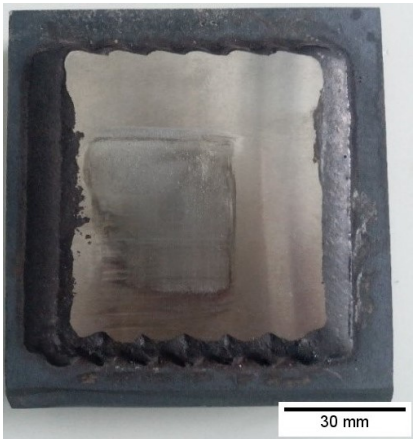

Figure 7.57: *FD605 specimen after hammer mill test*

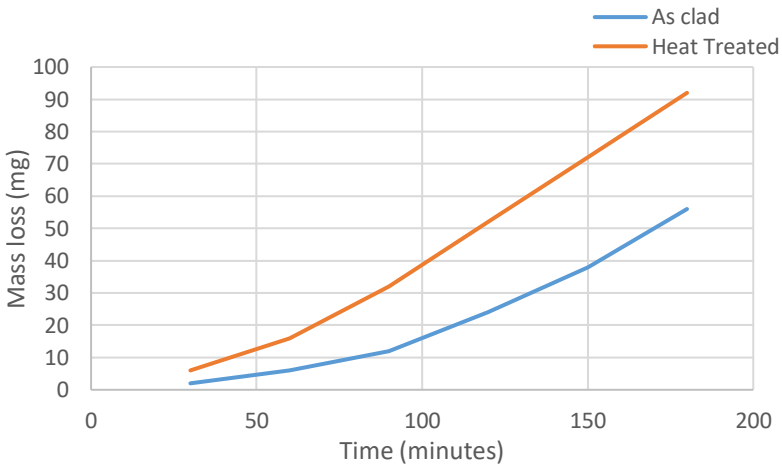

Figure 7.58: *Mass loss of FD605 as a function of test time in as clad and heat-treated condition from hammer mill at 10.5Hz*

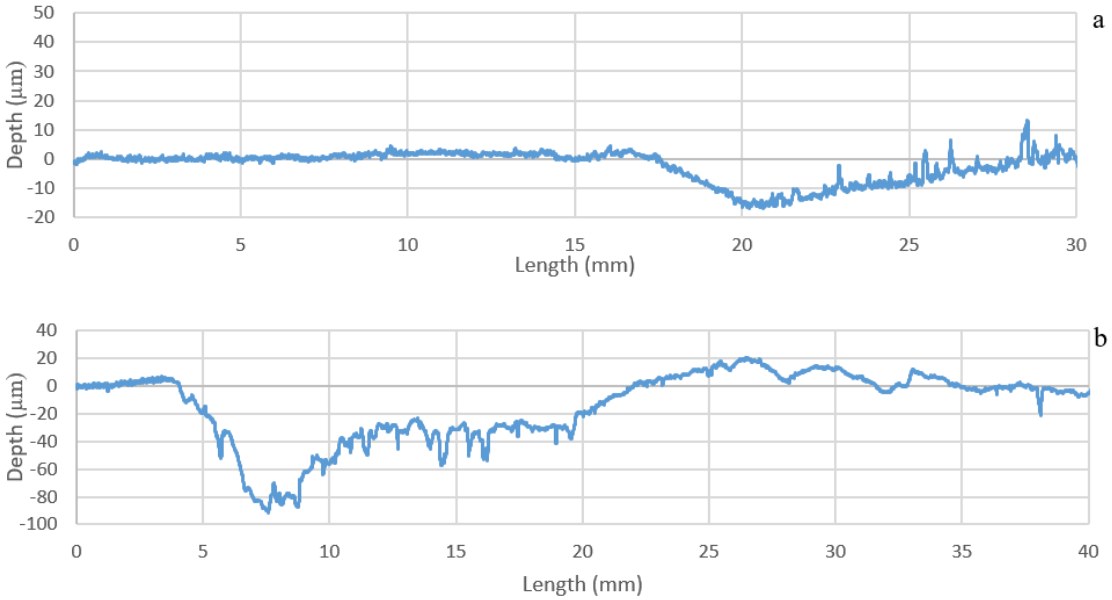

Figure 7.59: *Wear depth of FD605 at 10.5Hz (a) as clad (b) heat-treated*

7.2.4 Impact wear resistance of NIFD PLUS hardfacing alloy

Figure 7.60 presents the mass loss of NIFD PLUS alloy by hammer mill test at 7.5Hz, the wear depth analysis is given in Figure 7.61. The mass loss basically occurred by particle separation by the propagation of cracks; the cracks became more visible after each impact cycle. The results from 10.5Hz are shown in Figure 7.62, while the wear depth analysis is presented in Figure 7.63; it can be seen that heat-treated specimens suffered a high mass at high impact energies and at a different angle.

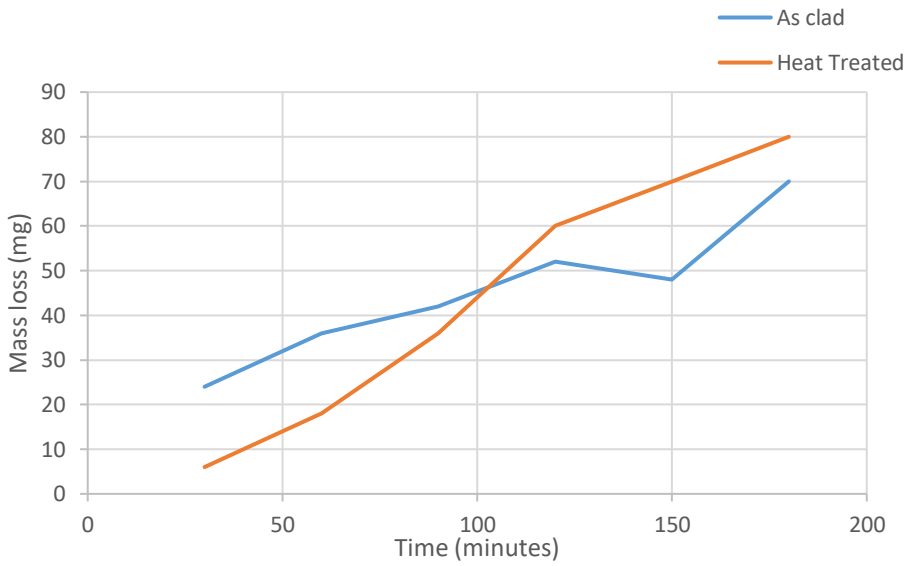

Figure 7.60: *Mass loss of NIFD PLUS as a function of test time in as clad and heat-treated condition from hammer mill at 7.5Hz*

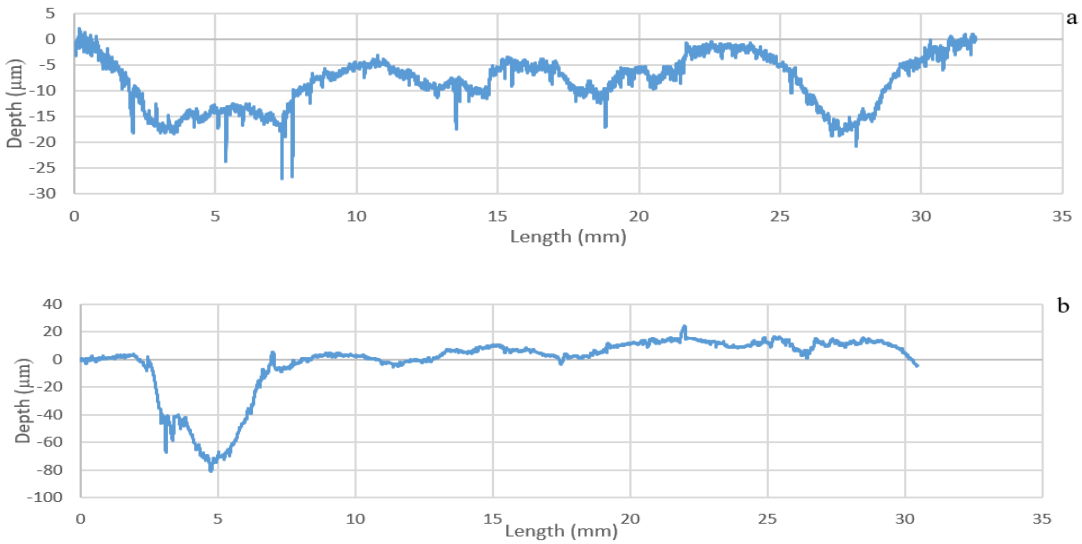

Figure 7.61: *Wear depth profile of NIFD PLUS at 7.5Hz (a) as clad (b) heat-treated*

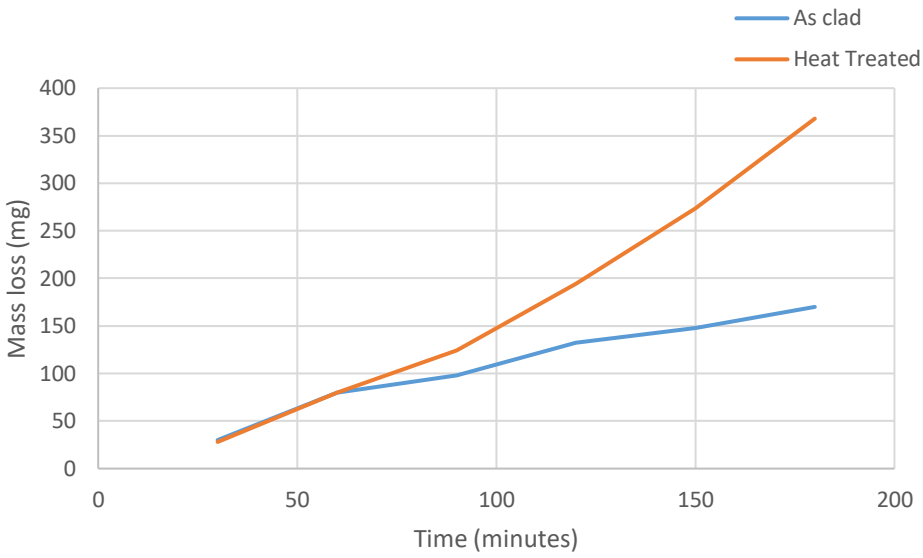

Figure 7.62: *Mass loss of NIFD PLUS as a function of test time in as clad and heat-treated condition from hammer mill at 10.5Hz*

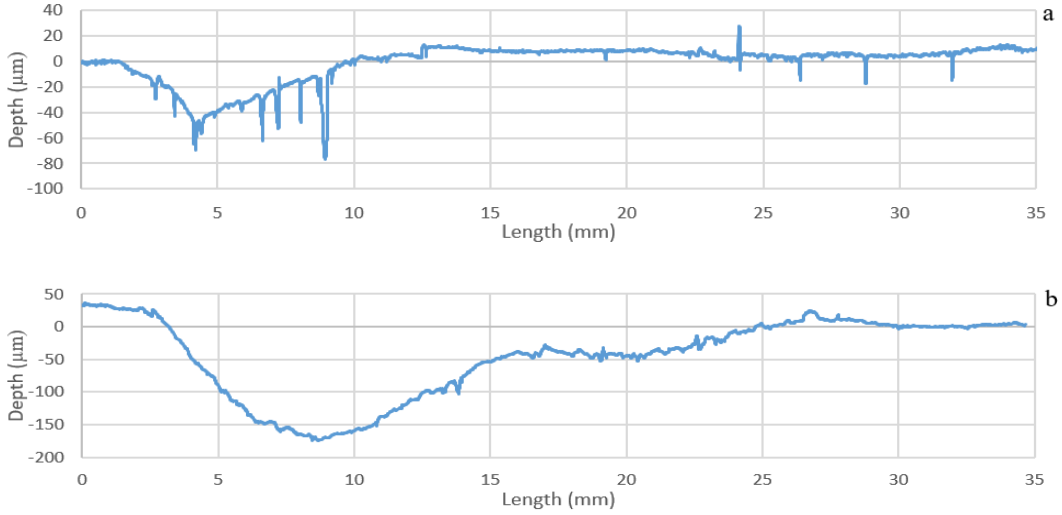

Figure 7.63: *Wear depth analysis of NIFD PLUS at 10.5Hz (a) as clad (b) heat-treated*

A summary of hammer mill results is given in Figure 7.64, it can clearly be deduced that overall heat-treated specimens resulted in a high loss. In case of nickel based alloys, the wear was similar for as clad and heat-treated at low impact energies; but at high impact energies as clad provided better impact resistance properties.

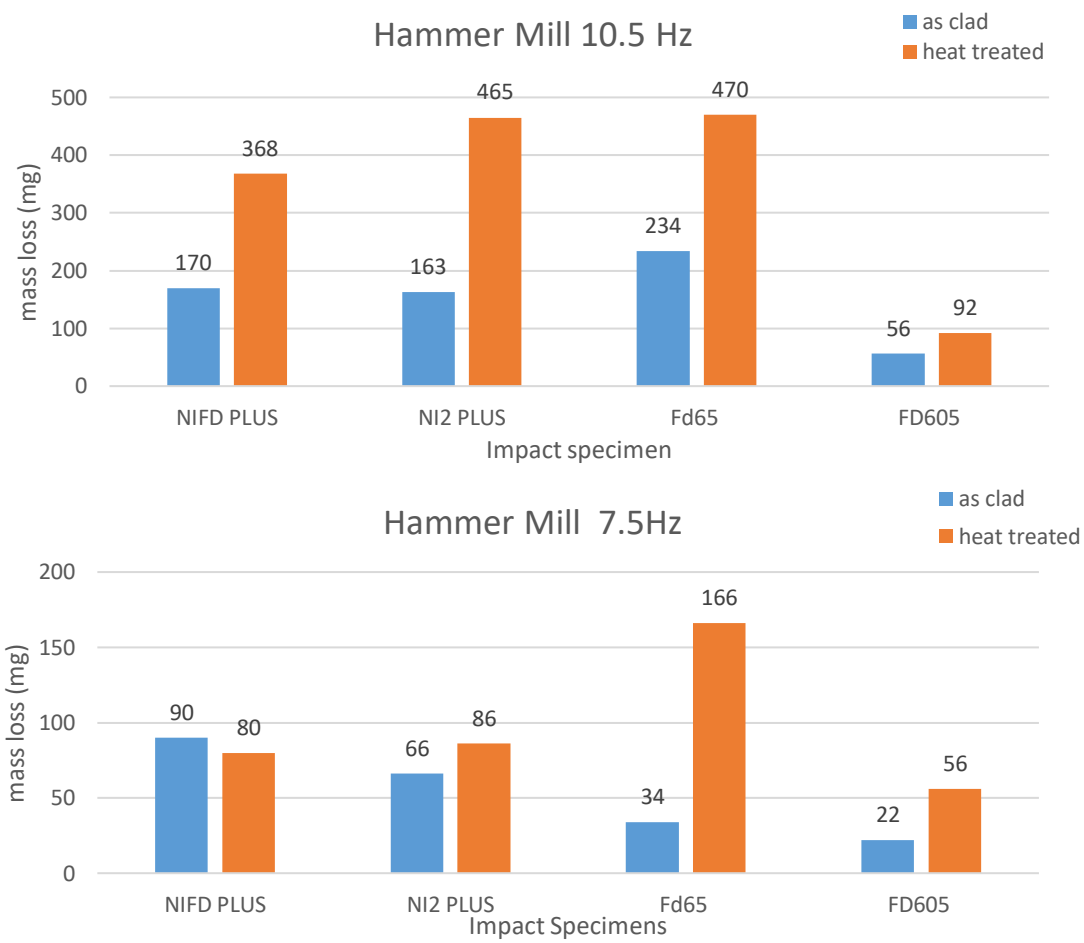

Figure 7.64: *Hammer Mill results at both impact frequencies*

7.3 Heat affected zone cracks

After the hammer mill test, as clad FD605 specimen tested at 10.5Hz was cut in half to locate if there were any cracks produced after the test. Figure 7.65 shows the image of interface of as clad FD605 at a magnification of 5x obtained by optical microscopy, it can be seen that no HAZ cracks appeared in the base metal after impacts from hammer mill test at an impact frequency of 10.5Hz

Figure 7.65: *FD605 interface at 5x magnification for HAZ crack observation*

7.4 Pulse Jet erosion wear test results

As described before, pulse jet was conducted for every hardfacing alloy in their as clad and heat-treated condition at 90˚ and 0˚ impingement angles; two specimens for 0˚ and one for 90˚, Figure 7.66. The test was to be conducted for 40,000 pulses and mass loss be measured after every 10,000 pulses. 5 kg granite particles were used in every test with a size distribution <4mm.

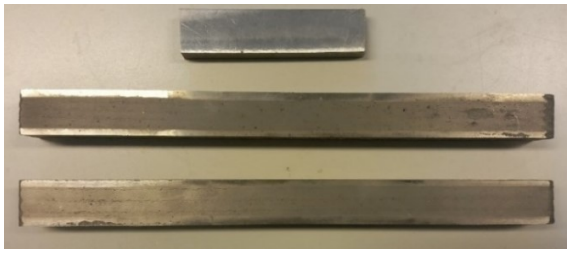

Figure 7.66: *Pulse jet specimens, two 240 mm 0˚ degree and one 87 mm 90˚ samples*

Before the test, the specimens were photographed with stereomicroscope and tested for hardness measurements, Figure 7.67 presents the stereomicroscopic images and Figure 7.68 shows the hardness measurements. From Figure 7.67, it is visible that every alloy has its unique features; FD65 has a higher crack density and high pores at the surface, NI2 PLUS has lower porosity and light cracks at the surface, FD605 has no cracks and no porosity just some minor grinding scratches and NIFD PLUS has light cracks between the weaving beads; they are due to overlapping of the beads and because the grinding could not be conducted appropriately because of WC/W_2C.

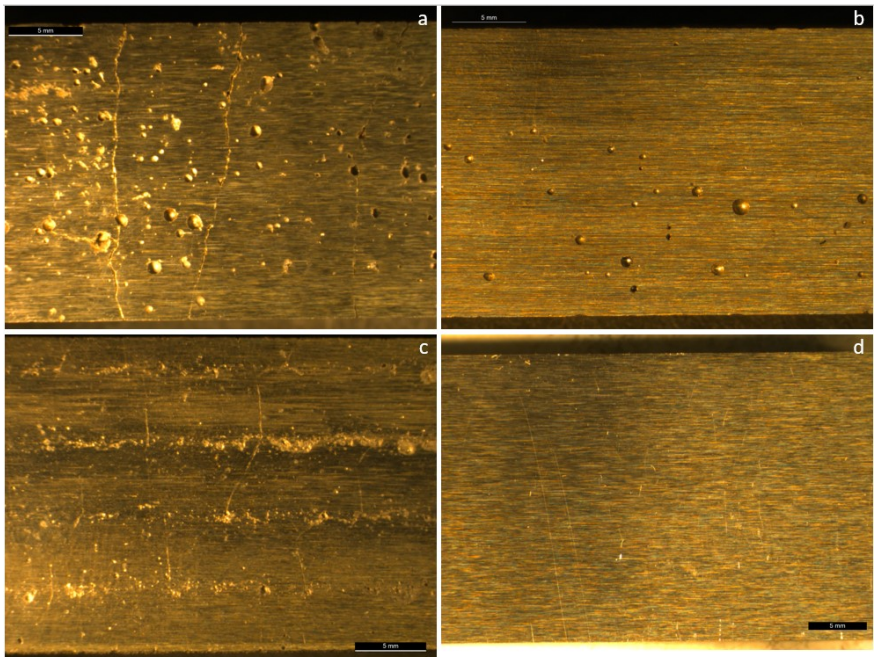

Figure 7.67: *Stereo microscopic images at 0.5x magnification (a) FD65 (b) NI2 PLUS (c) NIFD PLUS (d) FD605*

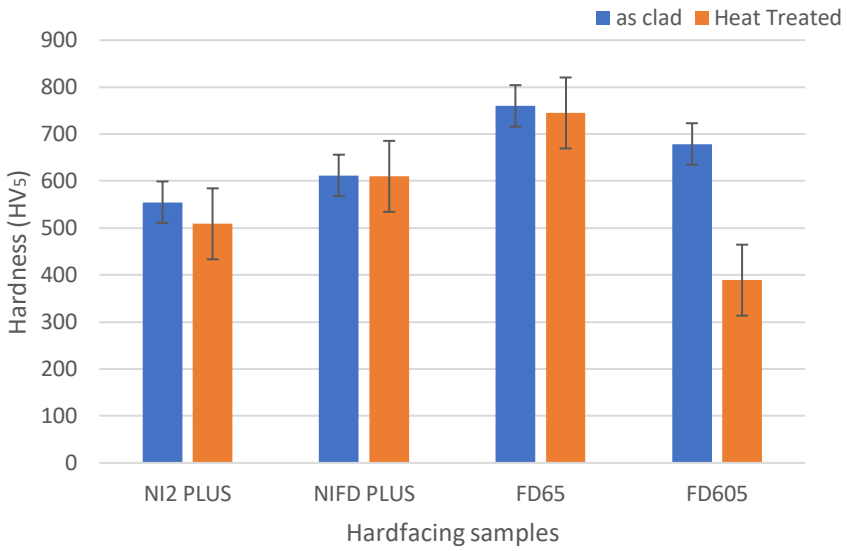

Figure 7.68: *Surface hardness of pulse jet specimen in as clad and heat-treated condition*

The results acquired from pulse jet test are presented in the following section for every hardfacing alloy at two different angles. After the test, the specimens were analyzed for their wear depth with Alicona. During the test, it was Figured that edges of the specimens have a higher wear rate than the center of the specimen, so wear rate of the edge and of the center are discussed. It was also found out that both the 0˚ specimens have similar wear rate, so the results from Alicona are presented for only one 0˚ sample. In some mass loss results in the following section, both 0˚ samples could not be tested with pulse jet, which was due to the inappropriate grinding.

7.4.1 Erosion wear results of NI2 PLUS hardfacing alloy

The mass loss of NI2 PLUS, in as clad and heat-treated condition, at parallel and perpendicular angles is presented in Figure 7.69. The mass losses of heat-treated specimen are slightly higher as compared to as clad specimens. Figure 7.70 shows the center profile of the 0˚ specimen and Figure 7.71 shows the edge profile of the 0˚ specimen along with Alicona wear images. Figure 7.72 shows the Alicona image and wear profile of 90˚ NI2 PLUS as clad specimen.

Figure 7.73 shows the center and edge wear profile of 0˚ NI2 PLUS heat-treated specimens and Figure 7.74 shows the wear profile of 90˚ heat-treated specimen.

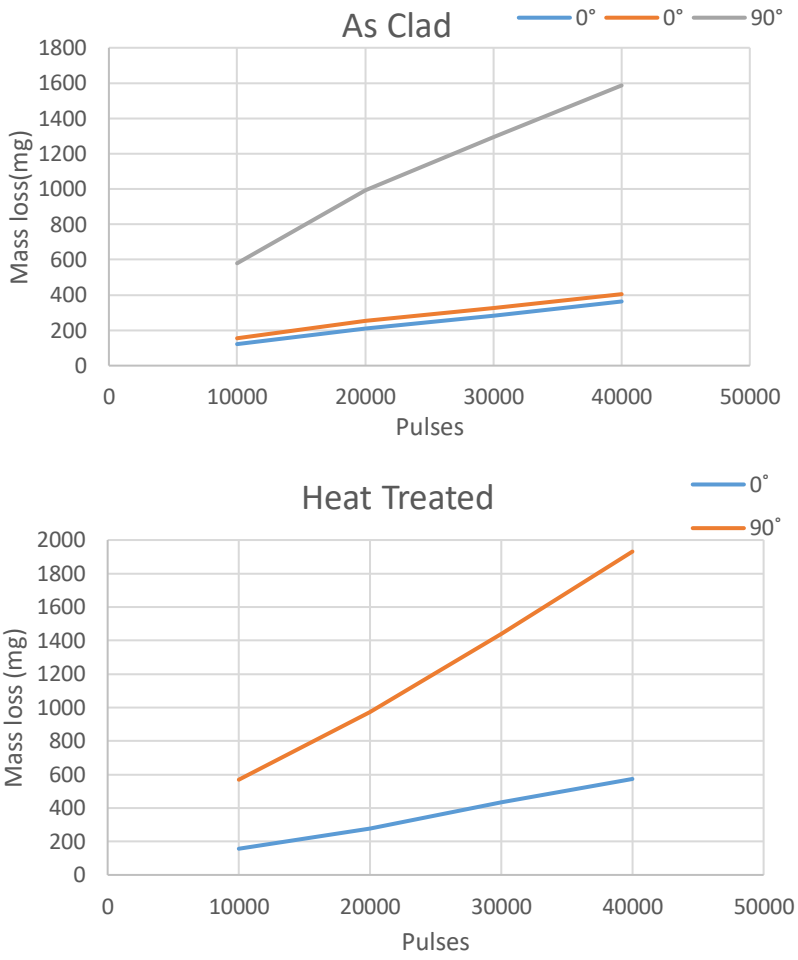

Figure 7.69: *Pulse jet result of NI2 PLUS in as clad and heat-treated conditions*

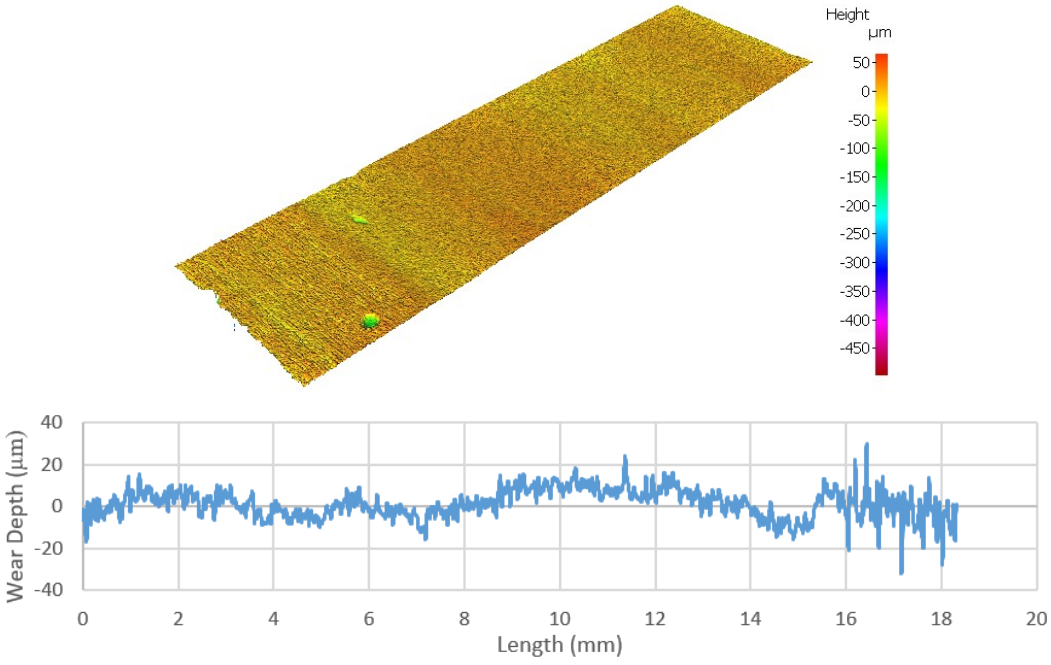

Figure 7.70: *Center wear profile of NI2 PLUS as clad 0˚ specimen*

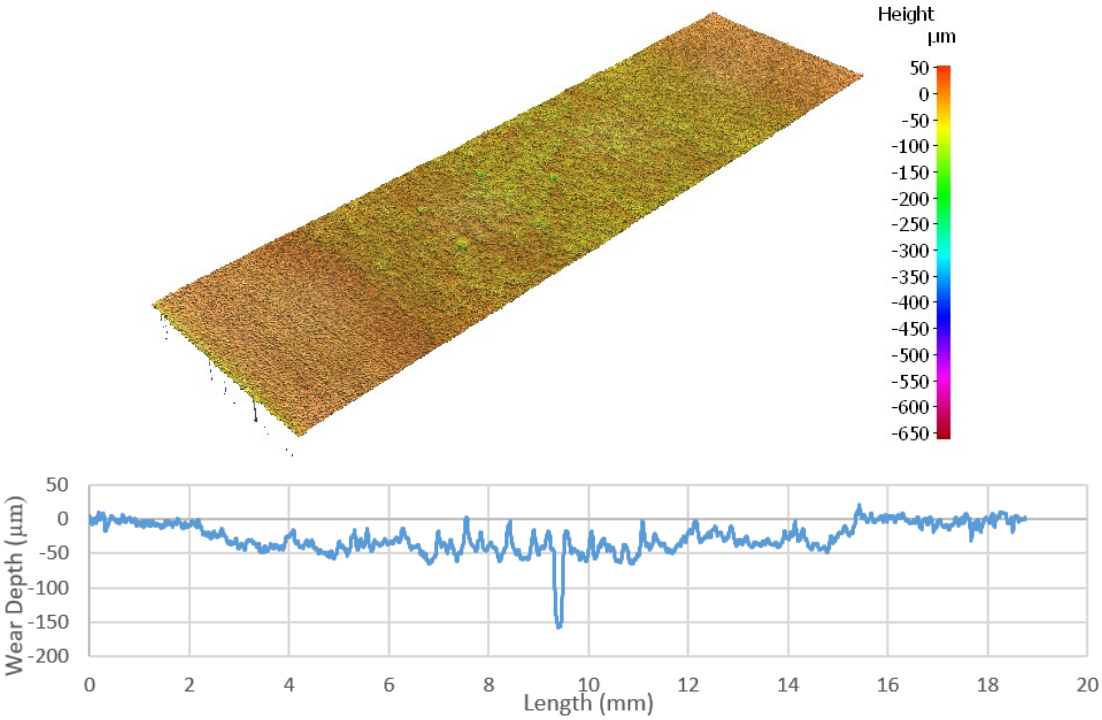

Figure 7.71: *Edge wear profile of NI2 PLUS as clad 0˚ specimen*

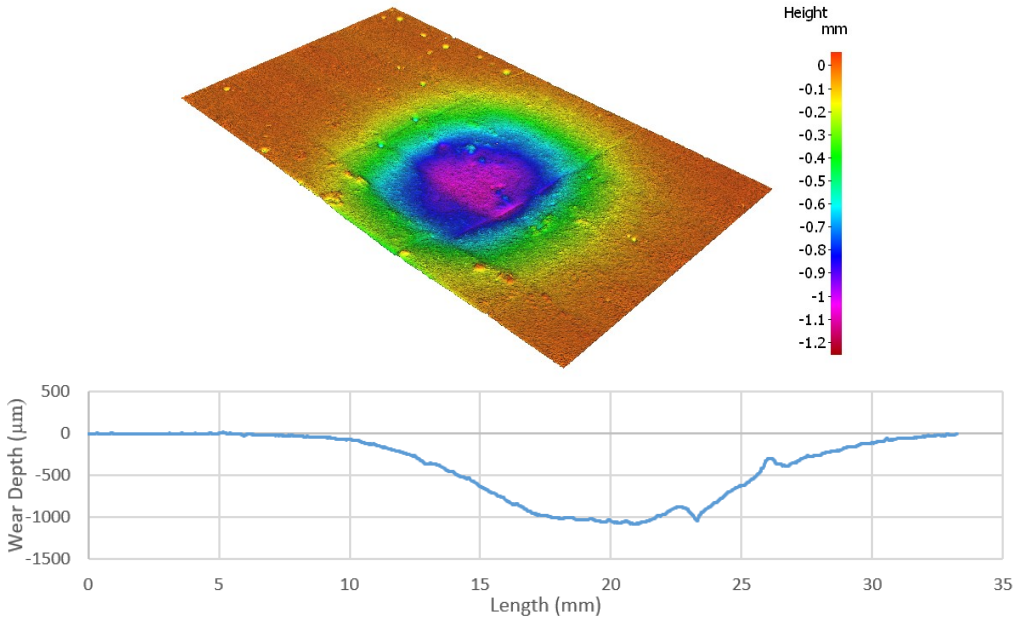

Figure 7.72: *Wear profile of NI2 PLUS as clad 90˚ specimen*

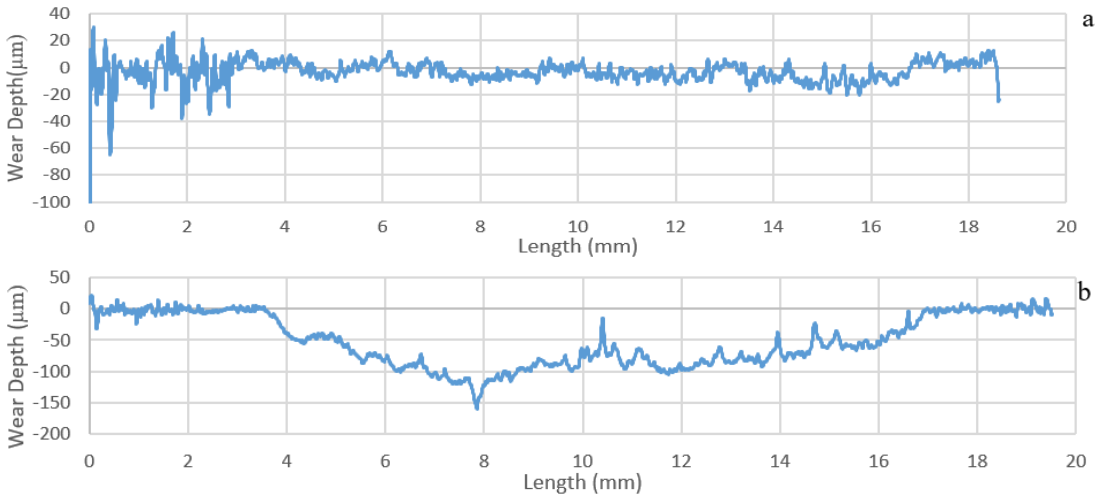

Figure 7.73: *NI2 PLUS heat-treated 0˚ specimen wear profile (a) center (b) edge*

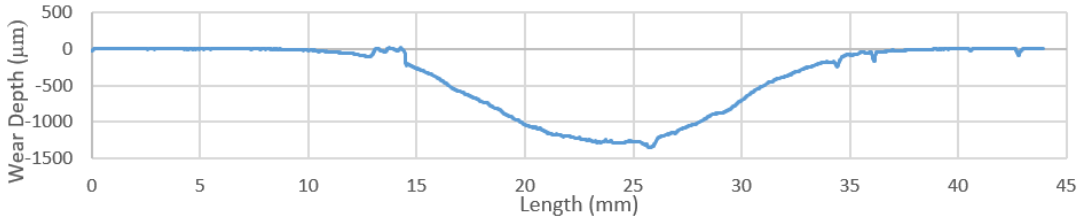

Figure 7.74: *NI2 PLUS heat-treated 90˚ specimen wear profile*

7.4.2 Erosion wear results of FD65 hardfacing alloy

Figure 7.75 shows the graphical representation of the results acquired from the pulse jet test conducted on FD65 in as clad and heat-treated conditions. Generally, the wear rate decreases after the interval of 10,000 pulses for both angles in the two graphs. The profile of 90˚ as clad specimen is presented in Figure 7.76 and the profile of 0˚ specimen, center and edge profile, is shown in Figure 7.77.

Figure 7.78 presents the wear profile of FD65 heat-treated specimen at parallel impingement angle and Figure 7.79 shows the profile of perpendicular impingement angle. Results of Alicona show that the wear depth of edge is higher as compared to center and also wear depth of NI2 PLUS alloy at both angles is higher as compared to FD65 with their respective specimens.

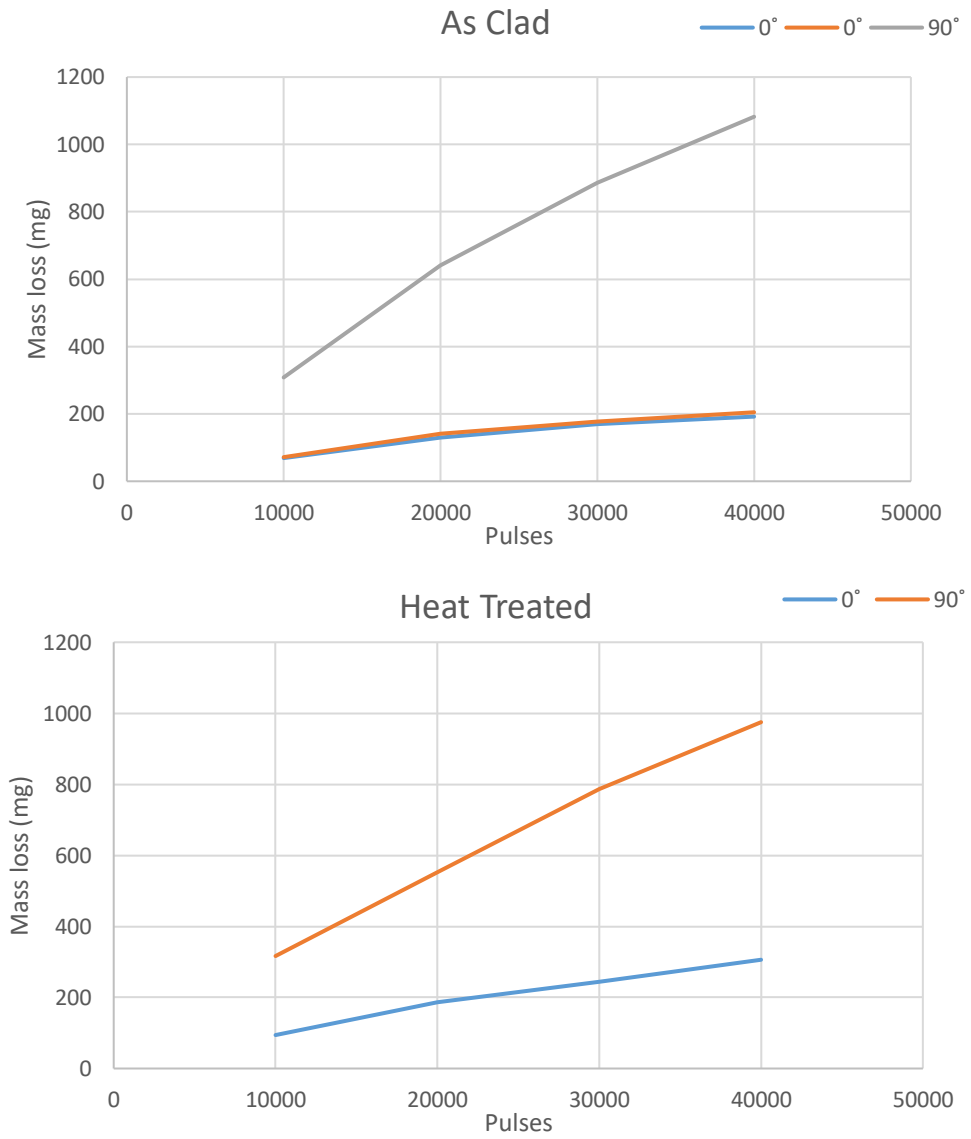

Figure 7.75: *Pulse jet result of FD65 in as clad and heat-treated conditions*

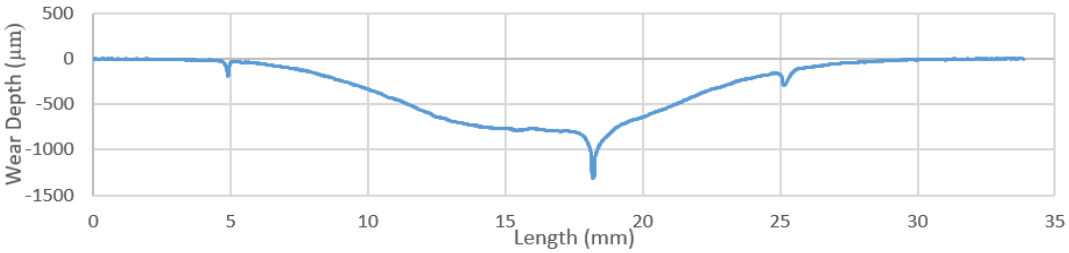

Figure 7.76: *Wear profile of as clad FD65 90˚ specimen*

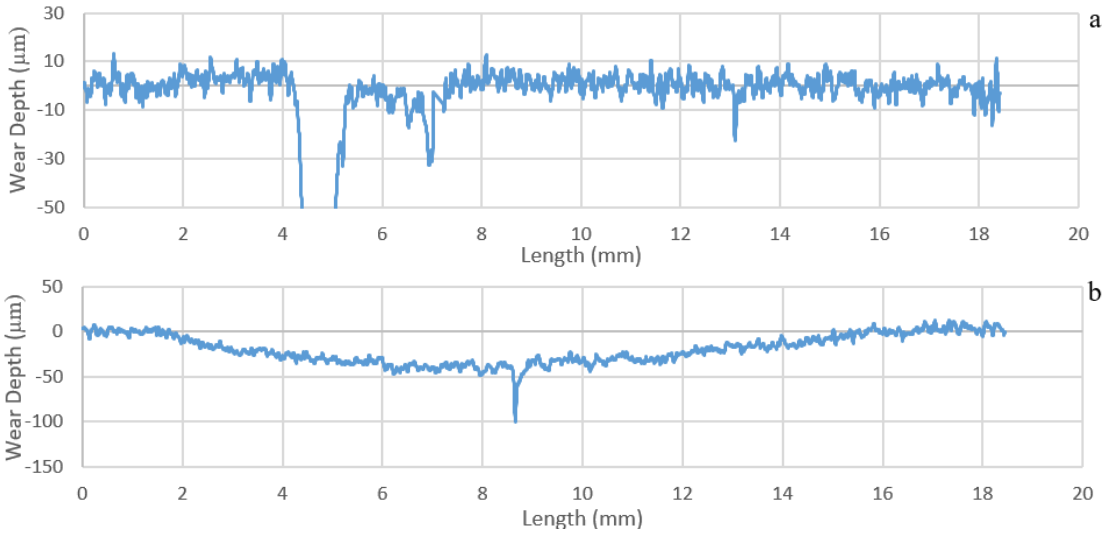

Figure 7.77: *FD65 as clad specimen wear profile (a) center (b) edge*

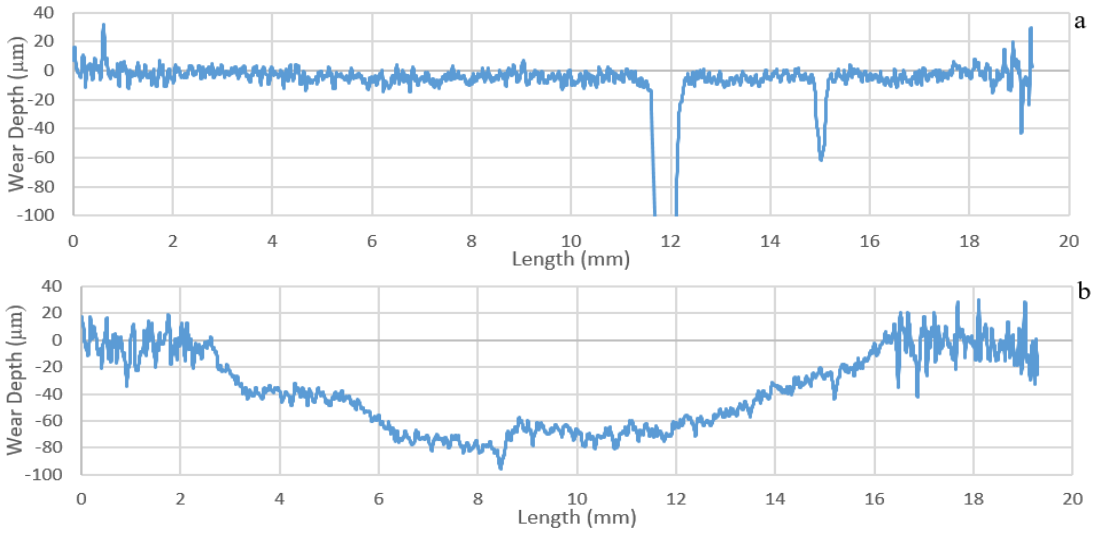

Figure 7.78: *FD65 heat-treated 0˚ specimen wear profile (a) center (b) edge*

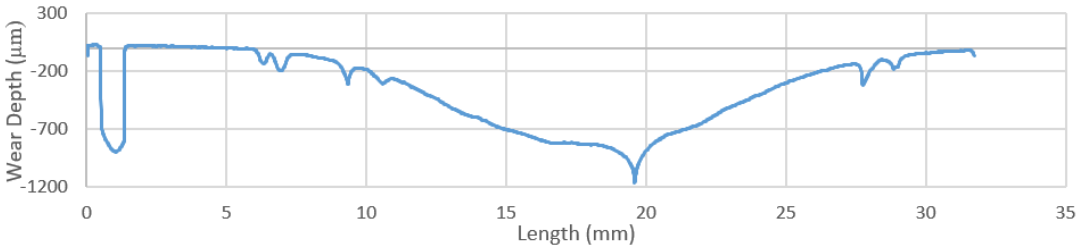

Figure 7.79: *Wear profile of heat-treated FD65 90˚ specimen*

7.4.3 Erosion wear results of FD605 hardfacing alloy

Analysis of erosion loss by pulse jet conducted on FD605 are presented in Figure 7.80, as analyzed in the previous materials as well, heat-treated specimens show a higher mass loss than as clad. Wear profile analysis by Alicona on as clad specimens are presented in Figure 7.81 and 7.82; Figure 7.81 presents the 0˚ specimen analysis and Figure 7.82 presents the 90° specimen analysis.

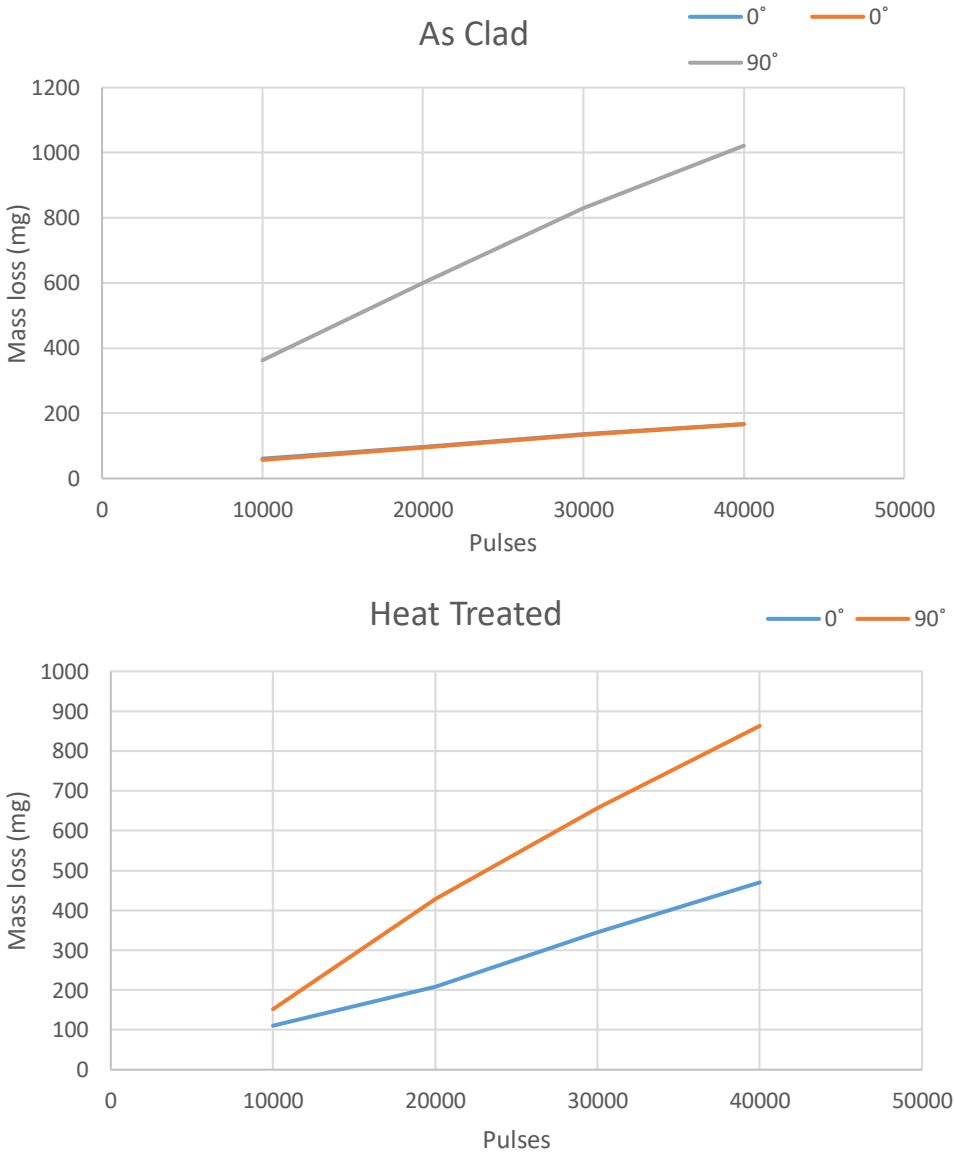

Figure 7.80: *Pulse jet result of FD605 in as clad and heat-treated conditions*

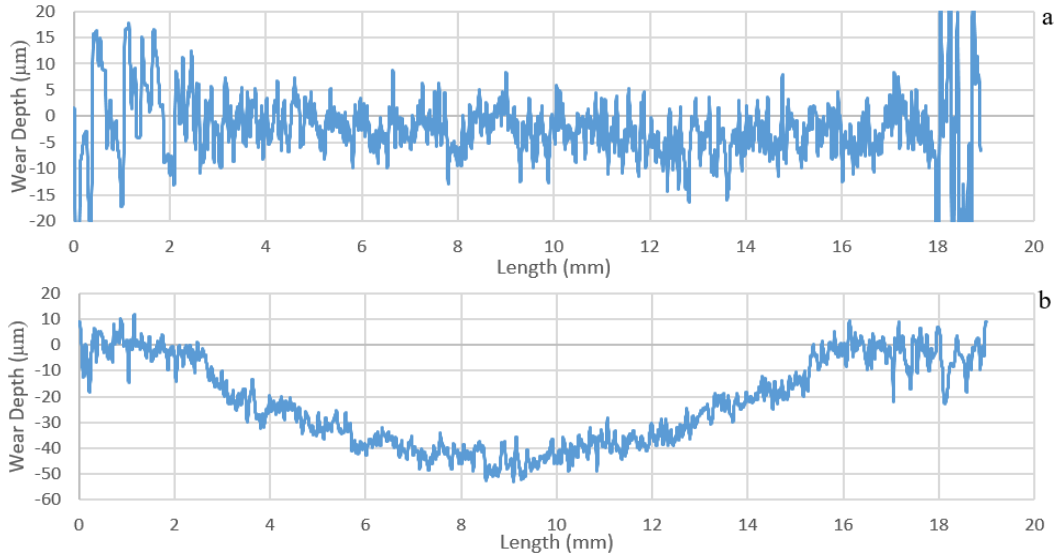

Figure 7.81: *FD605 as clad specimen 0˚ wear profile (a) center (b) edge*

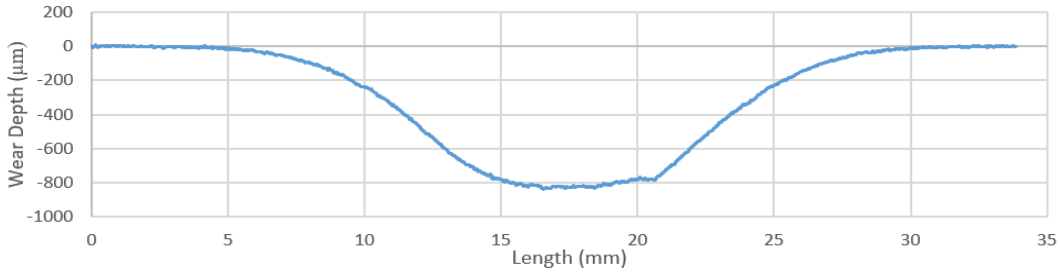

Figure 7.82: *Wear profile of as clad FD605 90˚ specimen*

The wear depth of FD605 in as clad condition is low, just around 10µm and 40µm for parallel samples, as compared to NI2 PLUS. Figure 7.83 shows the wear depth of FD605 heat-treated 90° specimen, and Figure 7.84 shows the wear depth of 0° specimens. The depth is same for 90° specimen but the depth is higher when comparing edge and center profile of as clad specimens.

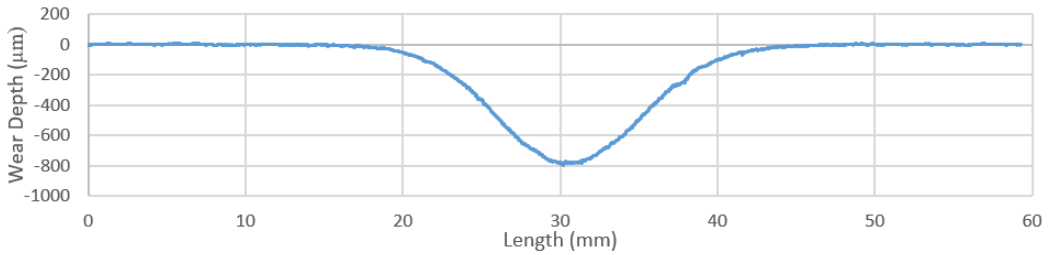

Figure 7.83: *Wear profile of heat-treated FD605 90° specimen*

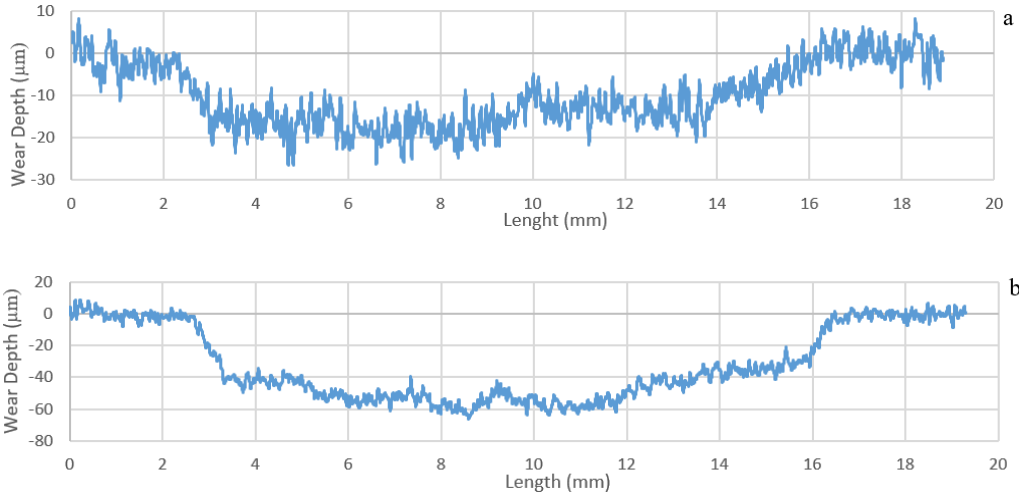

Figure 7.84: *FD605 heat-treated 0° specimen wear profile (a) center (b) edge*

7.4.4 Erosion wear results of NIFD PLUS hardfacing alloy

Pulse Jet results conducted on NIFD PLUS in as clad and heat-treated conditions are presented in Figure 7.85, higher mass loss is encountered in nickel based alloys as compared to iron based alloys for both impingement angles. Wear profile of as clad specimens are presented in Figure 7.86 and 7.87.

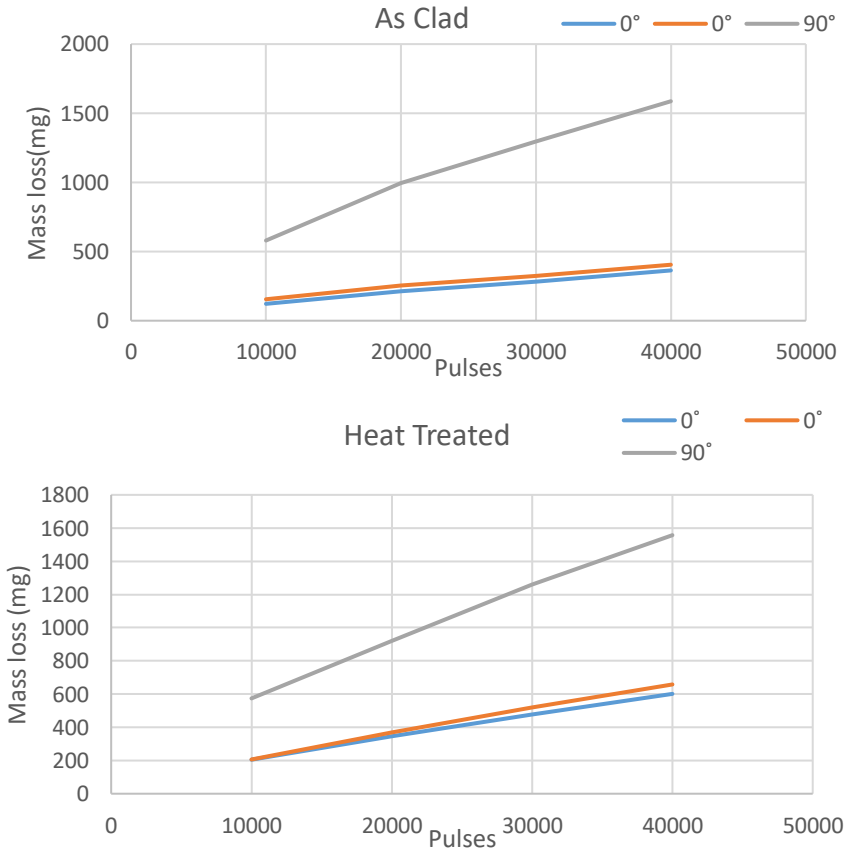

Figure 7.85: *Pulse jet result of NIFD PLUS in as clad and heat-treated conditions*

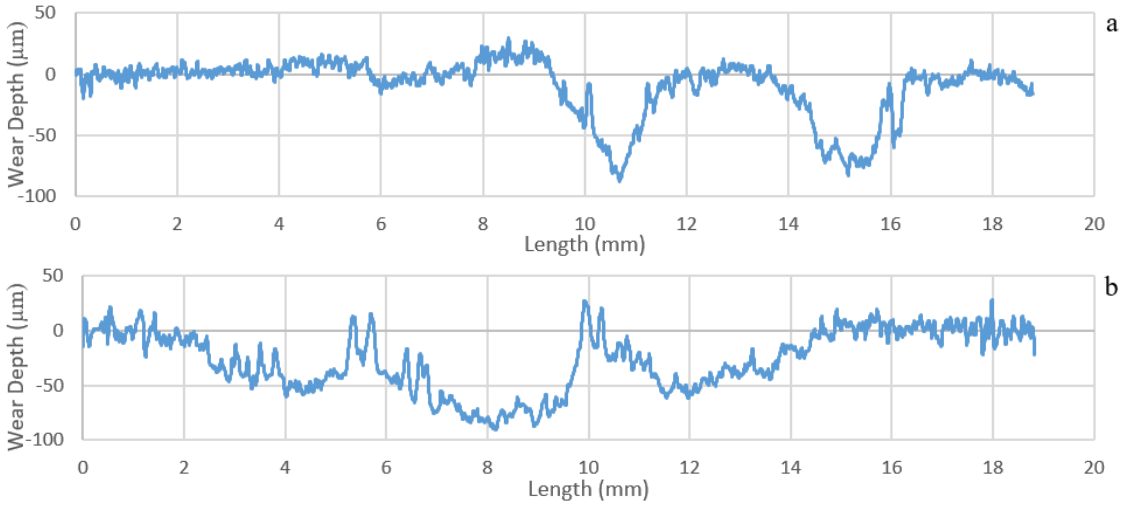

Figure 7.86: *NIFD PLUS as clad 0° specimen wear profile (a) center (b) edge*

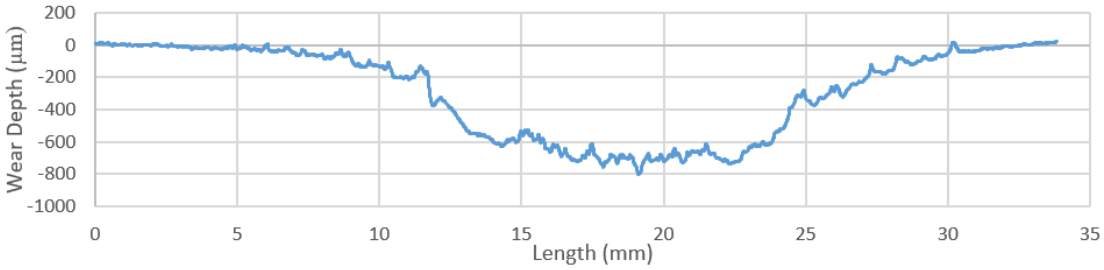

Figure 7.87: *Wear profile of as clad NIFD PLUS 90° specimen*

The lower curves in Figure 7.86a are from insufficient grinding or uneven distribution of carbides between the beads and it gives the idea that higher wear has occurred at that area. The wear depth profile of NIFD PLUS heat-treated are presented in Figure 7.88 and 7.89. Alicona results prove that heat-treated specimens of NIFD has yielded in a higher wear rate as compared to as clad specimens.

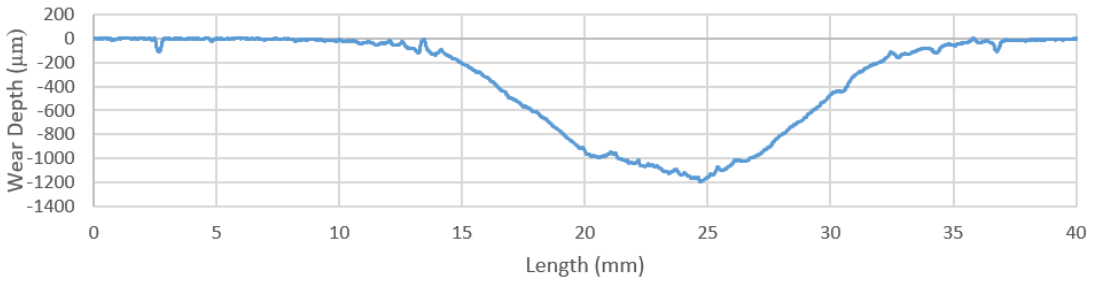

Figure 7.88: *Wear profile of heat-treated NIFD PLUS 90° specimen*

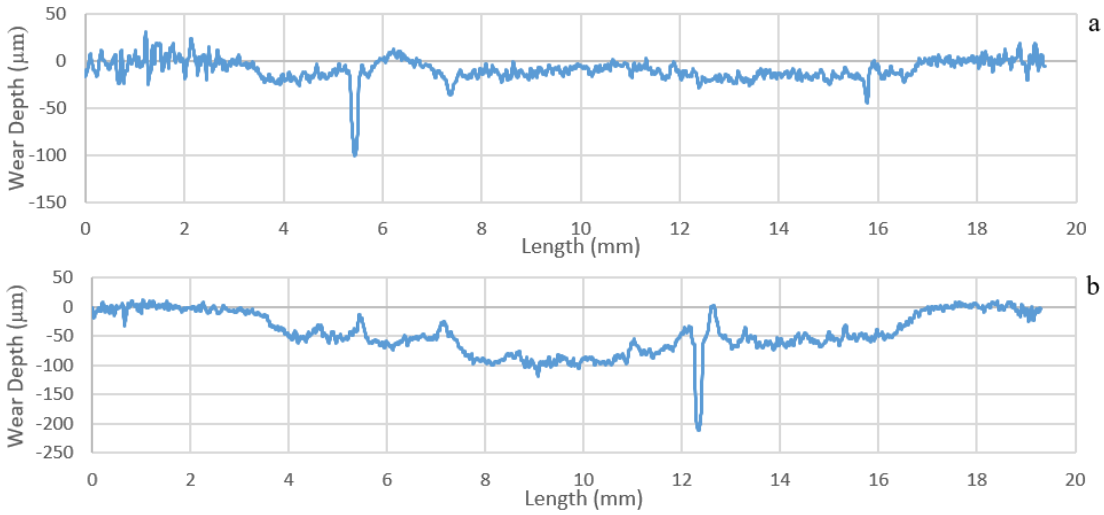

Figure 7.89: *NIFD PLUS heat-treated 0° specimen wear profile (a) center (b) edge*

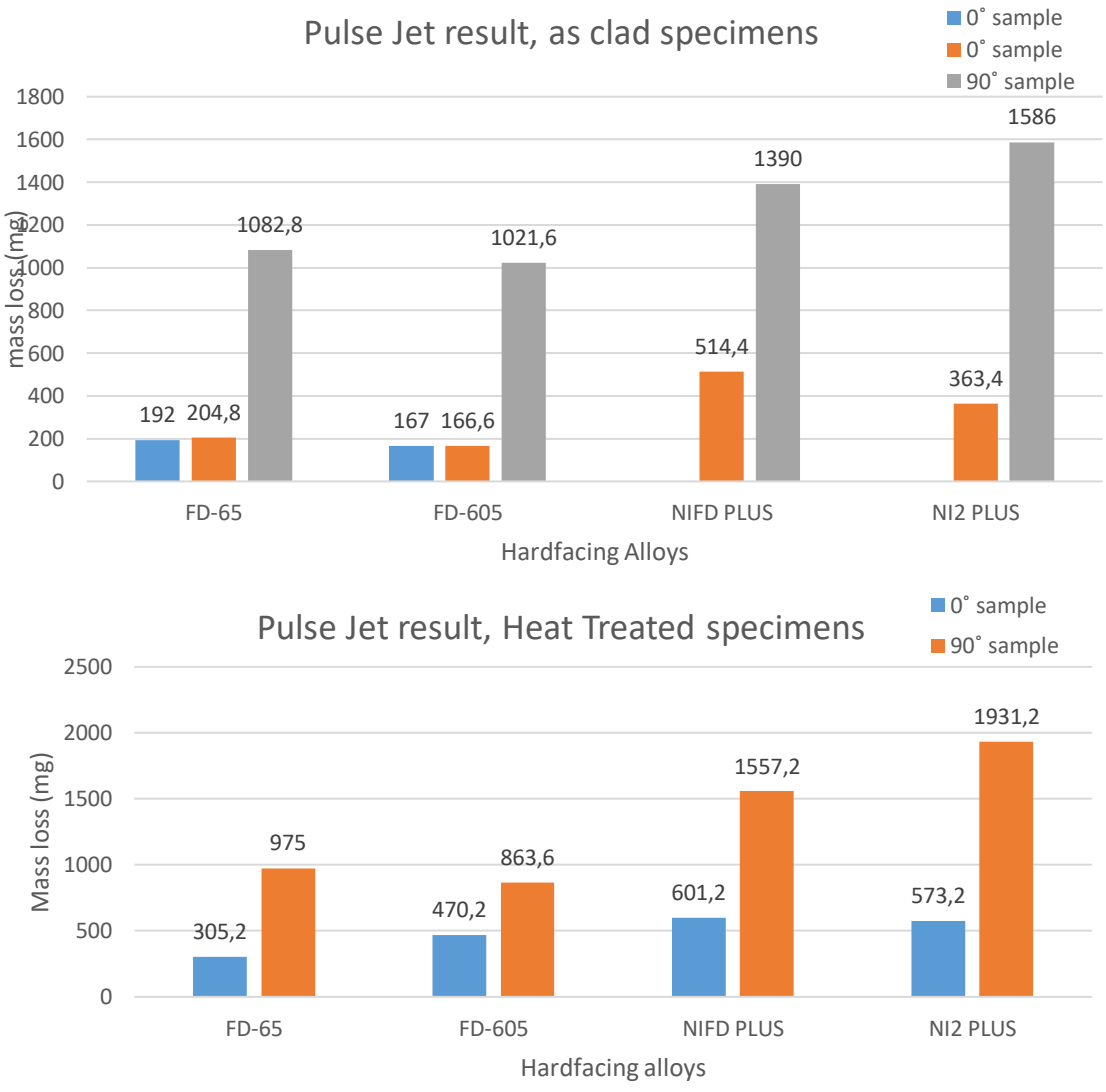

Figure 7.90: *Pulse jet result of selected alloys in as clad and heat-treated conditions*

A comparison of pulse jet test between the selected hardfacing alloys, in as clad and heat-treated conditions, is presented in Figure 7.90. The iron based alloys offer higher wear resistance in 90° and 0° impingement angles as compared to nickel based alloys in as clad as well as heat-treated states. In 90° angles, iron based alloys offered a higher wear rate in as clad condition as compared to heat-treated samples. Nickel based alloys showed a higher erosion resistance in as clad state at 0° angle than heat-treated; NI2 PLUS yielded better erosion resistance in 90° specimen in as clad, while NIFD PLUS shows vice versa results.

The results of pulse jet were compared with two reference materials; S355 construction steel (HV200) and selected quench and tempered steel, the results were only compared in as clad conditions. The relative wear of hardfacing alloys in comparison to S355 is presented in Figure 7.91 and relative wear with quench and tempered steel is presented in Figure 7.92.

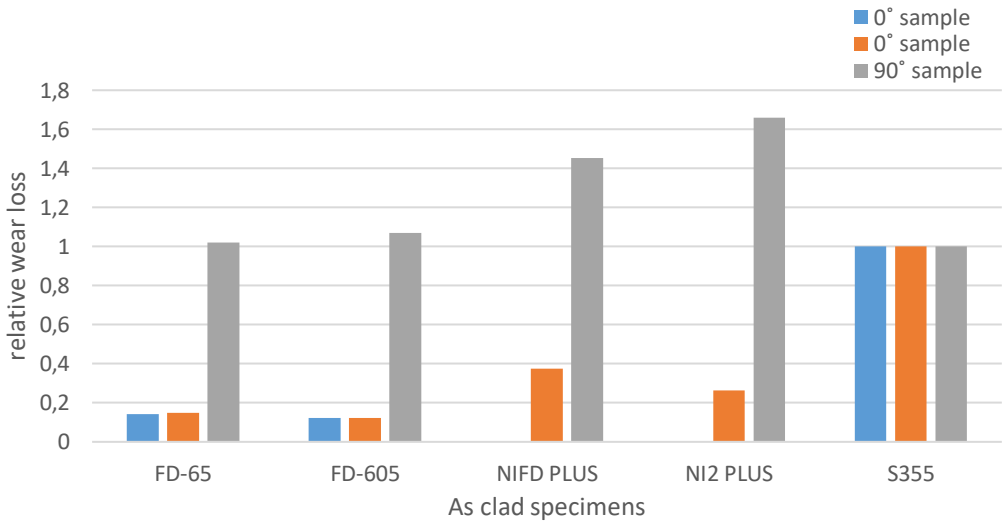

Figure 7.91: *Relative wear of alloys in comparison to S355*

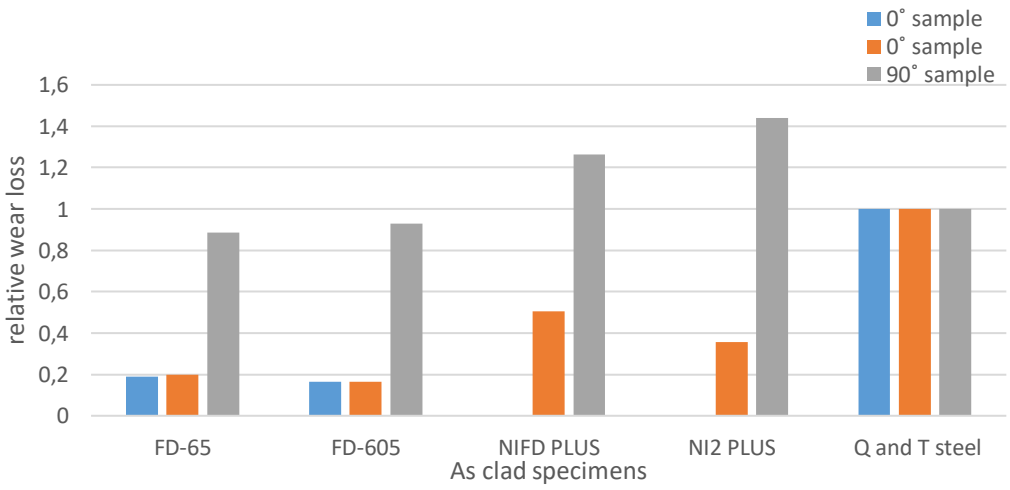

Figure 7.92: *Relative wear of alloys in comparison to quench and tempered steel*

8. DISCUSSION

Iron based hardfacing alloys offered a high erosion resistance as compared to nickel based alloys in pulse jet test; while in hammer mill test FD605 proved to be the most impact resistant alloy, the reason being ductile austenitic microstructure, lack of porosity and crack free surface.

The 90° specimens in pulse jet test incurred a high erosion loss than the S355 reference sample, the reason is the effect of particle angle, as brittle materials show high erosion rate at high impact angles and ductile materials show high erosion rates at low impact angles [62]. This statement was proved by the pulse jet comparison of hardfacing alloys with S355, which is a ductile material and has low hardness.

The detailed explanation of each selected in regards to their structure, before and after heat treatment, and wear results from hammer mill test and pulse test are discussed in the following sections.

8.1 FD65 hardfacing alloy

The chromium rich M_7C_3 carbides are the main reason for the wear resistance of this type of alloy, which are also the first phase to solidify after welding. The volume fraction of these carbides are higher at the surface which shows that the growth rate is high at high cooling rates. The hardness of the alloy is also high at the surface because of high cluster of carbides at the surface and the hardness value decreased along the length of the coating where the fraction of carbides were low. Long vertical cracks are a characteristic of this alloy and they occur due to high percentage of chromium and carbon. Bonding defects were visible at the interface of the hardfacing and they are due to low WFR selected. After heat treatment, low magnification image of the clad profile reveal that coating disintegrated and cracked from some parts of the deposit. There was evidence from optical microscopy that some of the carbides broke along the length of the carbide and results of XRD prove that transformation of ferrite from austenite in the matrix of the alloy; these all factors contribute to the low hardness values as compared to as cladded hardfacing.

Mass loss of FD65 in hammer mill test occurred due to material removal from the cracks and brittle nature of the alloy due to high carbon content. The mass loss was low in as clad condition, even at high impact energies. The heat-treated samples showed a high mass loss at both impact frequencies; the reason being high crack density and softening of the structure because of the ferrite transformation and disjunction of carbides.

The wear loss from pulse jet test at the 90° angle specimen was high in as clad state and was comparatively low for heat-treated condition; reason for high resistance in heat-

treated condition is the induction of ductility by the transformation of ferrite. The same reason applies vice versa for the increased mass loss of the 0° specimen in the heat-treated state. The 0° erosion sample showed a high wear rate at the start and then wear rate suppressed as the number of pulses increases. This behavior occurred because of the cracks present and the edge; the erosion rate was high at the initial pulses because the cracks and edges are sharp at the initial pulse cycle and as the pulse cycle proceeds the edges and cracks become blunt and the erosion is decreased. The profile analysis from Alicona gives the evidence that sharpness of the cracks has lost after the pulse jet cycles have been completed.

8.2 FD605 hardfacing alloy

FD605 is a hypoeutectic low alloyed hardfacing material containing vanadium carbides that provide wear resistance to this alloy; SEM and EDS results have shown that there are also small precipitated hardened carbides in the alloy. Vanadium carbides were quite well dispersed throughout the alloy and provides similar hardness values in the entire hardfacing deposit. The deposit of FD605 was free of cracks, porosity and any inconsistencies; the interface images show that there is good bonding between the matrix and the alloy. Dilution values encountered for FD605 was quite high as compared to other selected alloys, but the maximum dilution was found at the ends of the beads and that is basically due to the low travel speed selected; low travel speed selected forces high heat input at the ends of the weld beads resulting in high dilution. The depth of HAZ in base metal encountered with this alloy was large, reason being the high heat input due to low travel speeds. As this alloy has the tendency to develop a work hardening layer after plastic deformation; hardness results show that the depth of work hardening is around 200µm after grinding.

After heat treatment, the hardness dropped to high degree, from 800HV to 450HV. XRD results did not reveal much and only identified the transformation of ferrite from the austenite matrix. SEM images and EDS results show that the precipitated carbides have dissolved after heat treatment. These carbides go through dissolution at heat treatment during cooling resulting in loss of the hardness of the alloy [70]; the transformation of ferrite and dissolution of precipitated carbides are the reason for overall decreased hardness in FD605 after heat treatment. However, it was also seen that the vanadium carbides were not affected by heat treatment, as indicated by the results from optical microscopy and SEM.

The mass loss of FD605 from hammer mill test was very low at both impact energies as comparison to other hardfacing alloys, in both as clad and heat-treated conditions. The reason is the absence of crack and porosity which prevent material detachment. Even though the hardness decreased in the heat-treated specimens, but it did not effect the impact resistance of the alloy. Due to the induced ductility after heat treatment, FD605 did

undergo some surface deformations after impacts at 10.5Hz frequency, according to the results from Alicona presented in Figure 7.59b.

Erosion resistance of FD605 at parallel impingement angles from pulse jet test was highest in comparison with other selected hardfacing alloys, and also the mass loss of perpendicular specimen was comparable to FD65. The wear resistance in as clad specimens is due to the presence of vanadium carbides, precipitated hardened carbides and development of the work hardened layer. After heat treatment, the wear rate increased in 0° specimen due to decrease in hardness. Although the precipitated carbides dissoluted, but it did not affect the erosion resistance of the alloy due to the presence of vanadium carbides and the work hardened layer. The wear resistance of FD605 heat treated 0° specimen was still higher than nickel based alloys. The mass loss decreased in 90° specimen after heat treatment because of induction of ductility due to softening of the specimen.

8.3 NI2 PLUS and NIFD PLUS hardfacing alloys

NI2 PLUS and NIFD PLUS are nickel based alloys consisting of WC/W_2C as reinforcing materials, the difference between the two alloys is different chemical composition and size of wire diameter; NI2 PLUS is the 1.2mm wire and consisted of small size carbides, while NIFD PLUS is a 1.6mm wire and contain larger carbides. The matrix of both alloys consisted of primary nickel dendrites surrounded by a secondary nickel alloyed phase. The matrix of NI2 PLUS also consisted of vanadium carbides; the manufacturer included vanadium carbides to add strength to the matrix. Dilution levels were quite low for both alloys and depth of HAZ was also comparable to the depth observed with FD65. Cracks and pores were seen in the two hardfacing deposits and there was large surface porosity visible in NIFD PLUS between the beads of the cladding. XRD results reveal the presence of elementary tungsten in both alloys, that indicates the dissolution of tungsten carbides that occurred in both deposits. However, the absence of secondary phases such as Ni_3W_3C and Ni_2W_4C illustrate that dissolution was not to a larger extent. These results indicate that these alloys are quite suited for welding or hardfacing with CMT. After heat treatment, there was no such change in the microstructure of the alloy. The hardness of the matrix dropped to a certain extent, but it is due to the softening of the secondary phases. Post weld heat treatment in nickel based alloys produced cracks in the coating as well as base metal. The crack in the base material may be produced due to the stresses in HAZ region. This suggests that the post heat treatment parameters selected does not suit cladding and can lead to undesirable results.

The volume fraction of tungsten carbides was not sufficient in both alloys; to reveal extra information about the low percentage of carbides, a video was made by high speed camera. The image captured from the camera is given in Figure 8.1. The image shows that the tungsten carbides do not go effectively into the weld pool and surround the weld area as black powder. The reason seems to be the retracting movement of wire that occurs while the weld drop is deposited. However, the reason for the escaping of carbides is not

quite fully understood, as hardfacing of nickel based wires with CMT is quite new to perform.

It was seen that WC/W_2C were not spread throughout the coating and there was inhomogeneous distribution of tungsten carbides in nickel based coatings; particularly in NIFD PLUS. Reason is the high density of tungsten carbide particles; they tend to sink at the bottom of the clad; specially the particles that have the larger size [71]. One solution can be that higher travel speeds be utilized to achieve higher solidification rates; Shu et al.[71] have described that homogenous distribution of tungsten carbides can also be achieved by depositing multi-layered clads.

The mass loss of NI2 and NIFD in hammer mill test occurred by the particle detachment from the cracks and pores by repeated impacts. The mass of these alloys was similar in low frequency impacts in both as clad and heat-treated conditions, but mass loss of heat-treated increased to a high degree when specimen was subjected to high impact energies. It is due to the breaking of clad after heat treatment; heat treatment induced severe cracks in the coating that led to elevated mass loss at high impact energies and increased the rate of particle detachment.

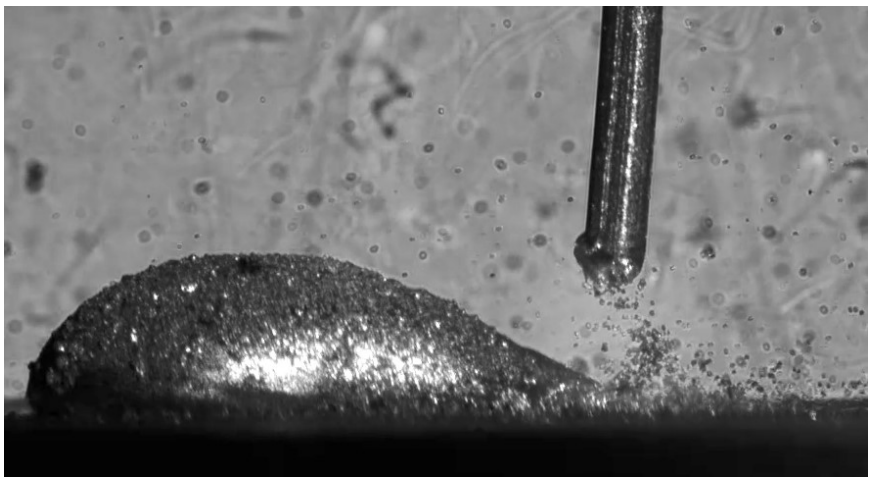

Figure 8.1: *Images of high-speed camera from the welding of nickel based wires*

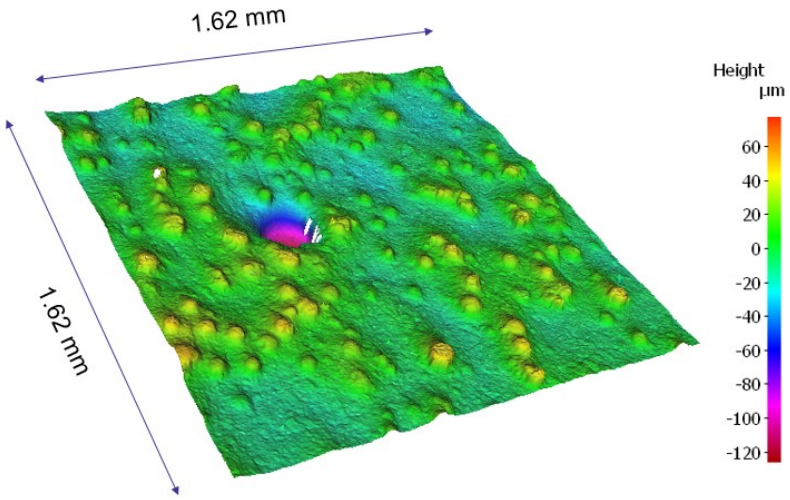

Figure 8.2: *Edge image of pulse jet NI2 PLUS specimen*

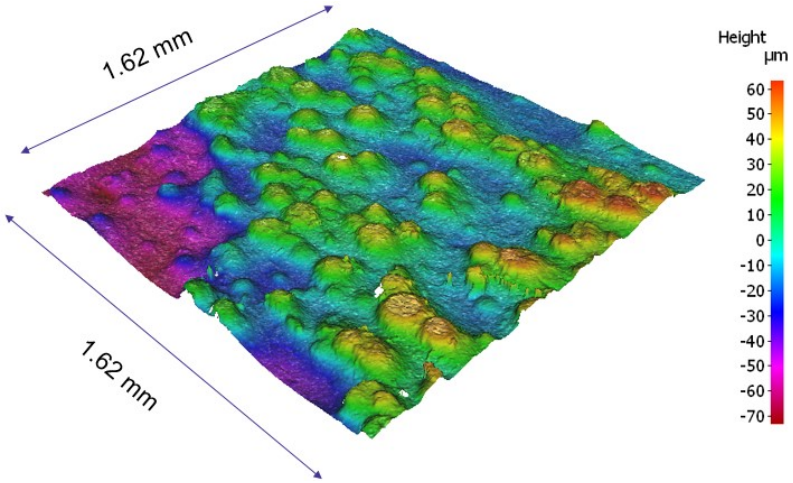

Figure 8.3: *Edge image of pulse jet NIFD PLUS specimen*

Erosion resistance at both impingement angles of nickel base alloys was the lowest as compared to the iron based alloys. Figure 8.2 and 8.3 shows the Alicona image of edge of NI2 PLUS and NIFD PLUS pulse jet specimen after the test. The Figures show the areas that have been affected by erosion at low impingement angles. However, there are few places visible in Figure 8.3 in which it is seen that carbides have deteriorated. The information related to damage of carbides can be found from reference [72]. The tungsten carbides in NI2 PLUS have undergone less distortion than NIFD PLUS because of the small size. The Alicona wear depth results and Figure 8.3 also reveal that the matrix of NI2 PLUS suffered a low wear depth as compared to NIFD PLUS, reason is due to the presence of vanadium carbides which were introduced to provide extra strength to matrix. However, the wear results were still quite high as compared to iron based alloys.

9. CONCLUSION

Four hardfacing alloys were compared for their impact resistance and erosion resistance in as clad and post weld heat-treated condition. The four hardfacing materials included two iron based and two nickel based alloys. The coatings were deposited by CMT, and welding results showed that CMT welding leads to low dilution, moderate heat input, high coating thickness and is capable weld variety of dissimilar metals. It can be deduced that welding on heat-treated steels, with suitable preheating temperature, lead to better results than cladding on top of soft steels and heat treating it after cladding. So, welding on quenched and tempered steels, at least on 22mm thickness specimens leads to higher wear resistance than post weld heat-treated claddings.

It can be concluded that all the alloys showed higher impact wear resistance and erosion wear resistance in as clad condition; iron based alloys showed higher resistance to 90° erosion resistance, because of induction of ductility. Post weld heat-treated specimen also creates a risk of cracking in the base metal.

FD605 produced higher impact resistance from the hammer mill test, because of absence of cracks and porosity. NI2, NIFD and FD65 showed higher mass loss in the heat-treated condition at high impacts because of increase in the crack density.

FD605 and FD65 showed higher erosion resistance than NI2 and NIFD in pulse jet test in both as clad and heat-treated conditions. FD605 offers wear resistance from vanadium carbides and work hardened layer, while FD65 contain ledeburitic chromium carbides which provide strength to this alloy. The deposition of nickel based alloys did not perform well in the pulse jet test and led to higher erosion rates.

For further study of the hardfacing of these alloys from CMT some recommendations are also discussed. The heat treatment parameters selected resulted in the emergence of crack in the base metal; the base metal cracked due to the stresses in the heat affected zone. It is recommended that if required suitable heat treatment parameters with lower heating rates be selected or stress relief annealing can be conducted prior to heat treatment.

FD65 alloy had pores in the interface and it is basically due to low WFR selected, it is possible to improve the surface qualities by adopting a higher WFR. FD605 had a higher dilution as compared to other hardfacing alloys, but that was high at the end of the coating; higher travel speeds may reduce this dilution and decrease heat input.

REFERENCES

[1] P. Vespa, P.T. Pinard, R. Gauvin, M. Brochu, Analysis of WC/Ni-Based Coatings Deposited by Controlled Short-Circuit MIG Welding, Journal of Materials Engineering and Performance, Vol. 21, Iss. 6, 2012, pp. 865-876.

[2] J.R. Davis, Hardfacing alloys in: Anonymous (ed.), Metals Handbook, Desk Edition (2nd Edition), ASM International, pp. 671-673.

[3] H. Yokota, Welding Consumables, Journal Of The Japan Welding Society, Vol. 81, Iss. 5, 2012, pp. 440-442.

[4] Lee G. Kahvidal, The Practical Reference Guide for Hardfacing: American welding society, , Welding and manufacturing engineering.

[5] G. R.C. Pradeep, A. Ramesh: A Review Paper On Hardfacing Processes And Materials, Springer, Berlin 2010, .

[6] G. Bastien, Fundamentals of Hardfacing by Arc welding, 1. publ. ed. Welding alloys group, France, 2018, .

[7] B. Venkatesh, K. Sriker, V.S.V. Prabhakar, Wear Characteristics of Hardfacing Alloys: State-of-the-art, Procedia Materials Science, Vol. 10, 2015, pp. 527-532.

[8] Prof. Petri Vuoristo, Weld surfacing, Lecture notes from ' coatings and surface treatments' 2017, Tampere University.

[9] Introduction to Oxy-Acetylene Welding, in: The American Heritage Dictionary of the English Language, 5th edition ed., Solas, Further education and training authority, Boston, 2014.

[10] A. Sue, H. Sreshta, B.H. Qiu, Improved Hardfacing for Drill Bits and Drilling Tools, Journal of Thermal Spray Technology, Vol. 20, Iss. 1, 2011, pp. 372-377.

[11] Butterworth-Heinemann Chapter 3 - Welding and Joining Processes, in: Applied Welding Engineering (Second Edition), 2016, pp. 163-195.

[12] Amado, Cruz-Crespo , R. Scotti, Operational behavior assessment of coated tubular electrodes for SMAW hardfacing, in: Journal of Materials Processing Technology, 2008, pp. 265-273.

[13] Cruz-Crespo, R.F. Fuentes, A. Scotti, The Influence of Calcite, Fluorite, and Rutile on the Fusion-Related Behavior of Metal Cored Coated Electrodes for Hardfacing, Journal of Materials Engineering and Performance, Vol. 19, Iss. 5, 2010, pp. 685-692.

[14] P.K. Ghosh, Introduction to Gas Metal Arc Welding Process, in: P.K. Ghosh (ed.), Pulse Current Gas Metal Arc Welding: Characteristics, Control and Applications, Springer Singapore, Singapore, 2017, pp. 1-30.

[15] L. Foulilland, M. Mansori E.Massaq, Friction-induced work hardening of cobalt-base hardfacing deposits for hot forging tools, in: Journal of Materials Processing Technology, 2009, pp. 3366-3373.

[16] U. Ersoy, E. Kannatey-Asibu, S.J. Hu, Analytical Modeling of Metal Transfer for GMAW in the Globular Mode, Journal of Manufacturing Science and Engineering, Vol. 130, Iss. 6, 2008, pp. 8.

[17] V. Vergara, J. Dutra, A.S. D'Oliveira, Hardfacing by Plasma Transferred Arc Process, in: Anonymous (ed.), 2011.

[18] D.H. Phillips, Welding Engineering: An Introduction, John Wiley & Sons, Incorporated, New York, 2016, .

[19] Mustafa Ulutan, Koray Kiliçay, Osman Nuri Çelik and Ümit Er: Microstructure and wear behaviour of plasma transferred arc (PTA)-deposited FeCrC composite coatings on AISI 5115 steel, in: Journal of Materials Processing Technology, 2016, pp. 26-34.

[20] S. Selvi, A. Vishvaksenan and E. Rajasekar :Cold metal transfer (CMT) technology - An overview, in: Defence Technology, 2018, pp. 28-44.

[21] P. Kah, R. Suoranta, J. Martikainen, Advanced gas metal arc welding processes, The International Journal of Advanced Manufacturing Technology, Vol. 67, Iss. 1, 2013, pp. 655-674.

[22] C.G. Pickin, K. Young, Evaluation of cold metal transfer (CMT) process for welding aluminium alloy, Science & Technology of Welding & Joining, Vol. 11, Iss. 5, 2006, pp. 583-585.

[23] Fronius Description of CMT: Cold Metal Transfer , process, working and advantages

[24] A. Azar, A heat source model for cold metal transfer (CMT) welding, Journal of Thermal Analysis & Calorimetry, Vol. 122, Iss. 2, 2015, pp. 741-746.

[25] C. G. Pickin, S. W. Williams and M. Lunt: Characterization of the cold metal transfer (CMT) process and its application for low dilution cladding, in: Journal of Materials Processing Technology, 2011, pp. 496-502.

[26] O. T. Ola, F. E. Doern: A study of cold metal transfer clads in nickel-base INCONEL 718 superalloy, in: Materials & Design, 2014, pp. 51-59.

[27] R. Cao, Gang Yu, J. H. Chen and Pei-Chung Wang: Cold metal transfer joining aluminum alloys-to-galvanized mild steel, in: Journal of Materials Processing Technology, 2013, pp. 1753-1763.

[28] C. Breck Hitz, J.J. Ewing, J. Hecht, An Overview of Laser Technology, in: Anonymous (ed.), Introduction to Laser Technology, IEEE, 2001, pp. 1.

[29] Breck Hitz: laser cladding chapter 12 in: Anonymous (ed.), Laser processing of engineering materials, pp. 296-326.

[30] Qian Ming, L. C. Lim and Z. D. Chen: Laser cladding of nickel-based hardfacing alloys, in: Surface and Coatings Technology, 1998, pp. 174-182.

[31] I. Hemmati, V. Ocelík and J. Th. M. De Hosson: Dilution effects in laser cladding of Ni–Cr–B–Si–C hardfacing alloys, in: Materials Letters, 2012, pp. 69-72.

[32] J. Amado, M.J. Tobar, J. Alvarez, J. Lamas, A. Yañez, Laser cladding of tungsten carbides (Spherotene (R)) hardfacing alloys for the mining and mineral industry, 2009, 5553-5556 p.

[33] Howard E. Boyer, Timothy L. Gall, Metals Handbook Desk Edition, American Society of Metals, Metals Park, Ohi, 1997, 17.10 p.

[34] Sachin Pawar, Aman Kumar Jha and Goutam Mukhopadhyay: Effect of different carbides on the wear resistance of Fe-based hardfacing alloys, in: International Journal of Refractory Metals and Hard Materials, 2019, pp. 288-295.

[35] C. Lin, C. Chang, J. Chen, C. Hsieh, W. Wu, Microstructural Evolution of Hypoeutectic, Near-Eutectic, and Hypereutectic High-Carbon Cr-Based Hard-Facing Alloys, Metallurgical and Materials Transactions A, Vol. 40, Iss. 5, 2009, pp. 1031-1038.

[36] Patricio F. Mendez, Nairn Barnes, Kurtis Bell, Welding processes for wear resistant overlays, in: Journal of Manufacturing Processes, 2014, pp. 4-25.

[37] Amado. Cruz-crespo, R. Fuentes, A. Valtair Ferraressi, R. Ariza Gonçalves, A. Scotti, Microstructure and Abrasion Resistance of Fe-Cr-C and Fe-Cr-C-Nb Hardfacing Alloys Deposited by S-FCAW and Cold Solid Wires, 2016, 342-353 p.

[38] H. Sabet, S. Khierandish, S. Mirdamadi, M. Goodarzi, The Microstructure and Abrasive Wear Resistance of Fe–Cr–C Hardfacing Alloys with the Composition of Hypoeutectic, Eutectic, and Hypereutectic, Tribology Letters, Vol. 44, Iss. 2, 2011, pp. 237.

[39] I. Hemmati, V. Ocelík and J. Th. M. De Hosson: Effects of the Alloy Composition on Phase Constitution and Properties of Laser Deposited Ni-Cr-B-Si Coatings, in: Physics Procedia, 2013, pp. 302-311.

[40] K. Gurumoorthy, M. Kamaraj, K. Prasad Rao, A. Sambasiva Rao and S. Venugopal: Microstructural aspects of plasma transferred arc surfaced Ni-based hardfacing alloy, in: Materials Science and Engineering: A, 2007, pp. 11-19.

[41] Qian Ming, L. C. Lim and Z. D. Chen: Laser cladding of nickel-based hardfacing alloys, in: Surface and Coatings Technology, 1998, pp. 174-182.

[42] A. E. Yaedu, A. S. C. M. D'Oliveira: Microstructural design of hardfacing Ni–Cr–B–Si–C alloys, in: Acta Materialia, 2013, pp. 6061-6070.

[43] C. Katsich, E. Badisch: Effect of carbide degradation in a Ni-based hardfacing under abrasive and combined impact/abrasive conditions, in: Surface and Coatings Technology, 2011, pp. 1062-1068.

[44] M. Mohaideen, M. Duraiselvam, K. Ganesh: Plasma Transferred Arc Welding of Stellite 6 Alloy on Stainless Steel for Wear Resistance, in: Procedia Technology, 2016, pp. 1305-1311.

[45] A.E. Yaedu, D'Oliveira, A. S. C. M., Cobalt based alloy PTA hardfacing on different substrate steels, Materials Science and Technology, Vol. 21, Iss. 4, 2005, pp. 459-466.

[46] H. Deng, H. Shi, S. Tsuruoka, Influence of coating thickness and temperature on mechanical properties of steel deposited with Co-based alloy hardfacing coating, 2010, 3927-3934 p.

[47] R. Liu, J. H. Yao, Q. L. Zhang, M. X. Yao and R. Collier: Sliding wear and solid-particle erosion resistance of a novel high-tungsten Stellite alloy, in: Wear, 2015, pp. 41-50.

[48] H. Bhadeshia, R. Honeycombe, Steels: Microstructure and Properties, Elsevier Science & Technology, Oxford, 2017, .

[49] Sindo Kou, Welding metallurgy, Wiley and sons, 2002, .

[50] I. Magnabosco, P. Ferro, F. Bonollo and L. Arnberg: An investigation of fusion zone microstructures in electron beam welding of copper–stainless steel, in: Materials Science and Engineering: A, 2006, pp. 163-173.

[51] S.A. David, S.S. Babu, J.M. Vitek, Welding: Solidification and microstructure, JOM, Vol. 55, Iss. 6, 2003, pp. 14-20.

[52] H.J. Grabke, H.J. Grabke, Surface and grain boundary segregation on and in iron and steels, ISIJ International, Vol. 29, Iss. 7, 1989, pp. 529-538.

[53] Dieter Radaj, Heat Effects of welding, Daimler Benz, Germany, 1992 .

[54] T. Falkenreck, M. Klein, T. Böllinghaus, Dynamic compressive behaviour of weld joints, 2017, .

[55] L. Lan, C. Qiu, D. Zhao, X. Gao, L. Du, Analysis of martensite–austenite constituent and its effect on toughness in submerged arc welded joint of low carbon bainitic steel, Journal of Materials Science, Vol. 47, Iss. 11, 2012, pp. 4732-4742.

[56] Mansilla Yanet, Zalazar Mónica: Microstructure Characterization of Heat Affected Zone in Single Pass Welding in 9Cr-1Mo Steels, in: Procedia Materials Science, 2015, pp. 904-913.

[57] C. Qiu, L. Lan, D. Zhao, X. Gao, L. Du, Microstructural evolution and toughness in the HAZ of submerged arc welded low welding crack susceptibility steel, Acta Metallurgica Sinica (English Letters), Vol. 26, Iss. 1, 2013, pp. 49-55.

[58] Zhenshun Li, Xuemin Zhao and Dongri Shan: Impact Toughness of Subzones in the Intercritical Heat-Affected Zone of Low-Carbon Bainitic Steel, in: Materials, Vol. 11 2018.

[59] Germanischer lloyd AG: Preheating in welding technology, in:, Netherlands, 2010.

[60] G.Y. Baek, K.Y. Lee, S.H. Park, D.S. Shim, Effects of substrate preheating during direct energy deposition on microstructure, hardness, tensile strength, and notch toughness, Metals and Materials International, Vol. 23, Iss. 6, 2017, pp. 1204-1215.

[61] Quan Lai, Ralph Abrahams, Wenyi Yan, Cong Qiu: Effects of preheating and carbon dilution on material characteristics of laser-cladded hypereutectoid rail steels, in: Materials Science and Engineering: A, 2018, pp. 548-563.

[62] G.W. Stachowiak, A.W. Batchelor, Engineering tribology, Fourth edition ed. Butterworth-Heinemann, Elsevier, Amsterdam, 2014, 525-571 p.

[63] I. Kleis, P. Kulu, Solid Particle Erosion : Occurrence, Prediction and Control, Springer, London, 2007, .

[64] Md. Aminul Islam, Zoheir N. Farhat: Effect of impact angle and velocity on erosion of API X42 pipeline steel under high abrasive feed rate, in: Wear, 2014, pp. 180-190.

[65] J. Laurila, A. Milanti, J. Nurminen, M. Kallio and P. Vuoristo: Microstructure and wear behaviour of a vanadium carbide reinforced weld coating, in: Wear, 2013, pp. 142-149.

[66] Karppi Risto, Nevasmaa Pekka, Ovakon terästen hitsaus, 2010.

[67] Tihinen Sakari, Hitsausenergian E ja lämmöntuonnin Q laskeminen, 2013.

[68] Jari Tuominen: Image analysis of claddings: Tampere University, Tampere, 2017.

[69] K. Osara, T. Tiainen: Three-body impact wear study on conventional and new P/M + HIPed wear resistant materials, in: Wear, 2001, pp. 785-794.

[70] C. Y. Chen, H. W. Yen, F. H. Kao, W. C. Li, C. Y. Huang, J. R. Yang and S. H. Wang: Precipitation hardening of high-strength low-alloy steels by nanometer-sized carbides, in: Materials Science and Engineering: A, 2009, pp. 162-166.

[71] Da Shu, Zhuguo Li, Ke Zhang, Chengwu Yao, Dayong Li and Zhenbang Dai: In situ synthesized high volume fraction WC reinforced Ni-based coating by laser cladding, in: Materials Letters, 2017, pp. 178-181.

[72] D. Zhou, H. Cui, P. Xu, F. Lu: Tungsten Carbide Grain Size Computation for WC-Co Dissimilar Welds, Journal of Materials Engineering and Performance, Vol. 25, Iss. 6, 2016, pp. 2500-2510.

APPENDIX A

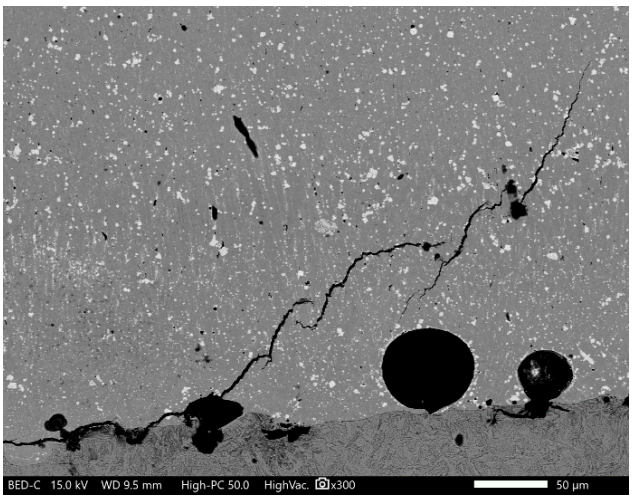

Figure 1: *Interface of FD65 as clad at 300x*

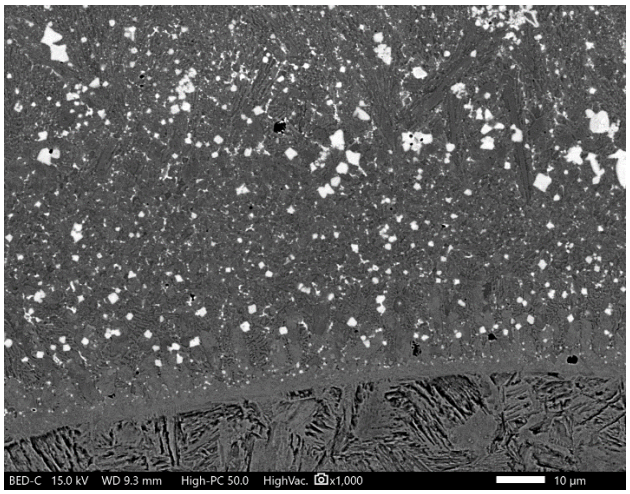

Figure 2: *Interface of NI2 PLUS as clad at 1000x*

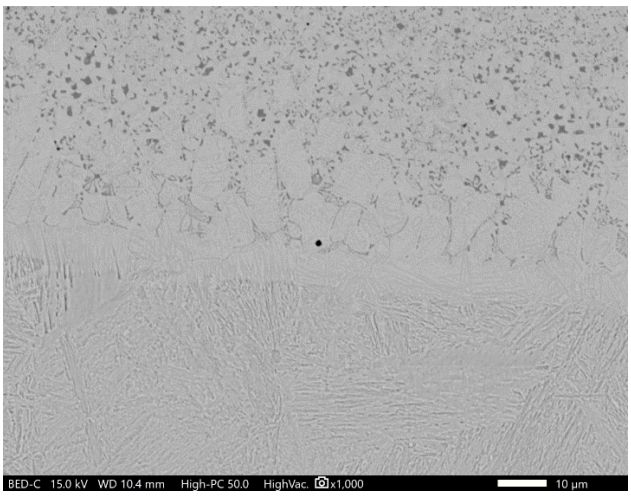

Figure 3: *interface of FD605 as clad at 1000x*

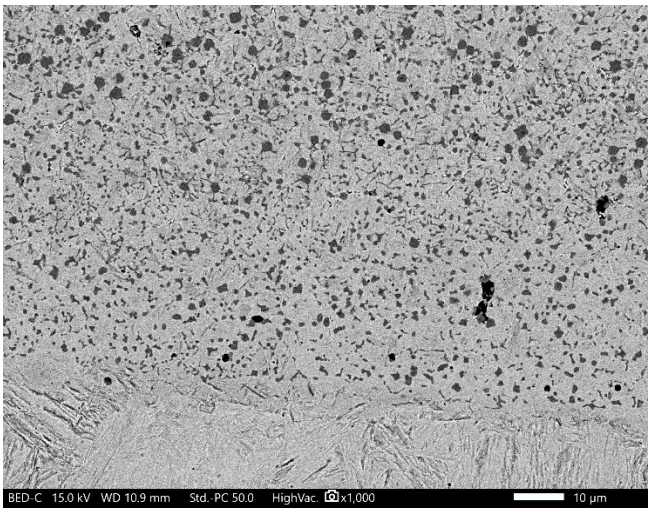

Figure 4: *Interface of FD605 heat-treated at 1000x*

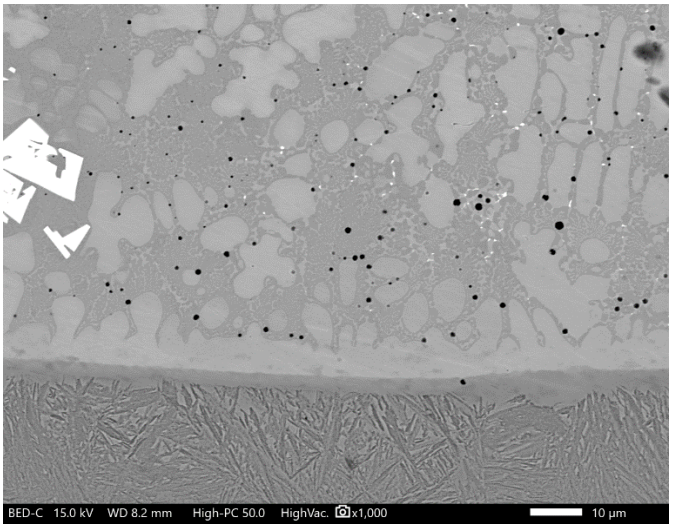

Figure 5: *Interface of NIFD PLUS as clad at 1000x*

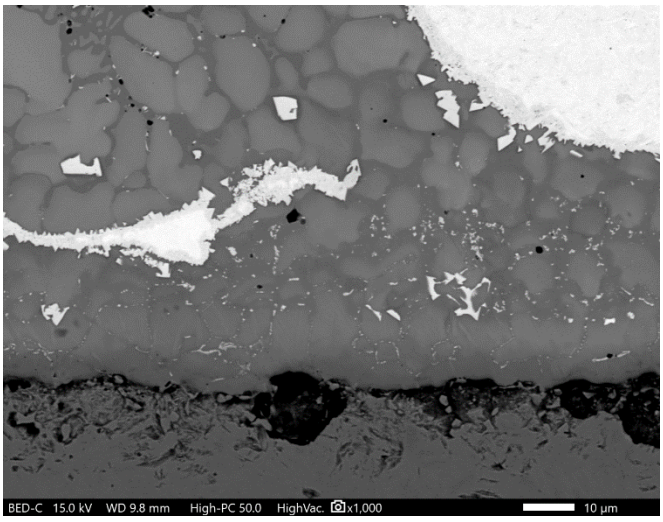

Figure 6: *Interface of NIFD PLUS heat-treated at 1000x*

APPENDIX B

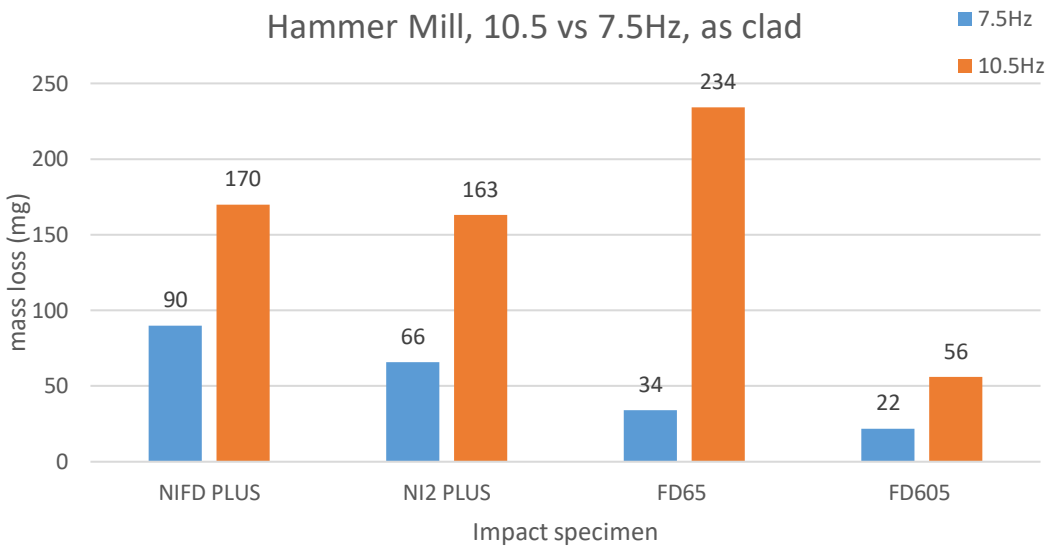

Figure 7: *Hammer mill result comparison of 7.5 and 10.5 Hz frequency for as clad specimen*

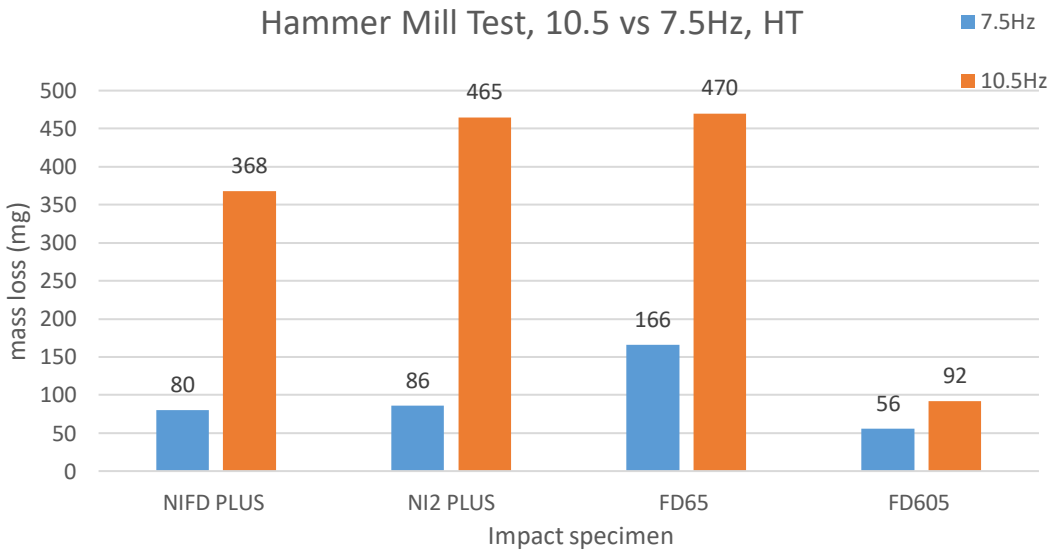

Figure 8: *Hammer mill result comparison of 7.5 and 10.5 Hz frequency for as heat-treated specimen*

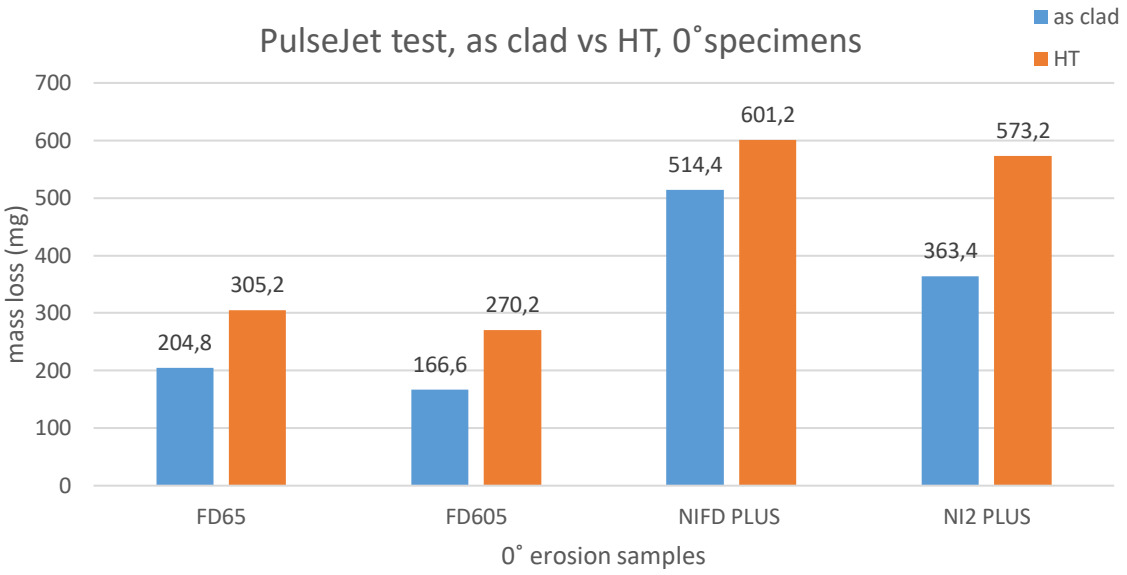

Figure 9: *Pulse jet result of 0˚ erosion specimen*

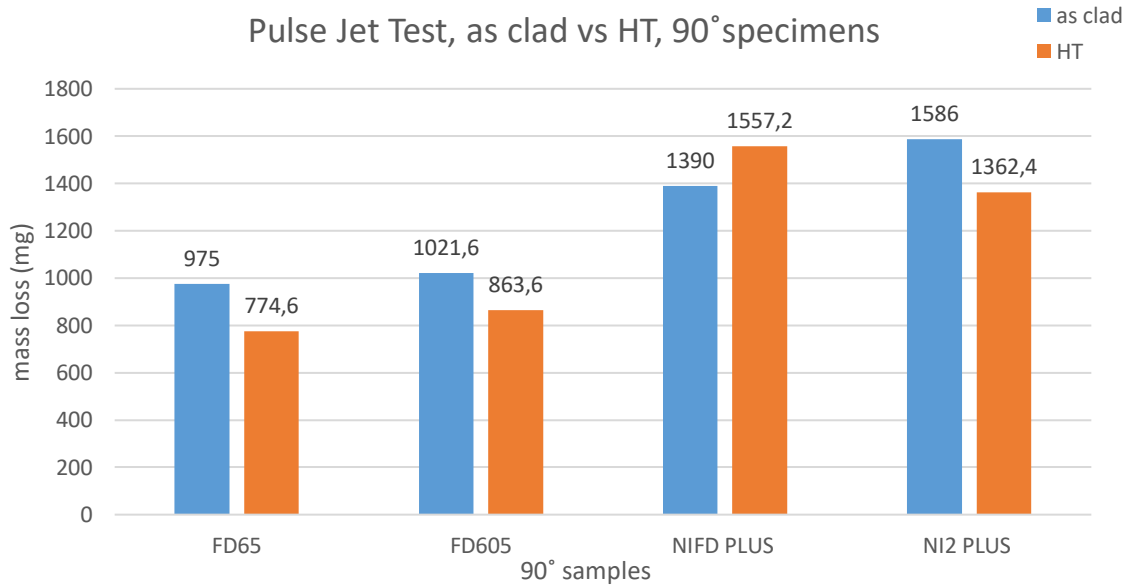

Figure 10*: Pulse jet result of 90˚ erosion specimen*